A Study of b-Quark Associated Higgs Production in the Decay Mode $\mathbf{b\bar{b}\,h/A/H \to \tau\,\tau \to 2\,\ell + 4\,\nu}$ with ATLAS at LHC

Diplomarbeit
zur Erlangung des akademischen Grades
Diplom-Physikerin

vorgelegt von

Jana Schaarschmidt

geboren in Annaberg-Buchholz

Institut für Kern- und Teilchenphysik
Fachrichtung Physik
Fakultät Mathematik und Naturwissenschaften
der Technischen Universität Dresden
2007

CERN-THESIS-2008-086
25/06/2007

1. Gutachter: Prof. Dr. Michael Kobel

2. Gutachter: Dr. Wolfgang Mader

Datum des Einreichens der Arbeit: 25.06.2007

Abstract

In the m_h^{max}-scenario of the Minimal Supersymmetric Extension of the Standard Model the b-quark associated Higgs production is among the most relevant channels. In this thesis an analysis of $b\bar{b}\ h/A/H \rightarrow \tau\ \tau \rightarrow 2\ \ell + 4\ \nu$ for the ATLAS detector at LHC has been performed. The goal of this Monte Carlo study was to obtain the discovery potential for neutral, mass degenerated Higgs bosons with low and medium masses for different points in the $m_A - \tan\beta$ plane.
The results for the significance obtained by a cut and count analysis without considering a systematic uncertainty are the following: A Higgs boson with a mass of 120 GeV can be discovered if $\tan\beta$>6. If the Higgs particle has a mass of 160 GeV it will be discovered if $\tan\beta$>7. If its mass is about 200 GeV it can be discovered if a value of $\tan\beta$>10 is realized in nature.

Kurzfassung

Im m_h^{max}-Szenario der Minimalen Supersymmetrischen Erweiterung des Standardmodells der Teilchenphysik ist die b-quark assoziierte Higgs Produktion einer der relevantesten Kanäle. In dieser Arbeit wurde eine Analyse des Kanals $b\bar{b}\ h/A/H \rightarrow \tau\ \tau \rightarrow 2\ \ell + 4\ \nu$ für den ATLAS Detektor am LHC durchgeführt. Das Ziel dieser Monte Carlo Studie war die Bestimmung des Entdeckungspotentials eines neutralen, massen-entarteten Higgs Bosons mit kleiner bis mittlerer Masse für verschiedene Werte in der $m_A - \tan\beta$ Ebene.
Die Ergebnisse für Signifikanzen einer Schnittanalyse ohne die Inbetrachtziehung von systematischen Unsicherheiten sind die Folgenden: Ein Higgs Boson mit einer Masse von 120 GeV kann für $\tan\beta$ Werte größer als 6 entdeckt werden. Wenn das Higgs Teilchen eine Masse von 160 GeV hat, wird es für $\tan\beta$>7 entdeckt werden. Beträgt seine Masse 200 GeV, so kann es entdeckt werden, falls $\tan\beta$>10 in der Natur realisiert ist.

Table of Contents

List of Figures

List of Tables

List of Abbreviations

$ALICE$	A Large Ion Collider Experiment
$ATLAS$	A Toroidial LHC Apperatus
$ATLFast$	Atlas Fast Simulation package
BR	Branching Ratio
CDF	Collider Detector at Fermilab
$CERN$	Conseil Européen pour la Recherche Nucléaire
CKW	Cabibbo Kobayashi Maskawa
CL	Confidence Level
CMS	Compact Muon Solenoid
CPU	Central Processing Unit
CSC	Cathode Strip Chambers
$DESY$	Deutsches Elektronen-Synchrotron
EM	Electromagnetic
ESD	Event Summary Data
EW	Electroweak
$FCAL$	Forward Calorimeters
$GridKa$	Grid Computing Centre Karlsruhe
GUT	Grand Unified Theory
HEC	Hadronic End-Caps
ID	Inner Detector
LAr	Liquid Argon
LCG	The LHC Grid Computing Project
LEP	Large Electron Positron Collider
LHC	Large Hadron Collider
$LHC-b$	Large Hadron Collider beauty
$Linac$	Linear Accelerator
LSP	Lightest SUSY Particle
$LVL1(2)$	Level 1(2) Trigger
MC	Monte Carlo
MDT	Monitored Drift Tube
ME	Matrix Element
$MSSM$	Minimal Supersymmetric Standard Model
NDF	Number of Degrees of Freedom
$NNLO$	Next-to-Next-to-Leading Order
P	Parity
PS	Proton Synchrotron
QCD	Quantum Chromodynamics

QED	Quantum Electrodynamics
QFT	Quantum Field Theory
RPC	Resistive Plate Chamber
SCT	Semiconductor Tracker
$Sherpa$	Simulation for high energy reactions of particles
SM	Standard Model
SPS	Super Proton Synchrotron
$SUSY$	Supersymmetry
TGC	Thin Gap Chamber
TRT	Transition Radiation Tracker
$UA1(2)$	Underground Area 1(2)
VBF	Vector-Boson-Fusion

Chapter 1

Introduction

The Standard Model of particle physics (SM) is the current theoretical description of the fundamental particles and interactions. It explains a multitude of effects in nature, except for gravity. In the history of its development a trend to unification and simplification cannot be missed. The electric and magnetic forces were unified to the electromagnetic (EM) force in 1864 by Maxwell. The unification of EM and weak forces to the electroweak (EW) interaction was proven in 1983 by the experiments UA1[1] and UA2 at CERN[2] through the discovery of the W and Z bosons. The theoretical description by Glashow, Salam and Weinberg had happened already in 1967. With the development of the QCD in 1973 and the discovery of the gluon in 1979 at DESY[3] the nuclear force was substituted by the more fundamental strong interaction.
An explanation for the origin of mass is also included in the theory, but has not yet been confirmed. The SM postulates a scalar field, present everywhere in the universe as the cause for mass of particles interacting with it. This Higgs[4] field can be detected by a discovery of the Higgs boson. It arises by the interaction of particles with this field and decays in known and detectable particles. Its discovery would be the last missing experimental proof for the SM.

So far the SM has been tested and confirmed in dozens of experiments, but still is not the answer to everything, because it is is not a complete theory. Overall 25 parameters - like couplings of fermions to the Higgs field for example - cannot be derived from first principles. The question why there are three generations of fermions cannot be answered either. Gravity - which is negligible only on mass scales of single elementary particles but not in macroscopic systems - cannot be inserted into the SM. And, furthermore, there is the question what kind of matter or energy 96 % of the universe consist of.
Supersymmetry is one approach to get the big picture of nature. Symmetries are very important in physics and were often the clue to a deeper understanding. This one is a concept linking the matter particles and the force mediators. As a consequence, in the minimal extension of the SM the particle content gets doubled, and there would be much to explore in high energy physics.

[1] UA1 stands for Underground Area 1
[2] Conseil Européen pour la Recherche Nucléaire
[3] Deutsches Elektronen-Synchrotron
[4] Named after Peter Ware Higgs, who proposed together with others the mechanism of spontaneous symmetry breaking in the electroweak theory in 1964.

In the next years several experiments will participate in the search for the 'most wanted' particle and new physics. CDF[5] and DØ - running experiments at Tevatron - could find evidence for a Higgs boson with a mass below 180 GeV[6] in the next years if sufficient luminosity can be collected. The ATLAS[7] experiment at the Large Hadron Collider at CERN in Geneva will explore a Higgs mass range from 100 GeV to 1 TeV. Its construction will be finished in 2007.
The data acquisition from LHC has not yet started, and so Monte Carlo[8] (MC) studies are being performed. One aim of detailed simulation is the exploration of discovery potentials of different processes for getting a starting point when the data taking begins. Another goal is testing the data handling but also improving the cooperation and communication among the collaboration members. MC studies allow the comparison of expectations to the measured data and do also benefit the understanding of elementary processes by studying different computational approaches.

In this thesis an MC analysis of $b\bar{b}\ h/A/H \rightarrow \tau\ \tau \rightarrow 2\ \ell + 4\ \nu$ with simulated data has been performed. The b-quark associated Higgs production is among the most relevant discovery channels in the *Minimal Supersymmetric Standard Model* (MSSM), wherein three neutral Higgs bosons (h/A/H) occur with relatively large production cross sections. The aim of this analysis was to examine the discovery potential of the Higgs bosons as function of different parameter values in the m_h^{max}scenario of the MSSM. In this work Higgs masses from 120 GeV to 300 GeV were considered.
This thesis starts with an explanation of the SM and the theoretical principles its based on. Then Supersymmetry is motivated and the MSSM and its scenarios are described. In chapter 3 the ATLAS experiment is presented. In the next part the usage of MC datasets is described. Afterwards, the selection and reconstruction algorithms are stated. Relevant signal properties are being studied later on. Relevant background channels are included later. A cut analysis is used to improve the significance of the Higgs signal and to suppress backgrounds. This cut method is optimized for different Higgs masses. This allows the extrapolation of a discovery contour in the $\tan\beta$[9] and Higgs mass plane. In addition, a method to estimate the number of background events and a systematic uncertainty. Furthermore an algorithm combining cuts and an analytical fit function is used to discuss the possibility to extract a Higgs signal from experimental data without knowing the Higgs mass.
The conclusion is that the studied process is very promising for a discovery for a wide range of parameter values.

[5]The Collider Detector at Fermilab
[6]In this work natural units have been used: $\hbar = c = 1$
[7]A toroidial LHC apperatus
[8]Monte Carlo methods are algorithms for simulating physical systems on the base of random numbers.
[9]$\tan\beta$ is the ratio of the vacuum expectation values of the two Higgs duplets in the MSSM

Chapter 2

Theoretical Foundations

2.1 The Standard Model of Particle Physics

2.1.1 Phenomenology of the Fundamental Particles and their Interactions

The SM of particle physics [1] is a quantum field theory, which is consistent with quantum mechanics as well as special relativity. Particles forming matter are leptons and quarks (fermions, spin $\frac{1}{2}$), interactions between them are mediated by gauge bosons with integer spin (Table 2.1 [2]). The fundamental leptons and quarks are grouped into three generations (Table 2.2 [2]), whereas the atoms forming matter as it exists today (electrons, protons, neutrons) only consist of particles of the first generation.

Boson	Mass	Electric Charge	Force	Range
γ	$< 10^{-17}$ eV	$< 10^{-30}$	EM	∞
Z^0	91.188 GeV	0	EW	10^{-18} m
$W^{\pm}$	80.403 GeV	± 1	EW	10^{-18} m
g	0	0	strong	10^{-15} m

Table 2.1: Gauge bosons.

Generation	First		Second		Third	
	Flavor	Mass	Flavor	Mass	Flavor	Mass
Leptons	ν_e	≈ 0	ν_μ	≈ 0	ν_τ	≈ 0
	e	0.5110 MeV	μ	105.658 MeV	τ	1.777 GeV
Quarks	u	1.5-3 MeV	c	1.25 GeV	t	174.2 GeV
	d	3-7 MeV	s	95 MeV	b	4.20 GeV

Table 2.2: Leptons and quarks.

The electrically charged leptons are EM and EW interacting particles, neutrinos do only interact weakly. The EW interaction does not conserve parity (P) and it is mediated by γ, $W^{\pm}$ and Z^0. The weak bosons W^+ and W^- only couple to left chiral particles.
To describe the structure of the EW interaction, the weak charge I is introduced. Particles with the same weak charge quantum number are considered identical and are grouped

into multiplets. Table 2.3 lists the EW multiplets and some quantum numbers. The third component of the weak charge I_3 and the electrical charge are related by the Gell-Mann-Nishina formula:

$$Q = \frac{Y}{2} + I_3, \tag{2.1}$$

where Y is called hypercharge.

Particles			Q	Y	I_3
$\begin{pmatrix} \nu_e \\ e \end{pmatrix}_L$	$\begin{pmatrix} \nu_\mu \\ \mu \end{pmatrix}_L$	$\begin{pmatrix} \nu_\tau \\ \tau \end{pmatrix}_L$	0	-1	$+1/2$
			-1	-1	$-1/2$
$\begin{pmatrix} u \\ d \end{pmatrix}_L$	$\begin{pmatrix} c \\ s \end{pmatrix}_L$	$\begin{pmatrix} t \\ b \end{pmatrix}_L$	$+2/3$	$+1/3$	$+1/2$
			$-1/3$	$+1/3$	$-1/2$
e_R	μ_R	τ_R	-1	-2	0
ν_{eR}	$\nu_{\mu R}$	$\nu_{\tau R}$	0	0	0
u_R	c_R	t_R	$+2/3$	-2/3	0
d_R	s_R	b_R	-1/3	$+4/3$	0

Table 2.3: Left and right chiral fermions and quantum numbers.

Although the EM force (light, radio, gamma rays) reaches over an infinite distance, the EW force only acts on scales of 10^{-18} m. The range depends on the mass of the mediating particle (Yukawa hypothesis). Using the Heisenberg uncertainty principle

$$\Delta x \cdot \Delta p \geq \frac{\hbar}{2} \tag{2.2}$$

the range $R = \Delta x$ can be calculated as:

$$R = \frac{\hbar \cdot c}{2 \cdot p}. \tag{2.3}$$

For a mass of 80 GeV the range is around 10^{-18} m, for a massless boson like the γ the range becomes infinite.
Quarks are EM, EW and strongly interacting particles. They cannot exist as free particles on length scales larger than the radius of a proton for instance but are asymptotically free within the proton, because the strong interaction gets weaker at smaller distances or higher energies (asymptotic freedom). The confinement is the consequence of the self-coupling of the gluons, which mediate the strong force. The strong interaction is flavor blind but couples to three color charges: Red, blue and green. Color is another degree of freedom for which the Δ^{++} resonance was one of the first evidences. In the Δ^{++} three u-quarks with the same spin orientation are bound together, but the Pauli exclusion principle forbids fermions having the same quantum numbers. Gluons also carry color charge. There are eight linear combinations of color and anticolor, leading to eight different gluons. On experimentally accessible length scales there are no single partons, but hadrons without color charge (white).
Quarks decay via the EW interaction. The quark flavour eigenstates are not the eigenstates of the EW interaction. Instead every flavor state is a mixture of different mass eigenstates, described by the CKM[1] matrix, also including a CP violating phase.

[1]CKM - Cabibbo Kobayashi Maskawa

Important for the weakly interacting particles is the weak universality. This is a consequence of the fact that all SU(2) doublets couple with the same strength to the gauge bosons of the EW interaction. As a consequence, the branching ratio (BR) for a Z^0 decay to a pair of leptons for instance is almost the same within experimental uncertainties [2]:

$$\begin{aligned} BR(Z^0 \to e^+e^-) &= (3.363 \pm 0.004)\ \% \\ BR(Z^0 \to \mu^+\mu^-) &= (3.366 \pm 0.007)\ \% \\ BR(Z^0 \to \tau^+\tau^-) &= (3.370 \pm 0.008)\ \% \end{aligned} \tag{2.4}$$

2.1.2 Gauge Theory of the Electroweak Interaction

One of the most profound principles of nature is the principle of least action. It is a variation principle meaning that the evolution of a physical system between two states is determined by requiring the action to be minimized.
Action in QFT is a functional S:

$$S = \int d^4x\, \mathcal{L} = \int dt\, d^3\vec{r}\, \mathcal{L}\left(\partial_\mu \Psi, \partial_\mu \bar{\Psi}, \Psi, \bar{\Psi}\right). \tag{2.5}$$

$\mathcal{L}$ is the Lagrangian density describing the system. $\mathcal{L}$ of a relativistic spin 1/2 particle with mass m is given by:

$$\mathcal{L}_0 = \bar{\Psi}\left(i\gamma^\mu \partial_\mu - m\right)\Psi. \tag{2.6}$$

The principle of least action leads to the extended Euler-Lagrange formalism:

$$\delta S = 0 \quad \Rightarrow \quad \frac{\delta S}{\delta \bar{\Psi}} = \frac{\partial \mathcal{L}_0}{\partial \bar{\Psi}} - \partial_\mu \frac{\partial \mathcal{L}_0}{\partial\left(\partial_\mu \bar{\Psi}\right)} = 0. \tag{2.7}$$

Evaluating this last equation leads to the Dirac equation:

$$\left(i\,\gamma^\mu\,\partial_\mu - m\right)\Psi = 0. \tag{2.8}$$

This $\mathcal{L}_0$ is invariant under a global[2] gauge transformation:

$$\begin{aligned} \Psi \to \Psi' &= e^{i\alpha}\Psi \\ \mathcal{L}'_0 &= \mathcal{L}_0. \end{aligned} \tag{2.9}$$

Ψ is not an observable itself - only its absolute value squared - and such transformations do not change the physical behavior of $|\Psi|^2$:

$$|\Psi'|^2 = |\Psi|^2. \tag{2.10}$$

Another possible transformation is the local[3] gauge transformation:

$$\begin{aligned} \Psi \to \Psi' &= e^{i\alpha(x)}\Psi \\ \mathcal{L}'_0 &\neq \mathcal{L}_0. \end{aligned} \tag{2.11}$$

[2]Global means that this transformation is equally performed at every space-time point.
[3]Local means that this transformation is differently performed in particular regions of space-time.

$\mathcal{L}$ is not invariant under a local gauge transformation, but local gauge symmetry is the general principle of all interactions in nature. One can make $\mathcal{L}$ locally symmetric by adding another term:

$$\mathcal{L} = \mathcal{L}_0 + \mathcal{L}_{loc}. \tag{2.12}$$

This is achieved by using the principle of minimal coupling:

$$\partial_\mu \rightarrow \partial_\mu + i\, e\, A_\mu. \tag{2.13}$$

Then the Lagrangian gets the form:

$$\mathcal{L} = \mathcal{L}_0 - e\, \left(\bar{\Psi}\, \gamma^\mu\, \Psi\right) A_\mu = \mathcal{L}_0 - e\, j^\mu A_\mu. \tag{2.14}$$

A_μ is a vector field changing the phase of Ψ and j^μ is a current. Now the local gauge transformation

$$\begin{aligned} \Psi \rightarrow \Psi' &= e^{i\alpha(x)}\Psi \\ A_\mu \rightarrow A'_\mu &= A_\mu - \frac{1}{e}\, \partial_\mu\, \alpha(x) \\ (\mathcal{L}_0 + \mathcal{L}_{loc})' &= \mathcal{L}_0 + \mathcal{L}_{loc} \end{aligned} \tag{2.15}$$

leaves the Lagrangian invariant. A_μ can be identified with the photon. So requiring local gauge symmetry leads to the gauge boson of the EM interaction.
Adding a kinetic term and a mass term for the field A_μ leads to the following complete form of $\mathcal{L}$ for the QED:

$$\mathcal{L}_{QED} = \bar{\Psi}\, (i\gamma^\mu \partial_\mu - m)\, \Psi - e\, j^\mu A_\mu - \frac{1}{4}\, F_{\mu\nu}\, F^{\mu\nu} + \frac{1}{2}\, M_{\gamma^2}\, A_\mu\, A^\mu. \tag{2.16}$$

$F_{\mu\nu}$ is the EM tensor defined as:

$$F_{\mu\nu} = \partial_\mu A_\nu - \partial_\nu A_\mu. \tag{2.17}$$

The mass term $\frac{1}{2}\, M_{\gamma^2}\, A_\mu\, A^\mu$ destroys the local gauge symmetry if $M_{\gamma^2} \neq 0$, but experiments show that indeed the photon mass is $< 10^{-17}$ eV [2]. As a consequence, this Lagrangian cannot describe massive bosons.
A Lagrangian for the weak interaction has to include the $(V-A)^4$ structure of the weak current, meaning that the gauge bosons only couple to left handed particles and right handed antiparticles. In a model world - where only leptons of the first generation exist - there is one left handed doublet and two right handed singlets:

$$\Psi_L = \begin{pmatrix} \nu_e \\ e \end{pmatrix}_L,\ e_R\ \nu_R \tag{2.18}$$

The Lagrangian 2.6 without the mass term $-m\bar{\Psi}\Psi$ then takes the form:

$$\mathcal{L} = \bar{\Psi}_L\, i\, \gamma^\mu\, \partial_\mu\, \Psi_L + \bar{e}_R\, i\, \gamma^\mu\, \partial_\mu\, e_R + \bar{\nu}_R\, i\, \gamma^\mu\, \partial_\mu\, \nu_R. \tag{2.19}$$

To make $\mathcal{L}$ invariant under a local gauge transformation

$$\hat{U} = e^{\frac{i}{2}\, \vec{\alpha}(x)\cdot\vec{\tau}} \tag{2.20}$$

[4]The form of the weak current has the structure of a vector current minus an axial current (V-A).

the following substitutions have to be performed:

$$\begin{aligned} \Psi_L &\rightarrow \hat{U}\,\Psi_L \\ i\,\partial_\mu &\rightarrow i\,\partial_\mu - \frac{g}{2}\,\vec{\tau}\cdot\vec{W}_\mu \\ g\,W_\mu &\rightarrow g\,\hat{U}\,W_\mu\,\hat{U}^+ - i\,\hat{U}\,\partial_\mu\,\hat{U}^+. \end{aligned} \tag{2.21}$$

$\vec{\tau}$ are the three Pauli matrices (τ^1, τ^2, τ^3), $\vec{W}_\mu$ are three vector fields $\left(W_\mu^1, W_\mu^2, W_\mu^3\right)$, g describes the strength of the coupling. The Lagrangian with these substitutions does not include a mass term to conserve the local gauge symmetry.
The electroweak mixing is now performed using 2.1 in operator form, so the EM current gets split:

$$j_\mu^{EM} = e\,\bar{\Psi}\,\gamma^\mu\,\hat{Q}\,\Psi = e\,\bar{\Psi}\,\gamma^\mu\left(\hat{I}_3 + \frac{\hat{Y}}{2}\right)\Psi = J_\mu^3 + \frac{1}{2}\,j_\mu^Y. \tag{2.22}$$

This leads to an (EM + weak) interaction term in the Lagrangian:

$$\mathcal{L}_{EM,w} = -i\,g\,\left(J^k\right)^\mu\,W_\mu^k - \frac{i}{2}\,g'\,\left(j^Y\right)^\mu\,B_\mu. \tag{2.23}$$

k is an index. For $k = 3$, 2.23 describes the neutral current and for $k = 1$, 2, the charged currents. It can be shown that the physical fields are linear combinations of W_μ^3 and B_μ using a rotation matrix:

$$\begin{pmatrix} A_\mu \\ Z_\mu \end{pmatrix} = \begin{pmatrix} \cos\theta_W & \sin\theta_W \\ -\sin\theta_W & \cos\theta_W \end{pmatrix} \cdot \begin{pmatrix} B_\mu \\ W_\mu^3 \end{pmatrix}. \tag{2.24}$$

Similar to QED, A_μ can be identified with the photon, Z_μ with the Z^0 boson. The rotation angle θ_W is the weak mixing angle and has the value $\sin^2(\theta_W) \approx 0.23$. The charged bosons $W^\pm$ belong to the fields $W_\mu^\pm$ which are linear combinations of $W_\mu^{1,2}$:

$$W_\mu^\pm = \frac{1}{\sqrt{2}}\left(W_\mu^1 \mp i \cdot W_\mu^2\right). \tag{2.25}$$

But still the gauge bosons are massless, and this is a contradiction to the experimental result that the weak interaction range is short. So what is missing is a mechanism to make the weak bosons massive but to leave the photon massless, and also to conserve the local gauge symmetry.

2.1.3 Higgs Mechanism

The Higgs mechanism [3; 4] is based on the idea that the former symmetrical vacuum state of nature was unstable and now a stable but asymmetrical state is taken. This actual state leads to massive gauge bosons and fermions.
In the following model the Higgs mechanism of a spontaneously broken global gauge symmetry

$$\begin{aligned} \Phi \rightarrow \Phi' &= e^{i\,\alpha}\Phi \\ \mathcal{L} \rightarrow \mathcal{L}' &= \mathcal{L} \end{aligned} \tag{2.26}$$

is exemplified. The Lagrangian $\mathcal{L}$ has the form:

$$\begin{aligned} \mathcal{L} &= T - V \\ &= (\partial_\mu \Phi)^* (\partial^\mu \Phi) - \left(\mu^2 \Phi^* \Phi + \lambda (\Phi^* \Phi)^2\right). \end{aligned} \tag{2.27}$$

$\mathcal{L}$ consists of three terms: $T = (\partial_\mu \Phi)^* (\partial^\mu \Phi)$ is a kinetic term, the potential V contains a mass term $\mu^2 \Phi^* \Phi$ and the term $\lambda (\Phi^* \Phi)^2$ describing the self coupling of four Φ fields with the strength λ. Φ is a complex field:

$$\Phi = \frac{1}{\sqrt{2}} (\Phi_1 + i \Phi_2). \tag{2.28}$$

If $\lambda = 0$, V is a harmonic potential, but for $\lambda \neq 0$ and $\mu^2 < 0$ and using Equation 2.28, V gets the following form (as displayed in Figure 2.1):

$$V = \frac{1}{2} \mu^2 \left(\Phi_1^2 + \Phi_2^2\right) + \frac{1}{4} \lambda \left(\Phi_1^2 + \Phi_2^2\right)^2. \tag{2.29}$$

V has one local but unstable maximum at $\Phi = (0 + i \cdot 0)$. The minimum is a circle in

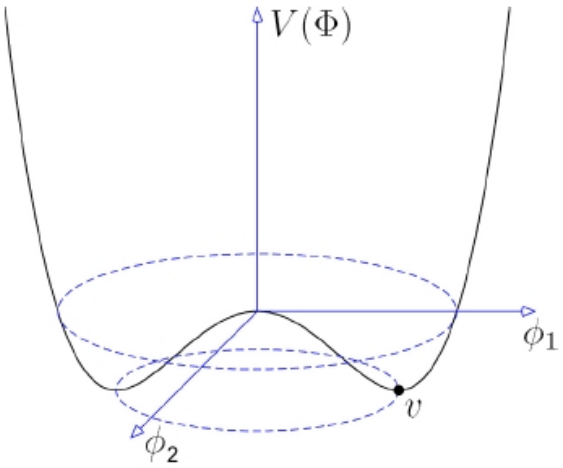

Figure 2.1: Higgs potential V.

the Φ_1-Φ_2 plane and can be calculated as:

$$\frac{\partial V}{\partial \Phi} = 0 \;\Rightarrow\; \Phi_1^2 + \Phi_2^2 = \frac{-\mu^2}{2\lambda} \equiv v^2. \tag{2.30}$$

This can be solved when choosing (for example)

$$\Phi_1 = v, \quad \Phi_2 = 0. \tag{2.31}$$

Now one can apply a small perturbation around the minimum:

$$\Phi(x) \approx \frac{1}{\sqrt{2}} (v + \eta(x) + i \cdot \xi(x)). \tag{2.32}$$

Substituting these terms into 2.27 and neglecting terms with higher orders in the perturbation fields η and ξ leads to:

$$\mathcal{L}' = \frac{1}{2} (\partial_\mu \xi)^2 + \left(\frac{1}{2} (\partial^\mu \eta)^2 + \mu^2 \eta^2\right) + const. \tag{2.33}$$

The term $\mu^2\,\eta^2$ can be interpreted as a mass term for the field η. The mass m_η is then given as:

$$m_\eta = \sqrt{-2\,\mu^2}. \tag{2.34}$$

$\frac{1}{2}\,(\partial_\mu\,\xi)^2$ is the kinetic term for the field ξ. Because the potential V is flat in ξ direction and a mass term corresponding to ξ is missing, one can conclude that this Lagrangian leads to a massless boson, a Goldstone boson. This can even be generalized to the Goldstone theorem [5], saying that every spontaneous breaking of a global gauge symmetry leads to a massless boson. Because no experiment has ever seen such a Goldstone boson this model cannot describe nature. Instead, the breaking of a local gauge symmetry is realized. Furthermore this is preferred by theory, because every local gauge symmetry is renormalizable [6].
In the SM, the Higgs field Φ is a doublet of the $(SU(2)_L \times U(1)_Y)$ EW interaction:

$$\Phi = \begin{pmatrix} \Phi^+ \\ \Phi^0 \end{pmatrix} = \frac{1}{\sqrt{2}} \begin{pmatrix} \Phi_1 + i \cdot \Phi_2 \\ \Phi_3 + i \cdot \Phi_4 \end{pmatrix}. \tag{2.35}$$

Using the same ansatz for the Higgs potential V as in 2.27 leads to the degenerate minimum (a circle in the complex plane):

$$\frac{\partial V}{\partial \Phi} = 0 \;\Rightarrow\; \Phi_{min} = \sqrt{\Phi_1^2 + \Phi_2^2 + \Phi_3^2 + \Phi_4^2} = \sqrt{\frac{-\mu^2}{2\,\lambda}}\, e^{i\,\theta}. \tag{2.36}$$

Usually, $\theta = 0$ is used to fix one vacuum state in the infinite number of states:

$$\Phi_{min}(\theta = 0) \equiv \Phi_{vacuum} = v. \tag{2.37}$$

v is called vacuum expectation value. It is related to the Fermi constant G_F[5] as follows:

$$\frac{G_F}{\sqrt{2}} = \frac{1}{2v^2}. \tag{2.39}$$

G_F can be obtained from the muon decay width. v was then calculated to be $v = 246$ GeV. This vacuum state has been realized in nature which is called spontaneous symmetry breaking.
Now the Higgs field is fixed by using the unitary gauge:

$$\Phi_1 = \Phi_2 = \Phi_4 = 0,\; \Phi_3 = v \;\Rightarrow\; \Phi_0 = \begin{pmatrix} 0 \\ v \end{pmatrix}. \tag{2.40}$$

This choice is motivated by the requirement that the vacuum state has to be neutral. Using the charge generator $\hat{Q}$ (Equation 2.1) on Φ_0 and the properties of the Higgs field, this leads to:

$$\hat{Q}\,\Phi_0 = \left(\hat{I}_3 + \frac{\hat{Y}}{2}\right)\,\Phi_0 = \left(-\frac{1}{2} + \frac{1}{2}\right)\,\Phi_0 = 0. \tag{2.41}$$

[5]The muon decay in LO can be described by the propagation of a W boson. Fermi showed that this can be simplified to one vertex with the coupling constant G_F, given as follows:

$$G_F = \frac{\sqrt{2}}{8} \cdot \left(\frac{g_W}{M_W}\right)^2. \tag{2.38}$$

This way the vacuum stays neutral but it carries a hypercharge and an isospin so that it couples to weak bosons. Furthermore, a different gauge fix would lead to Goldstone bosons. Here the degrees of freedom represented by the Goldstone bosons are absorbed (*eaten up*) by the vector particles $W^{\pm}$ and Z^0, giving them an additional degree of freedom: A longitudinal polarization. Only massive particles with velocities below the speed of light can have longitudinal degrees of freedom. The photon has only a transversal polarization. Now the field $h(x)$ is used as a distortion around this minimum:

$$\Phi_0 = \begin{pmatrix} 0 \\ v + h(x) \end{pmatrix}. \tag{2.42}$$

$h(x)$ is a physical field, the scalar Higgs field of nature. All the elementary particles become massive when interacting with this field, this coupling (Yukawa coupling) is proportional to the mass of the particle. The full Lagrangian contains products of $h(x)$ with the gauge fields W_μ^k and B_μ and this way their masses can be predicted by theory:

$$\begin{aligned} m_{W^\pm} &= v\,\frac{g}{2} \\ m_{Z^0} &= v\,\frac{\sqrt{g^2+g'^2}}{2} \\ m_f &= v\,\frac{\lambda_f}{\sqrt{2}} \\ m_{H^0} &= v\,\sqrt{2\,\lambda}. \end{aligned} \tag{2.43}$$

The Yukawa coupling terms must be added 'by hand' into the Lagrangian, so their Yukawa coupling constants λ_f are inputs to instead of results from the theory.
The Higgs boson H^0 is a massive scalar (spin 0) and the quantized excitation of the Higgs field. So far no direct evidence for its existence has been found, yet its required for the completeness of the SM. The LEP experiment was able to give a lower limit on its mass: m_H>114.4 GeV at 95% confidence level (CL) [7].
A theoretical upper bound on the SM Higgs mass can be given by the requirement of unitarity in the perturbative regime. From the scattering of longitudinal polarized $W^{\pm}$ one can conclude:

$$m_H \leq \sqrt{\frac{2\sqrt{2}}{G_F}} \approx 850\ GeV. \tag{2.44}$$

Considering other scattering processes the upper bound is raised to approximately 1 TeV [8].

2.1.4 SM Higgs Boson Production Processes and Discovery Potential

At LHC there are four main processes for the production of a SM Higgs boson [9]:

- Gluon-gluon-fusion (2.2a)
  The Higgs boson is produced in the fusion of two gluons in a heavy-quark loop. As displayed in the LO diagram, this loop is dominated by top quarks. Important higher order processes are for example $gg \rightarrow H^0\,g$, $g\,q \rightarrow H^0\,q$ and $g\,\bar{q} \rightarrow H^0\,g$. This process has the largest cross section over the allowed mass range.

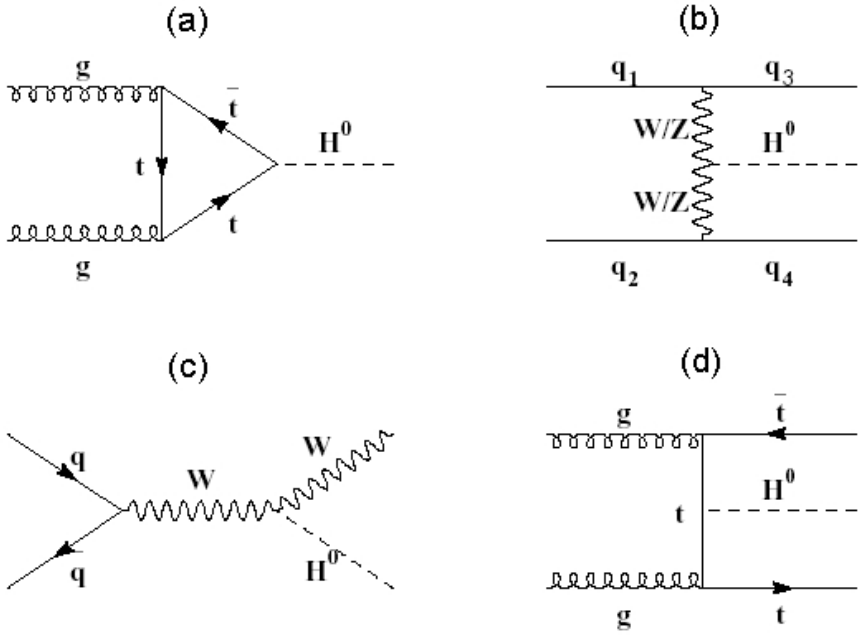

Figure 2.2: LO Feynman diagrams for the main SM Higgs production processes.

- Vector-boson-fusion (VBF) (2.2b)
  In this channel the Higgs is produced by the fusion of two weak vector bosons $W^{\pm}$ or Z^0 which are radiated off quarks. Those quarks will hadronize to jets which can be detected at large values of pseudorapidity (defined in Equation 3.2). This process has the second largest cross section for $m_{H^0} < 800$ GeV.

- Associated production $W^{\pm}H^0$, Z^0H^0 (2.2c)
  Here the Higgs boson is radiated off a weak vector boson (Higgsstrahlung). This process is important in the intermediate mass range $m_{H^0} < 2 \cdot m_{Z^0}$. Its cross section falls rapidly with an increasing value of m_{H^0}.

- Associated production $t\bar{t}H^0$ (2.2d)
  The Higgs production in association with top-pairs is less important because the cross section is about five times smaller than that for $W^{\pm}H^0$ or Z^0H^0 for $m_{H^0} < 200$ GeV. But for light Higgs bosons $t\bar{t}H^0$ is expected to be the only channel where $H^0 \rightarrow b\bar{b}$ is observable.

The LHC will be able to detect a SM Higgs boson over the full kinematic range between the LEP limit and a theoretical upper limit of 1 TeV. In the lower Higgs mass region 110 GeV $< m_{H^0} <$ 130 GeV the dominant decay channel is $H^0 \rightarrow b\bar{b}$, but this cannot be triggered in the gluon-gluon-fusion production mode. The Higgs decay to a pair of photons $H^0 \rightarrow \gamma\gamma$ offers the possibility to get a precise value of the Higgs mass because of a clean signal, although this BR is extremely small compared to the Higgs decay to heavy quarks or vector bosons. For $m_{H^0} < 180$ GeV the Higgs production in weak boson fusion promises good results because of the unique signature of the tagging jets in the detector. The decay channel $H^0 \rightarrow ZZ \rightarrow 4l$ is called the golden channel, because it promises excellently detectable signatures with a flat background in the intermediate mass range

130 GeV $< m_{H^0} <$ 180 GeV.
The results for the expected discovery potential in the range between 100 GeV to 200 GeV at ATLAS is displayed in Figure 2.3 [10; 11]. The combined discovery potential allows a discovery of a SM Higgs boson with more than five standard deviations for an integrated luminosity of 30 fb^{-1} in this difficult mass range. For higher Higs masses the decay modes $H \rightarrow ZZ$ and $H \rightarrow WW$ allow a significant discovery.

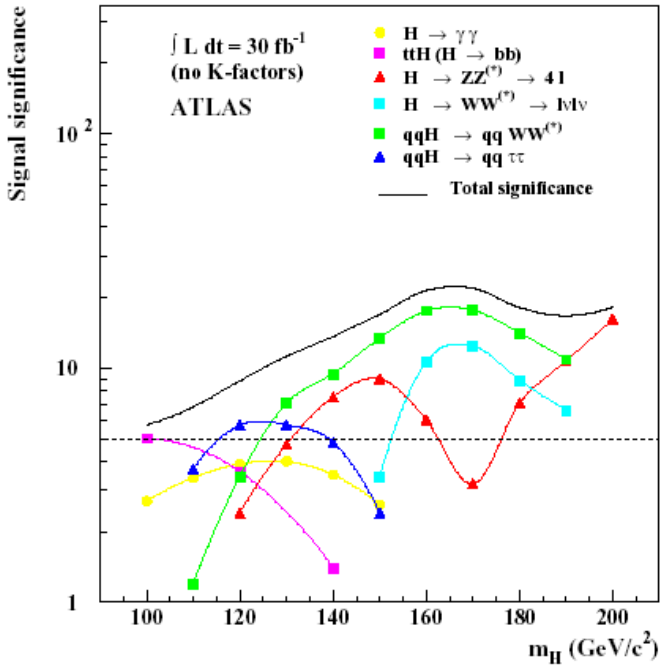

Figure 2.3: Anticipated Higgs discovery potential for various search channels at ATLAS.

2.2 Beyond the Standard Model: Supersymmetry

2.2.1 Supersymmetry and its Motivation

In Supersymmetry the single particle states are extended to supermultiplets containing bosonic and fermionic states. Each of the SM fermions gets one new bosonic superpartner (sfermion) and each boson gets one fermionic superpartner (gaugino or Higgsino).
Supersymmetry is only one possible method to extend the SM. But some aspects make this the most preferred one.

- Hierarchy Problem [12]
  In QFT diverging integrals are often handled by using a cut-off parameter Λ (where the integration is truncated). The mass of a particle is then given by its mass at Born level[6] m_0 and a correction term $\delta m(\Lambda)$:

$$m^2(\Lambda) = m_0^2 + (\delta m(\Lambda))^2. \tag{2.45}$$

[6]Born level is the lowest order in perturbation theory. In the according Feynman graph there are no contributions from higher orders.

Λ is of the order of $\mathcal{O}(\Lambda) \approx 10^{15}$ GeV, the scale where new physics is supposed to appear. Corrections to the Higgs mass come from fermion and scalar loops (Fig. 2.4a), leading to unnatural and large correction values. The Higgs mass at Born level has to be at the scale of EW energy $\mathcal{O}(EW) \approx 100$ GeV[7]. Theoretically it is allowed to fine-tune the mass at Born level but those counter terms must be extremely precise, and this does not come naturally:

$$\mathcal{O}(fine\ tuning) \approx \frac{\mathcal{O}(EW^2)}{\mathcal{O}(\Lambda^2)} \approx 10^{-26}. \tag{2.46}$$

SUSY solves this problem, because in fermion loops also terms from sfermions contribute to the mass correction with an opposite sign (Fig. 2.4b):

$$\delta m^2 \approx \mathcal{O}(\alpha) \cdot |M_{\tilde{f}}^2 - M_f^2| \approx \mathcal{O}(10^{-2}) \cdot M_{SUSY}^2. \tag{2.47}$$

If the masses for fermions and sfermions would be equal, δm^2 would be zero. But because of a mass difference between them, a small rest remains being at the order of the EW mass scale. From this one can conclude that the mass scale for SUSY particles M_{SUSY} is limited to $M_{SUSY} < 1$ TeV.

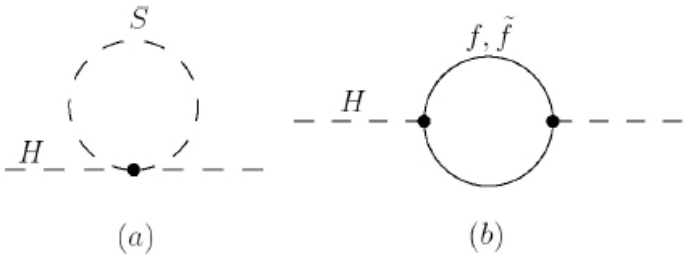

Figure 2.4: Loop corrections to the Higgs mass.

- Grand Unified Theory (GUT)
  An important basis for a theory unifying strong and electroweak interactions is a point of intersection of all coupling constants below the Planck energy. In the SM this is not the case. Heavy SUSY particles would change the coupling constants behavior and lead to this intersection at an energy scale of 10^{15} GeV (GUT scale).

- Dark Matter
  Dark Matter was introduced into physics to solve the galaxy rotation problem. Spiral galaxies rotate with an approximately constant speed also at very high distances from the galaxy centers [13]. This contradicts the prediction of Newtonian dynamics if the visible matter is the only source of the gravitational force. So in addition to the visible mass (eg. stars, gas) galaxies contain invisible dark matter extending into the galaxies halo.
  The SM of cosmology states that only 4% of the universe consists of known matter particles, the rest is hypothetical matter of unknown composition [14]. Since neutrinos are not massless (as implied by neutrino oscillation [15]) they could contribute

[7]The exact value of the EW energy scale is the vacuum expectation value of 246 GeV.

to the dark matter, but they can explain only a small fraction of it.
One hypothetic candidate for cold dark matter is the lightest SUSY particle LSP. As a condition the LSP must be stable. This is achieved by introducing a new discrete symmetry, R-parity P_R:

$$P_R = (-1)^{2s+3B+L}, \tag{2.48}$$

where s is the spin, B the baryon and L the lepton quantum number. SUSY particles have $P_R = -1$, SM particles have $P_R = +1$. A decay of the LSP to SM particles would not conserve P_R and is therefore forbidden. Another consequence of the conservation of P_R is that SUSY particles can only be produced in pairs.

2.2.2 Minimal Supersymmetric Standard Model

The Minimal Supersymmetric Standard Model (MSSM) is the minimal extension of the SM (minimal new particle content, Table 2.4). Particles in the same supermultiplet (for instance the electron e and the selectron $\tilde{e}$) have the same coupling constants and therefore also the same masses, charges, color and isospin:

$$\begin{pmatrix} e_L \\ \tilde{e_L} \end{pmatrix} \Rightarrow \tilde{e_L} = f(Q, Q^+) \cdot e_L. \tag{2.49}$$

$f(Q, Q^+)$ is a function depending on the SUSY operators Q and Q^+ (App. A). In the Higgs sector of the MSSM two Higgs doublets are necessary to avoid gauge anomalies:

$$H_u = \begin{pmatrix} H_u^+ \\ H_u^0 \end{pmatrix} \qquad H_d = \begin{pmatrix} H_d^0 \\ H_d^- \end{pmatrix}. \tag{2.50}$$

Because experiments have not found SUSY particles yet, e.g. a scalar particle at 0.51 MeV (the selectron), SUSY must be a broken symmetry (sparticle masses are much larger than SM masses). The basic idea here is that this must be a soft breaking mechanism to avoid new fine tuning. As a consequence 105 new parameters must be introduced into the theory. These are necessary because the exact breaking mechanism is unknown.
Because the partners of the gauge supermultiplet have the same quantum numbers, they mix. The measured mass eigenstates are linear combinations: Neutralinos χ^0 are mixed states from $\tilde{B}^0$, $\tilde{W}_3^0$ and $H_{u,d}^0$. Charginos $\chi^\pm$ mix from $\tilde{W}^\pm$ and $\tilde{h}_{u,d}^\pm$.
The two Higgs doublets lead to eight mixed states in the higgs sector. It can be shown, that in the MSSM three Goldstone bosons and five Higgs bosons exist. The Goldstone bosons are no physical fields but are merged into the gauge bosons Z^0 and $W^\pm$ and make them massive. The five physical detectable Higgs bosons are the following ones [16]:

h^0	Lightest CP-even scalar MSSM Higgs boson
H^0	Heavier CP-even scalar MSSM Higgs boson
A^0	CP-odd scalar MSSM Higgs boson
$H^\pm$	Charged scalar MSSM Higgs bosons

As a convention from now on Φ labels any of the three neutral Higgs bosons.
The mass of the lightest boson h^0 is constrained to mass values lighter than m_Z:

$$m_{h^0} \leq m_Z \cdot \cos 2\beta. \tag{2.51}$$

Particles			Spin	Partners			Spin
ν_{eL}	$\nu_{\mu L}$	$\nu_{\tau L}$	1/2	$\tilde{\nu}_{eL}$	$\tilde{\nu}_{\mu L}$	$\tilde{\nu}_{\tau L}$	0
e_L	μ_L	τ_L	1/2	$\tilde{e}_L$	$\tilde{\mu}_L$	τ_L	0
ν_R	$\nu_{\mu R}$	$\nu_{\tau R}$	1/2	$\tilde{\nu}_{eR}$	$\tilde{\nu}_{\mu R}$	$\tilde{\nu}_{\tau R}$	0
e_R	μ_R	τ_R	1/2	$\tilde{e}_R$	$\tilde{\mu}_R$	τ_R	0
u_L	c_L	t_L	1/2	$\tilde{u}_L$	$\tilde{c}_L$	$\tilde{t}_L$	0
d_L	s_L	b_L	1/2	$\tilde{d}_L$	$\tilde{s}_L$	$\tilde{b}_L$	0
u_R	c_R	t_R	1/2	$\tilde{u}_R$	$\tilde{c}_R$	$\tilde{t}_R$	0
d_R	s_R	b_R	1/2	$\tilde{d}_R$	$\tilde{s}_R$	$\tilde{b}_R$	0
H_d^0	H_d^-		0	$\tilde{h}_d^0$	$\tilde{h}_d^-$		1/2
H_u^+	H_u^0		0	$\tilde{h}_u^+$	$\tilde{h}_u^0$		1/2
g			1	$\tilde{g}$			1/2
$W^\pm$	W_3^0		1	$\tilde{W}^\pm$	$\tilde{W}_3^0$		1/2
B^0			1	$\tilde{B}^0$			1/2

Table 2.4: Field content of the MSSM.

In higher order corrections of pertubation theory this limit is weakened to around 135 GeV (depending on the top mass). If no Higgs particle is found below that mass, the MSSM is ruled out.
As mentioned before, the MSSM has 105 parameters. But at Born level the properties of the Higgs sector can be given in terms of only two parameters: The mass of the A^0 and $\tan\beta$. The definition of $\tan\beta$ is:

$$\tan\beta = \frac{v_u}{v_d}, \tag{2.52}$$

where v_u and v_d are the vacuum expectation values of the two Higgs doublets. v_u gives mass to up-type fermions (u, c, t, ν), v_d to down-type fermions (d, s, b, e, μ, τ), the gauge bosons coupling λ goes with $v_u^2 + v_d^2 = v^2$. The MSSM Yukawa couplings of the b-quark to the neutral Higgs bosons are:

$$\begin{aligned} \lambda_b &= -\sqrt{2}\cdot\frac{m_b}{v_d}\cdot\frac{\sin(\alpha)}{\cos(\beta)} \qquad \Phi = h^0 \\ &= \sqrt{2}\cdot\frac{m_b}{v_d}\cdot\frac{\cos(\alpha)}{\cos(\beta)} \qquad \Phi = H^0 \\ &= \sqrt{2}\cdot\frac{m_b}{v_d}\cdot\tan(\beta) \qquad \Phi = A^0. \end{aligned} \tag{2.53}$$

Large values of $\tan\beta$ lead to an enhancement of the Higgs coupling to b-quarks and other down-type fermions.
In the SM, the ratio of $t\bar{t}H$ to $b\bar{b}H$ coupling at tree level is given by [17]:

$$\frac{\lambda_t^{SM}}{\lambda_b^{SM}} = \frac{m_t}{m_b} \approx 35. \tag{2.54}$$

In the MSSM this ratio depends on $\tan\beta$:

$$\frac{\lambda_t^{MSSM}}{\lambda_b^{MSSM}} = f_\Phi(\alpha)\cdot\frac{1}{\tan(\beta)}\cdot\frac{m_t}{m_b}. \tag{2.55}$$

α is the mixing angle between the weak and the mass eigenstates of the neutral Higgs bosons, $f_\Phi(\alpha)$ is given by:

$$\begin{aligned} f_\Phi(\alpha) &= -\cot(\alpha) \quad \Phi = h^0 \\ &= \tan(\alpha) \quad \Phi = H^0 \\ &= \cot(\alpha) \quad \Phi = A^0. \end{aligned} \tag{2.56}$$

This suggests that high $\tan\beta$ values around 35 are natural, because then it follows:

$$\frac{\lambda_t}{\lambda_b} \approx 1. \tag{2.57}$$

2.2.3 MSSM Higgs Search and Benchmark Scenarios

In the MSSM Higgs production and decay modes other than in the SM become important, depending on the MSSM parameter values. The $\Phi \to ZZ$ and $\Phi \to WW$ decay channels are dominant in the SM Higgs sector with Higgs masses below 160 GeV. In the MSSM they are suppressed for H^0 and h^0 and even absent for the A^0 (in CP-conserving models), instead the decays $\Phi \to \tau^+\tau^-$ and $\Phi \to t\bar{t}$ are important. Higgs decays to second generation fermions $\mu^+\mu^-$ and third generation quarks $b\bar{b}$ are also promising. Those channels allow the separation of the three neutral Higgs bosons at certain parameter values due to the good mass resolution. Charged Higgs bosons lighter than the top are produced in top decays $t \to H^+ b$ and can be found in $H^\pm \to \tau\nu$ for instance. The b-quark associated Higgs production $b\,\bar{b} \to \Phi$ or $g\,b \to \Phi\,b$ is enhanced for large values of $\tan\beta$. So production modes as displayed in Figure 2.5 become relevant in the MSSM.

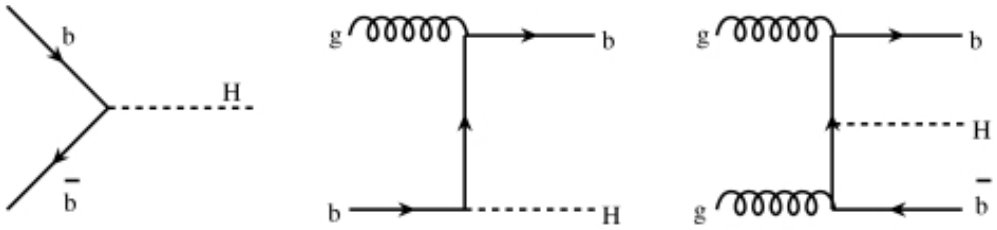

Figure 2.5: Possible graphs for the b-quark associated Higgs production.

In NLO the following five parameters (in addition to m_A and $\tan\beta$) describe the Higgs sector of the MSSM:

M_{SUSY}	Energy scale of SUSY breaking (mass scale of sfermions at EW scale)
M_2	Gaugino mass at EW scale
μ	Strength of the supersymmetric Higgs mixing
$m_{\tilde{g}}$	Gluino mass
X_t	Stop mixing parameter

Furthermore, several benchmark scenarios have been suggested for the Higgs search [18]. The different scenarios exemplify the discovery potential and different features of the

MSSM parameter space, such as maximal m_h values and the suppression of certain production channels. In the benchmark scenarios the enumerated five parameters are fixed and only m_A and $\tan\beta$ are free. The scenarios mainly influence the allowed mass range of the lightest Higgs boson h^0. In Table 2.5 the four main scenarios, the fixed parameters and the maximal m_h value are listed.

Parameters [GeV]	m_h^{max}	nomixing	gluophobic	small α_{eff}
M_{SUSY}	1000	2000	350	800
M_2	200	200	300	500
μ	200	200	300	2000
$M_{\tilde{g}}$	800	8000	500	500
X_t	2000	0	-750	-1100
$max.\ m_h$	133	116	119	123

Table 2.5: Parameters of the benchmark scenarios.

LEP searched for the neutral MSSM Higgs bosons in all four scenarios and was able to find constraints in the m_A-$\tan\beta$ plane. Figure 2.6 shows the results for the m_h^{max}scenario [19]. The green marked regions of m_A, $\tan\beta$ and m_t are excluded by at least 95% CL. The left plot was made for a fixed top mass of 174.3 GeV.

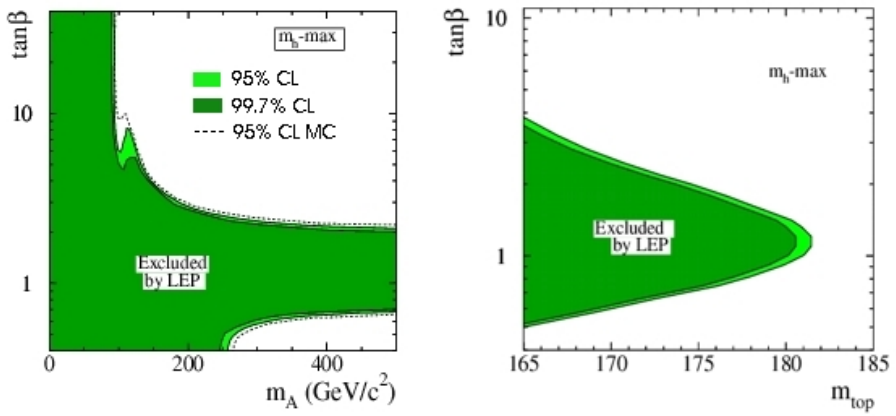

Figure 2.6: LEP results for neutral MSSM Higgs search in the m_h^{max}scenario.

The analysis of the b-associated Higgs production in this thesis is performed in the m_h^{max}scenario. Parameters such as cross sections and Higgs masses are discussed in Section 4.2.1.

2.2.4 Sensitivity to SUSY

A direct discovery of SUSY particles would confirm SUSY. But there are other quantities which are sensitive to processes involving contributions from SUSY particles. Two important quantities are described below:

- Anomalous magnetic moment of the muon [20]
  The anomalous magnetic moment of the μ is given by:

$$a_\mu = \frac{g-2}{2} \tag{2.58}$$

g is the Landé factor of the μ. Most precise measurements have found $a_{exp} = (11659208 \pm 6) \cdot 10^{-10}$ [21]. A comparison with the prediction of the SM shows a deviation from the expected value of 2.3 σ:

$$a_{exp} - a_{SM} = (23.0 \pm 10.0) \cdot 10^{-10}. \tag{2.59}$$

This difference can be understood if SUSY contributions from smuon-neutralino and sneutrino-chargino loops are taken into account.
This also leads to a prediction of the SUSY mass scale. Using a simplified SUSY model where all SUSY particles have the same mass $\tilde{m}$, $a_{SUSY} - a_{SM}$ takes the form:

$$a_{SUSY} - a_{SM} \simeq 13 \cdot 10^{-10} \cdot \tan(\beta) \cdot \left(\frac{100\ GeV}{\tilde{m}} \right)^2 . \tag{2.60}$$

Using $\tan\beta$ values around 35 and $\tilde{m} = 100$ GeV for example, leads to $a_{SUSY} - a_{SM} = 455 \cdot 10^{-10}$. As a consequence, such small SUSY masses can be excluded for values of $\tan\beta \leq 35$.

- Top mass
  The phenomenological features of any Higgs sector are tied to the still not precisely known mass of the top quark. The most recent result from the Tevatron is $m_t = 170.9 \pm 1.8$ GeV [22]. The top as a heavy elementary fermion near the EW symmetry breaking scale has a large Yukawa coupling term to the Higgs field. In higher orders of perturbation theory, the mass of the W boson depends on the top mass and the SM Higgs mass. So, precise measurements of m_W and m_t could be used to discriminate between the SM and a non-minimal model. Cross sections, for instance for the production of top pairs are not yet precisely measured either. Values higher than the SM expectation could imply SUSY models, but so far there are no significant differences due to a lack of precision.

Other particle decay processes such as $b \rightarrow s + \gamma$ or $B^+ \rightarrow \tau^+ + \nu$ are also sensitive to Supersymmetrie.

Chapter 3

The ATLAS Experiment

3.1 The Large Hadron Collider

The Large Hadron Collider (LHC) is located at the border between Switzerland and France. As displayed in Figure 3.1, there are 4 detectors along the proton-proton collider ring.

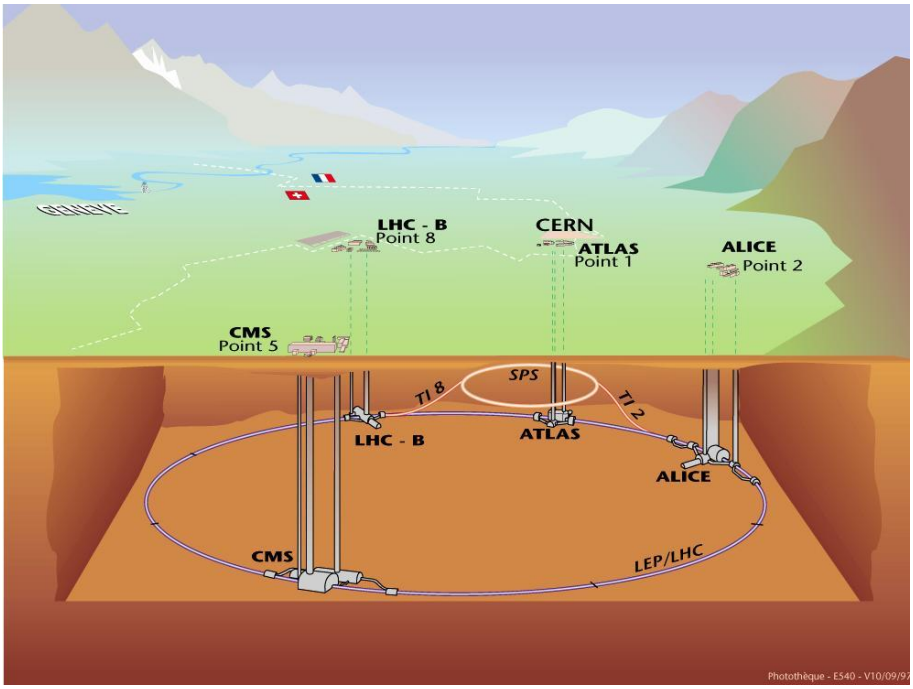

Figure 3.1: Scheme of the LHC.

ATLAS and CMS[1] [23] are both multi-purpose detectors and will be able to search for the Higgs boson and supersymmetric particles. They are also capable to perform electroweak precision measurements. Due to different detector concepts both experiments can confirm each other's findings. The other two experiments are designed to explore other fields of particle physics: LHC-b [24] is intended for measurements of B meson decays and CP

[1] Compact Muon Solenoid

violation effects, Alice[2] [25] will be used for heavy ion collisions and will have access to the quark gluon plasma as it existed in the early universe.
LHC is a synchrotron with a diameter of 8.6 km and with two proton beams running into opposite directions. Each beam will have an energy of 7 TeV when brought to collision and will contain about $3 \cdot 10^{14}$ protons which are obtained from a hydrogenic source. The particles are pre-accelerated to 50 MeV in the *Linac* and gain more energy in the *Booster*, *PS*[3] and *SPS*[4] . They will have an energy of 0.45 TeV when being injected into the LHC [9]. The filling will take about 260 s [26].
The acceleration is achieved by a 400.8 MHz high-frequency field where the protons will experience a maximal voltage of 2 MV/m. 1232 LHC dipoles and 3700 multipole corrector magnets will keep the two beams on their circular path. The field strength of the dipoles depends on the beam energy. At injection it is about 0.5 T and it will rise to the maximum value of 8.3 T at 7 TeV beam energy. The superconducting coils work at a temperature of 1.9 K, cooled by superfluid helium encased in a cryostat.
The protons are grouped into bunches, running with a time distance of 25 ns. In every bunch $1.1 \cdot 10^{11}$ protons will be gathered. There will be 2835 filled bunches running in the LHC with a bunch crossing rate of 40 MHz. In the beginning the anticipated luminosity is 10^{33} cm^{-2}s^{-1} with one proton-proton interaction per bunch crossing. Later a luminosity of 10^{34} cm^{-2}s^{-1} with an average number of 23 proton-proton interactions per crossing is expected.

3.2 Coordinates

The space coordinates x, y and z form a right-handed system defined as follows: The coordinate origin is the interaction point. The beam direction corresponds to the z axis, the x-y plane is the transverse plane to the beam direction. The positive x-axis points from the interaction point of the two proton beams to the center of the LHC ring, the y axis points upwards to the ground.
To describe particle positions within the detector cylindrical coordinates are used: The radius R, the azimuthal angle ϕ given by

$$\tan(\phi) = p_y/p_x \tag{3.1}$$

and the pseudorapidity η, defined as:

$$\eta = -\ln\ \tan\theta/2. \tag{3.2}$$

The polar angle θ is defined as:

$$\cot\theta = p_z/p_T\ , \tag{3.3}$$

where p_T is the transverse momentum, given by:

$$p_T = \sqrt{p_x^2 + p_y^2}. \tag{3.4}$$

[2]A Large Ion Collider Experiment
[3]Proton Synchrotron
[4]Super Proton Synchrotron

To describe the direction of the particles momentum with respect to the z-axis, η is used instead of θ. This is because in QCD events the number of particles produced is approximately constant as a function of η. A sketch with the coordinates, angles and η is displayed in Figure 3.2.

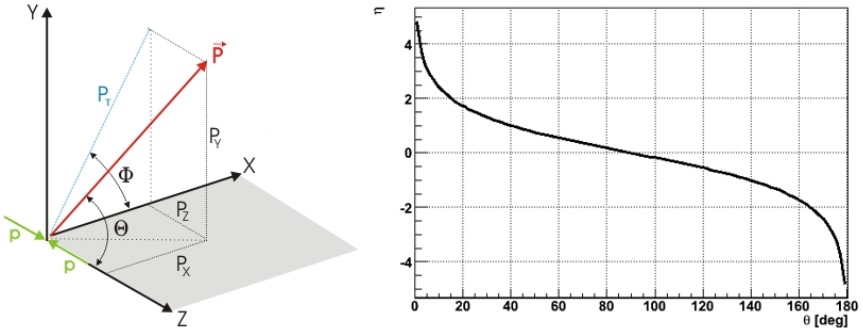

Figure 3.2: Coordinates and angles (left), Pseudorapidity η vs. θ (right).

The transverse momentum p_T and transverse energy E_T are more reliable kinematic variables than $\vec{p}$ or $\vec{E}$, because the partons carry an unknown fraction of the protons momentum. Using momentum conservation in the transverse plane, the components of the missing p_T ($p_{T,miss}$) are defined as:

$$p_{x,miss} = -\sum_{particles} p_x \qquad (3.5)$$
$$p_{y,miss} = -\sum_{particles} p_y.$$

3.3 The ATLAS Detector

3.3.1 General Layout

The ATLAS detector has a cylindrical design with a length of 44 m, a diameter of 22 m and a weight of 7000 t. It is located 92 m below the ground of Point 1 at CERN. In Figure 3.3 the detector is shown; the main components are marked and described below.
ATLAS is a multi-purpose detector but its primary goal is the discovery of new physics. In ref. 27 the Higgs search is emphasized as being a first benchmark for the detector concept. ATLAS is also capable of precise measurements of properties of known particles [28]. The detector is mainly optimized for the identification of electrons and photons and the high precision measurement of muon momenta. This is achieved by the electromagnetic calorimeters and the muon chambers. Sophisticated triggers and computing systems were developed to filter and store interesting data.

3.3.2 The Inner Detector

Being closest to the interaction point, the inner detector (ID) as shown in Figure 3.4 consists of the pixel detector and at outer radii the semiconductor tracker (SCT) and the transition radiation tracker (TRT) . A solenoidal field of 2 T allows for the measurements

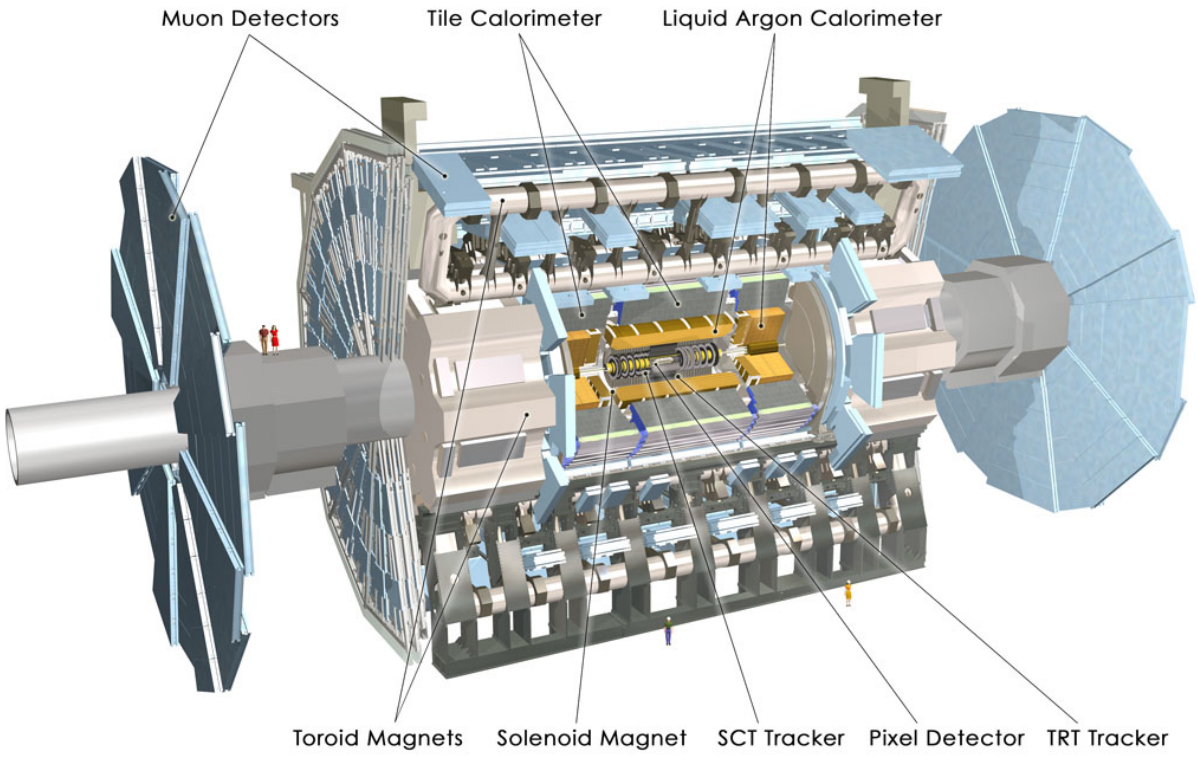

Figure 3.3: The ATLAS detector.

of particle momenta. The ID covers the pseudorapidity region $\eta = \pm 2.5$ and extends 7 m in length and 1.15 m in radius. An approximate form for the p_T resolution of muons in the ID is given by [28]:

$$\sigma\left(\frac{1}{p_T}\right) = 0.36 + \frac{13}{p_t \cdot \sqrt{\sin\theta}} \quad (\mathrm{TeV}^{-1}) \,. \tag{3.6}$$

The first (constant) error term comes from multiple scattering, the second describes the Sagitta resolution.
The pixel detector has a very high granularity and is dedicated to measure the impact parameter, tracks and to find short-lived particles, like B hadrons or τ leptons. A total of 140 million detector elements are ordered in three barrels and five disks on each side. The innermost barrel layer is located at $R = 5.05$ cm, the second layer at $R = 8.85$ cm and the third at $R = 12.25$ cm, the disks are located between $z = 59$ cm and $z = 65$ cm. Each pixel works like a semiconductor diode in reverse-biasing mode and with a high voltage field between its electrodes: Charged particles produce pairs of electrons and holes, they get separated by the electrical field and accumulated on the electrodes.

The SCT is designed to contribute to the measurement of momentum, impact parameter and the vertex position of charged particles. It is comprised of silicon microstrip modules, located on a four layer barrel and nine disks in each direction. The modules contain strips on both sides and are being twisted by an angle of 40 mrad to allow precise measurement of the z coordinate and to eliminate ghosts (signals identified by mistake). The silicon strips operate the same way as the pixels, as semiconductor diodes.

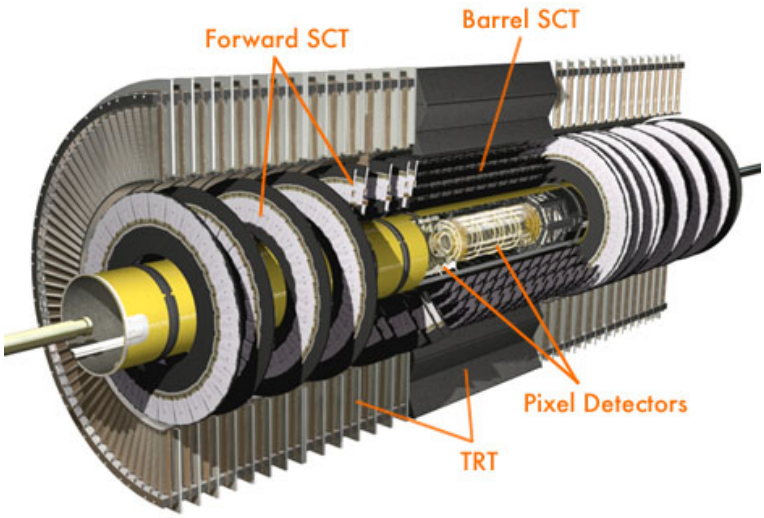

Figure 3.4: The inner detector.

The outer tracker is a combined straw tube tracker and transition radiation detector. It consists of one barrel and two end-caps. The barrel alone is build from 52 544 straw tubes with 4 mm in diameter and maximum 144 cm in length. A total of 298 304 tubes are filled with 3 m^3 of a gas mixture of 70% Xe, 20% CO_2 and 10% CF_4. Each tube contains a gold-plated tungsten wire in the middle. Between the tubes and the wires is a strong electric field. When a charged particle passes through the tubes, the gas gets ionized. Then the ions and electrons from the gas move towards the electrodes causing secondary ionization. Those charge carriers lead to a voltage pulse getting recorded.
Between the straw tubes are foils of polyethylene and polypropylene. Charged particles passing through those foils will emit transition radiation because of the different di-electrical constants of the foils. Especially electrons can be identified this way [29]. The outer tracker provides on average 35 two-dimensional measurement points with less than 0.15 mm resolution for charged particle tracks with $|\eta| < 2.5$ and $p_T > 0.5$ GeV [30].

3.3.3 The Calorimeters

A view of the ATLAS calorimeters is presented in Figure 3.5. The calorimeter consists of an electromagnetic (EM) calorimeter covering the pseudorapidity region $|\eta| < 2.5$, a hadronic calorimeter covering $1.5 < |\eta| < 3.2$ and forward calorimeters covering $3.1 < |\eta| < 4.9$.
A calorimeter's purpose is to measure the particle energy. Particles enter the calorimeter and initiate a particle shower. The EM calorimeter is more sensitive to EM interacting particles, in hadronic calorimeters strongly interacting particles can be measured. The hadronic calorimeter is located at outer radii and is supposed to absorb as many particles as possible inhibiting a punch through into the muon system. The particles energy is deposited in the calorimeter, collected and measured. By separating the calorimeter in small segments both longitudinal and transversal, the particle track and its identity can be detected.

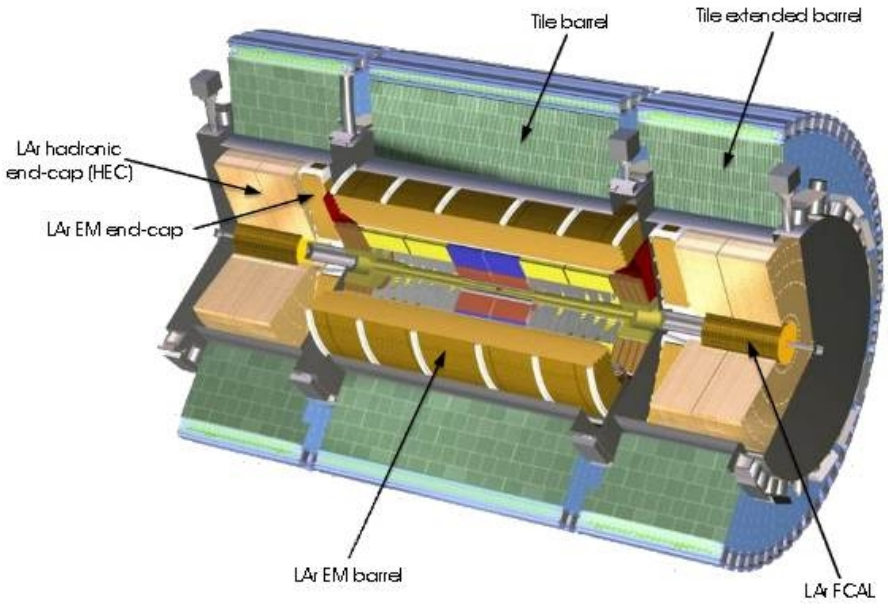

Figure 3.5: The calorimeter system.

The EM calorimeter is divided into a barrel part and two end-caps. It is a lead liquid argon (LAr) detector with accordion-shaped Kapton[5] electrodes and lead absorber plates over its full coverage. The accordion geometry provides complete ϕ symmetry without azimuthal cracks.
Over the region of $|\eta| < 2.5$ the EM calorimeter is segmented into three longitudinal sections. The strip section is equipped with narrows strips acting as a 'preshower' detector, enhancing particle identification. The middle section is transversally segmented into square towers of size $\Delta\eta \times \Delta\phi = 0.025 \times 0.025$. The back section has a granularity of 0.05 in η. The end cap has a coarser granularity, which is sufficient for measurements of $E_{T,miss}$ and jet reconstruction.
The estimated energy resolution for electrons and photons in the EM calorimeter follows the function [28]:

$$\frac{\sigma(E)}{E} \approx \frac{0.1\ \sqrt{\text{GeV}}}{\sqrt{E}}. \tag{3.7}$$

The hadronic calorimeter consists of a tile calorimeter, the LAr hadronic end-caps (HEC) and the LAr forward calorimeters (FCAL) .
The tile calorimeter is composed of one barrel and two extended barrels. It is a sampling calorimeter using iron as absorber and scintillating tiles as active material. A scintillator is a substance that absorbs the radiation from a particle and then fluoresces photons at a characteristic wavelength, releasing the previously absorbed energy.
The two HEC, one in each z direction, consist of two independent copper wheels. Each wheel is build out of 32 modules and a central ring. The wheels have a mass of 67 tons or 90 tons.
The FCAL consist of three sections, one is made of copper and the other two are made out of tungsten. The metal matrix is filled with LAr as sensitive medium.

[5]Kapton is the trade name for a high-end thermoplastic made of polyimide.

3.3.4 The Outer Detector

The outermost detector component is the muon spectrometer. Due to their relatively long lifetime of $2.2 \cdot 10^{-6}$ s and their electroweak nature, muons pass trough the whole detector. They are 207 times heavier than electrons and so they loose less energy through bremsstrahlung. The energy depositions mass dependance is given by the Bethe-Bloch-Formula:

$$\frac{dE}{dx} \propto \frac{1}{m^2} \,. \tag{3.8}$$

The ATLAS muon system has its own magnetic system. The eight toroid magnets work with superconducting coils and an air-core and bend muon tracks within $|\eta| < 1.0$. In regions with $1.4 < \eta < 2.7$ muons tracks are bent by two smaller end-cap magnets inside the barrel toroid. Within $1.0 < \eta < 1.4$ (the 'transition region') there is a combination of the two magnetic systems. This allows a magnetic field structure being mostly orthogonal to the muon trajectories.
The outer detector is instrumented with separate trigger and high-precision tracking chambers. They are optimized against radiation background mostly coming from neutrons and photons, arising from secondary interactions with shielding material or the beam pipe.
The muon detector consists of a barrel in the central region and end-caps on each side. There are three layers in the barrel with optimized locations for the momentum reconstruction. Each end-cap consists of four disks with different distances between them.
In the barrel, tracks are measured in chambers around the beam axis, in the other regions those chambers are installed vertically. The muon track coordinates are mostly measured by Monitored Drift Tubes (MDTs) . MDTs are tubes made of aluminium filled with gas at a pressure of 3 bar. In the innermost layer for the region $2 < |\eta| < 2.7$ Cathode Strip Chambers (CSC) with higher granularity are used to also shield against backgrounds. CSCs are multiwire proportional chambers with cathode strip readout.
The trigger function is provided by Resistive Plate Chambers (RPCs) in the barrel and Thin Gap Chambers (TGCs) in the end-caps. RPC units are parallel plates, filled with a gas mixture of $C_2H_2F_4$ and SF_6 at low voltage. TGCs are similar to multiwire proportional chambers filled with CO_2 and C_5H_{12}.
The positions of the muon chambers are constantly monitored. Misalignment occurring during operation can thus be corrected in offline analysis. This is to ensure the high precision of the muon momentum measurements. Over a p_T range from ca. 10 GeV up to 100 GeV the muon momentum resolution is about 2 % [28].

3.4 Data Processing

3.4.1 Trigger

Starting from an interaction rate of 10^9 Hz, the trigger is supposed to reduce this by a factor of 10^7 for permanent storage. This must be optimized for rejection against minimum-bias[6] events but keeping rare events of new physics.
The trigger consists of three levels. Level-1 (LVL1) is a hardware trigger and makes a first selection by using only some detector information. High p_T muons are identified by the

[6] A minimum-bias event is what one would see with a totally inclusive trigger [31].

RPCs and TGCs of the muon spectrometer. Information with reduced granularity is taken from the calorimeters. Triggered objects are high p_T electrons, photons, jets, τ-leptons and a large $E_{T,miss}$. LVL1 selects events with a rate of 75 kHz and forwards its data to so-called pipeline memories. From there the data goes on to the readout drivers (RODs) and further to the 1700 readout buffers (ROBs). Since especially for the muon chambers, information is collected in the ATLAS detector while the next interesting bunch-crossing is already on-going, the latency time of LVL1 must be kept as small as possible.
The ROBs hold information as long as the event has not been rejected by the Level-2 trigger (LVL2). LVL2 is a firmware trigger evaluating events with respect to η, ϕ and p_T of the particles and $E_{T,miss}$. LVL2 is supposed to reduce the data rate to 1 kHz.
If an event passes LVL2, the data goes on the event filter (Level-3 trigger) and the data storage. The event filter is based on offline algorithms reducing the storage rate to 100 MB/s. Its tasks are to confirm the LVL2 decision and applying more complex algorithms for vertex fitting and bremsstrahlung recovery.

3.4.2 Grid Computing

Grid computing is an emerging computing model that treats all resources as a collection of manageable entities with common interfaces. It makes use of not needed resources of large numbers of disparate computers. In difference to clusters, grid computing focuses on the ability to support computation across administrative domains [32].
For both simulation of events in ATLAS and offline analysis of experimental data, grid computing is essential to success. The anticipated data volume from all LHC experiments is about 15 PByte every year [33]. To process and store this data about 150000 of today's fastest CPUs[7] are required. The concepts of grid computing and distributed analysis make this possible and allow many users everywhere to benefit from the data.
In the LHC Computing Grid Project (LCG) all the participating CPUs are grouped into five different categories, so-called Tiers. Tier architecture is a client-server architecture in which an application is split into several discrete components.
CERN works as TIER-0, where the data processing starts and all the raw data gets backuped. All four LHC experiments will contribute their data. The TIER-0 passes its data to several TIER-1s, which are big international computing centers. Germany's TIER-1 is the Computing Centre Karlsruhe (GridKa) . TIER-2s are less powerful national centers where also MC production and event summary data (ESD) analysis takes place. The German institute DESY for example serves as TIER-2. Smaller computer farms or clusters from institutes or universities will serve as TIER-3. Finally, the end-users will evaluate the data on single desktop computers (TIER-4).
Similar to the World Wide Web, in the future grid computing will not only be constrained to high energy physics but might support other areas of science and could also be opened to the general public.

[7] Central Processing Unit

Chapter 4

Tools & Datasets

4.1 Event Generation and Simulation

The events for this analysis have been generated using MC techniques. The event generation is basically divided into the following steps [34]:

- Matrix element (ME) calculation
  The matrix element of the hard process[1] and the following decay is the basis for the whole event. The ME is the probability of the interactions as function of momenta and energies of the participating partons at a fixed order of the coupling parameter. Usually the whole phase space of possibilities is considered, but appropriate cuts on interesting regions of the phase space can speed up this step. An important input to the ME calculation are the parton density functions (PDF). They influence for example the cross section.

- Underlying event
  Besides the hard process, other partons of the same protons may interact and produce other particles. Those additional interactions are called underlying event and must be added to the event generation for a realistic result.

- Parton shower
  Initial and final state parton showers must be added to the hard process and also to the underlying event. They are modeled by approximate calculations at higher orders which regularize collinear and soft emission divergences.

- Hadronization
  Finally, the outgoing partons must be converted into colorless objects (particles and jets). A jet is a narrow cone of hadrons coming from the hadronization process of the parton. From the direction and four momentum of the jet one can draw conclusions about the properties of the parton.

- Pile up
  At high luminosity of 10^{34} $\mathrm{cm}^{-2}\mathrm{s}^{-1}$ an average of 23 proton-proton interactions are expected during one bunch crossing. Many collision will interleave with each other

[1] Hard process is called the hardest interaction between two partons.

at the same time (pile up).
This analysis makes only predictions for the first years of LHC running with an initial luminosity of 10^{33} cm^{-2}s^{-1}.

After the event generation, the calculation of the four momenta of the particles is finished. This information is also called MC truth or truth information. The final state particles truth data is fed into an ATLAS simulation tool after the event generation.
In principle this simulation proceeds in three steps using GEANT [35]:

- Simulation of detector response
  In the simulation all the detector layers' and materials' responses to traversing particles is calculated using MC techniques. Also misalignments and maintenance materials are included into the full simulation.

- Digitalization
  Here the output of the simulation is converted into digits like they are to be expected from the real detector (times and voltages).

- Reconstruction
  Reconstruction is the process where the raw data digits are reconstructed into tracks and energy deposits.

Running this full chain of data processing takes about 10-15 min per event on a CPU which is usually used today.
An alternative simulation tool is provided by the fast simulation package ATLFast [36], which is ca. 10^3-10^4 times faster than the full chain. ATLFast does not simulate all the detector parts and their response. Instead, it smears the truth information directly using the resolutions (mainly Gaussian functions) measured in the full simulation. For reliable results ATLFast has to be validated against the full simulation of GEANT. A detailed overview over the ATLFast objects and methods is given in [37].
In this analysis all event generation samples have been processes using ATLFast.

4.2 b-quark associated Higgs Production

4.2.1 $\mathbf{m_h^{max}}$ Parameter Values from Feynhiggs

The analysis of the process $b\bar{b}\,h/A/H \rightarrow \tau\,\tau \rightarrow 2\,\ell{+}4\,\nu$ is performed in the $\mathrm{m_h^{max}}$-scenario. Before starting the event generation, certain parameters such as cross sections, branching ratios, decay widths and the masses of h^0 and H^0 must be obtained from theory. For this the tool Feynhiggs [38] Version 2.5.1, has been used. Table 4.1 shows the Feynhiggs default input parameter values for the $\mathrm{m_h^{max}}$scenario that have been used in this thesis.
The three Higgs bosons A^0, H^0 and h^0 have been simplified to one effective boson Φ_{eff}. This is motivated by an important feature of the $\mathrm{m_h^{max}}$scenario: At least two Higgs bosons are nearly degenerate in mass for large values of $\tan\beta$, so that they can be treated as one boson. Figure 4.1 shows the masses of the CP even Higgs bosons as function of m_A at $\tan\beta$=20. The total decay widths Γ_A, Γ_H and Γ_h are also shown in Figure 4.1.
For $m_A > 130$ GeV, A^0 and H^0 are degenerate in mass and h^0 is negligible because of a comparatively small cross section. For $m_A < 130$ GeV, A^0 and h^0 are degenerate and H^0

Parameter	Value [GeV]
m_t	172.5
m_b	4.7
m_W	80.404
m_Z	91.1875
M_{SUSY}	1000
X_t	2000
M_2	200

Table 4.1: Default Feynhiggs m_h^{max}input parameter values.

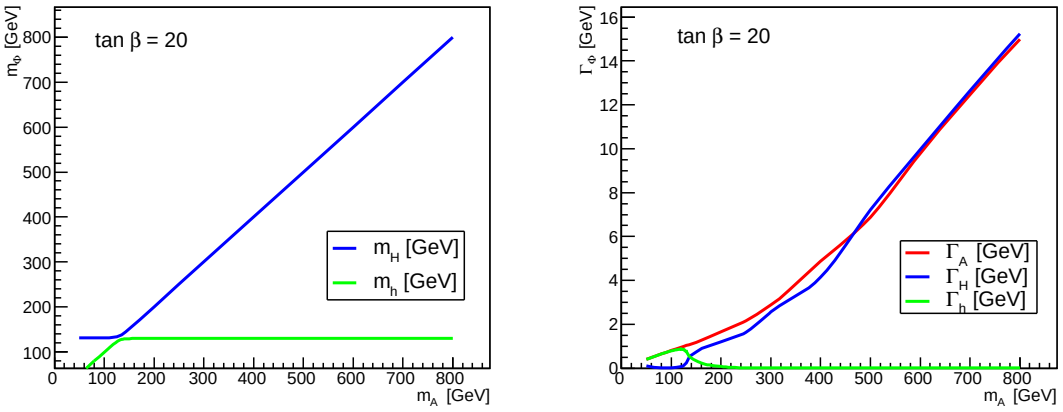

Figure 4.1: Feynhiggs predictions for Higgs masses (left) and total decay widths (right) as function of m_A.

is not important. The mass of the effective boson Φ_{eff} is the value of m_A. In the intense coupling region at $m_A \approx 130$ GeV all three neutral Higgs bosons are almost degenerate in mass for large values of $\tan\beta$.
In Figure 4.2 the cross sections for the b-quark associated Higgs production are displayed. A strong dependence on m_A is evident. At $m_A = 130$ GeV all three cross sections become comparable.
Since the Yukawa couplings to b-quarks (Formula 2.53) is proportional to $\tan\beta$, the cross section for A^0 and H^0 show a quadratic dependency on $\tan\beta$:

$$\sigma_{b\bar{b}\,A/H} \propto \tan^2\beta. \tag{4.1}$$

The cross sections for the neutral Higgs bosons used in this analysis are also calculated by Feynhiggs. The programm uses NNLO SM cross sections [17] and reweights them to MSSM values:

$$\sigma_{MSSM} = \sigma_{SM} \cdot \frac{\Gamma^{MSSM}_{A\to b\bar{b}}}{\Gamma^{SM}_{H\to b\bar{b}}}. \tag{4.2}$$

This is based on the idea, that in the limit of heavy supersymmetric partners, their virtual contributions are insignificant and the predictions for SUSY Higgs bosons can be obtained by rescaling the SM values with the proper coupling constants to MSSM cross sections.
In this work the Higgs bosons decay to $\tau\tau \rightarrow 2\,\ell + 4\,\nu$. The BRs $\Phi \rightarrow \tau\tau$ vs. m_A and

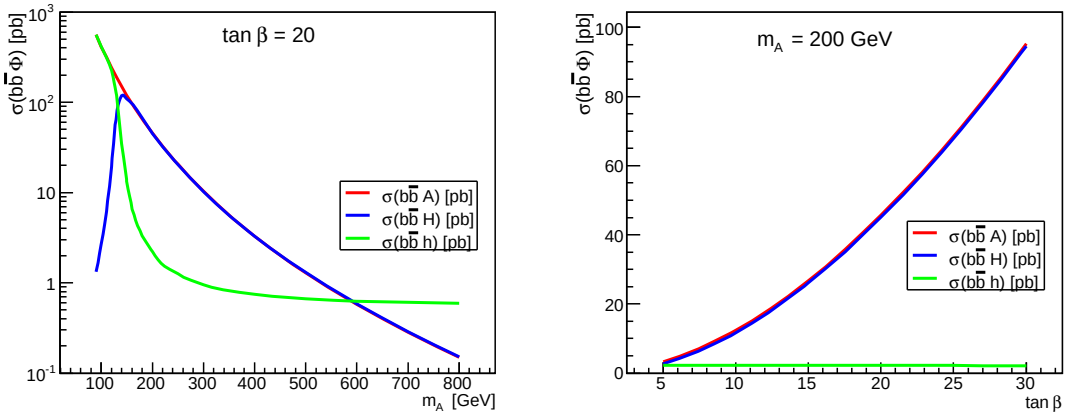

Figure 4.2: Feynhiggs predictions of the cross sections $b\bar{b}\Phi$ as function of m_A and $\tan\beta$.

$\tan\beta$ are plotted in Figure 4.3. The Higgs decay to two τ-leptons is a very important

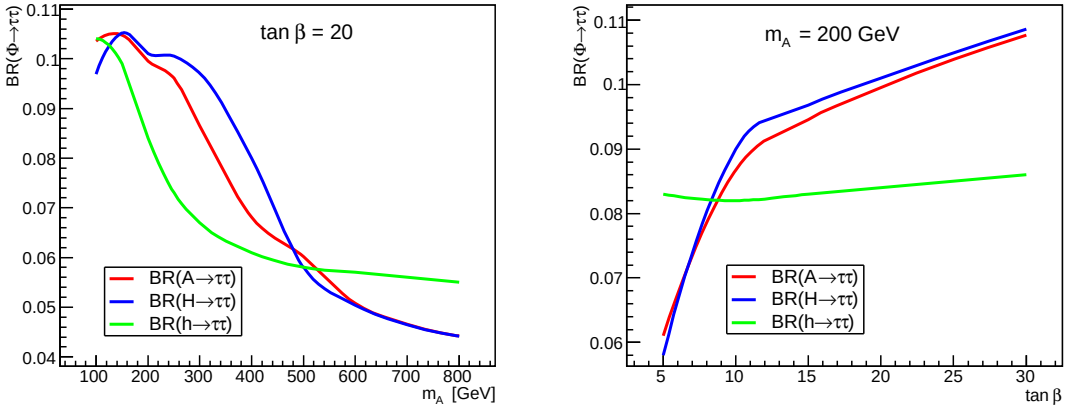

Figure 4.3: Feynhiggs predictions for $BR(\Phi \to \tau\tau)$ as function of m_A (left) and $\tan\beta$ (right).

channel due to the relatively large BR for low masses and high $\tan\beta$.
The BR for a τ-lepton decaying to leptons is [2]:

$$\begin{aligned} BR(\tau \to e + \bar{\nu}_e + \nu_\tau) &= 0.1737 \\ BR(\tau \to \mu + \bar{\nu}_\mu + \nu_\tau) &= 0.1784. \end{aligned} \tag{4.3}$$

When the values in 4.3 are averaged[2], the $BR(\tau\tau \to 2\,l + 4\,\nu)$ is:

$$BR(\tau\tau \to 2\,l + 4\,\nu) \approx (2 \cdot 0.176)^2 \approx 0.124 \tag{4.4}$$

The cross section of the remaining effective boson decaying to $\tau\tau \to 2\,l + 4\,\nu$ is then given by:

$$\sigma_{b\bar{b}\,\Phi_{eff}} \times BR\,(\Phi_{eff} \to \tau\tau \to 2\,l + 4\,\nu) = \sum_{\substack{degenerate \\ bosons\ \Phi}} \sigma_{b\bar{b}\,\Phi} \times BR(\Phi \to \tau\tau \to 2\,l + 4\,\nu) \tag{4.5}$$

[2]Average branching ratios for the τ decay to electrons and muons are valid because the systematic uncertainty on the cross section of the Higgs particle is dominant.

Figure 4.4 displays on its left the cross section of the effective boson decaying to $\tau\tau \rightarrow 2\ell + 4\nu$ as a function of m_A, the right plot shows the extrapolated cross section in the m_A-tan β plane. Because the cross section decreases very fast with increasing m_A, this

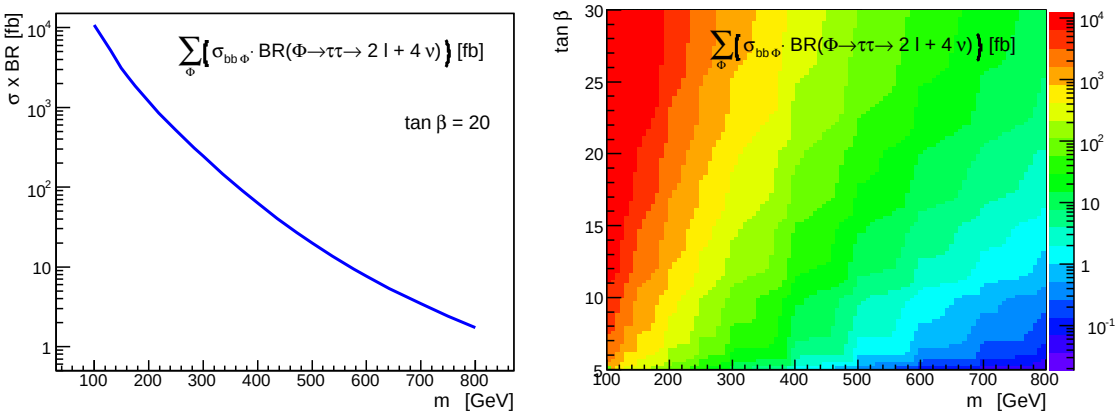

Figure 4.4: Cross section × BR of the effective boson as functions of m_A and tan β.

analysis is only sensitive to low and medium Higgs masses. The sensitivity increases for large values of tan β. In fact, considering Equation 4.1 and the flat distribution of $\sigma_{b\bar{b}h^0}$ vs. tan β in Fig. 4.2, one can conclude that the cross section of the effective boson also shows a quadratic dependency on tan β.
Taking into account these considerations and the LEP limit on the SM Higgs, the performed analysis will explore the discovery potential for a MSSM Higgs with 120 GeV $< m_A <$ 300 GeV and $5 <$ tan $\beta < 30$ using only one effective boson. The described mass degeneracy has not been studied in detail for every point in the m_A-tan β-plane. Especially for low values of tan β the mass difference between the Higgs bosons increases. But further studies show that the reconstructed Higgs width is very large compared to the mass difference (section 5.3). Therefore, the usage of three separate signals for each point in the m_A-tan β plane would complicate the analysis unnecessarily, especially because it is not a goal of this analysis trying to separate the Higgs bosons.

4.2.2 Generating the Signal Process

The datasets for the signal process $b\bar{b}\ h/A/H \rightarrow \tau\ \tau \rightarrow 2\ \ell + 4\ \nu$ have been generated using Sherpa [39] version 1.0.9. Sherpa is a relatively new event generator and uses the CKKW[3] matching [40; 41] for combining the ME and the parton shower. The key idea is to separate the phase space for parton emission into a hard region of jet production (accounted for by the ME) and the softer region of jet evolution (covered by the parton shower). Extra weights and vetoes are used to minimize the overall dependency on this phase space cut. Double counting of radiated jets is explicitly avoided. Graphs as displayed in Figure 2.5 can be matched correctly.

The b-associated Higgs production can be obtained from Sherpa using the following inputs (more information on the input files **.dat* is given in [42]):

[3]CKKW- Catani, Krauss, Kuhn, Webber.

- Yukawa coupling only to the b-quark switched on (YUKAWA_B=4.5 in *Model.dat*) This assures that the Higgs is produced in association with b-quarks. All other Yukawa couplings to quarks are switched off.

- SM Higgs h particle switched on *(Particles.dat)*
  As described before only one boson with the mass m_A is generated. The decay width is changed to the value of Γ_A.

- Generated production and decay processes *(Processes.dat)*:

$$\begin{aligned} Jet + Jet &\rightarrow h \\ Jet + Jet &\rightarrow h + Jet \\ Jet + Jet &\rightarrow h + Jet + Jet \\ h &\rightarrow \tau^+ + \tau^- \end{aligned}$$

  The processes are of EW order 2 and strong order 0, 1 and 2. Jet stands for a particle container including quarks and gluons. Some Feynman graphs included in Sherpa are displayed in Appendix B. Spin correlations between the mother particle (h) and its decay particles are also included in Sherpa.

- τ decay
  The decay of the τ-leptons is also handled by Sherpa. Since in this analysis only leptonically decaying τ's are considered, all BR for hadronic τ decays are set to zero.

The generated datasets are listed in Table 4.2. All the samples were generated using Sherpa Version 1.0.9 and simulated by ATLFast of the Athena[4] release Version 11.0.5. The number of events N is related to the integrated luminosity L as follows:

m_A [GeV]	$\sigma \times BR$[fb]	Γ_A [GeV]	generated events	events needed for 30fb^{-1}
120	6309	0.994	250 k	189.3 K
160	2497	1.263	187.5 k	74.9 K
200	1136	1.665	125 k	34.1 K
250	498	2.157	125 k	14.9 K
300	118.26	2.874	125 k	3.7 K

Table 4.2: Data samples for the signal process.

$$L = \frac{N}{\sigma \times BR} \, . \tag{4.6}$$

This analysis is optimized for an integrated luminosity of 30 fb^{-1} which is expected after three years of LHC running at initial luminosity.

[4]Athena is the ATLAS software framework.

4.3 Background Processes

For a realistic study besides the signal also all important background processes must be considered. Processes with a similar final state as the signal are possible backgrounds. Processes with at least one b-tag[5], two leptons and missing transverse energy are relevant, especially if the order of magnitude of the cross section is at least comparable to the signal cross section.
Cross sections are one of the most important inputs into this analysis, because they are directly related to the normalization (Equation 4.6). MC generators mostly only state LO cross sections, whereas NLO cross section calculations are known and available by external programs.

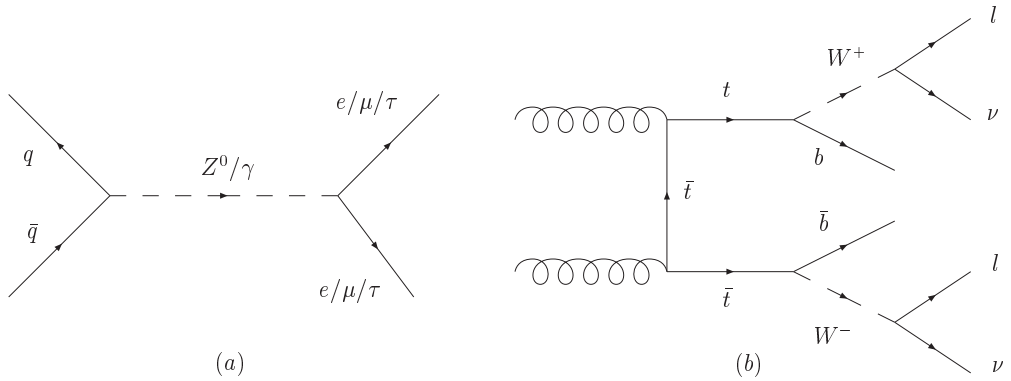

Figure 4.5: Possible Feynman graphs for the main backgrounds.

The following processes have been studied (the datasets are listed in Table 4.3):

- Z + jets
  Z^0 production has by far the largest cross section of all background processes. The Drell Yan process $q\bar{q} \to Z^0/\gamma \to \ell\,\ell$ is displayed in Figure 4.5a. The Z^0 decays to a pair of leptons (BR in Equation 2.4). The decay to $\tau\tau \to 2\ell + 4\nu$ then has the same topology as the signal. If the Higgs mass is small (around 100 GeV), Z^0 decays to τ-leptons will be an irreducible background process.
  Z + jets samples have been produced using Sherpa 1.0.8 and they have been processed using ATLFast 11.0.5. The enormous computation effort was handled at GridKa.
  On all Z + jet samples a cut on the invariant lepton-lepton mass m_{ll} is applied at generator level:
  $$60 \text{ GeV} < m_{\ell\ell} < 14 \text{ TeV}. \tag{4.7}$$
  This is done to reject events where a photon is produced instead of a Z^0 boson which would lead to a very large cross section for small invariant lepton-lepton masses. The Z^0 cross section is a very important input. It was calculated in NLO by the program MCFM [43] taking into account the mass cut to $\sigma_Z = (1763.5 \pm 1.2)$ pb.

[5]B-tagging is important to this analysis, it labels a jet as a jet originating from a b-quark. Light jets (originating from u-,d- or s-quarks) and c-jets can be mis-tagged as b-jets.

- $t\bar{t}$
  LHC will be a top factory. One top pair is expected to be produced every second [44]. Top pairs decay (almost to 100%) to W bosons and b-quarks, the W bosons decay further to leptons and neutrinos (Figure 4.5b).
  $t\bar{t}$ has been generated using MC@NLO [45; 46] and processed with ATLFast 11.0.5. The underlying event was generated by Jimmy [47].
  The $t\bar{t}$ cross section is not known precisely because of sizeable contributions from the uncertainties on the top mass and from scale variations. MC@NLO states the value as $\sigma_{t\bar{t}} = 776$ pb. This is in good agreement with a NLO calculation with the result $\sigma_{t\bar{t}} = (794 \pm 32)$ pb [48]. The used cross section value is taken from MC@NLO. Then a two-lepton filters is applied to get processes like $t\bar{t} \rightarrow W^+W^- + b\bar{b} \rightarrow 2\ell + 2\nu + b\bar{b}$.

- SUSY background
  Background coming from the production of SUSY particles must also be considered in this non-SM study. For two points in the m_A-$\tan\beta$ plane SUSY samples [49; 50] have been generated to test their general relevance to this analysis. The sample SUSY-120-20 was generated for $m_A = 120$ GeV and $\tan\beta$=20, SUSY-200-20 for $m_A = 200$ GeV and $\tan\beta$=20.
  For the inclusive SUSY samples the event generator Herwig [51; 52] has been used. The simulation tool was ATLFast 11.0.5. The cross sections used are calculations by the program Prospino [53]: $\sigma_{SUSY-120-20} = (6.246 \pm 0.049)$ pb and $\sigma_{SUSY-200-20} = (6.234 \pm 0.049)$ pb. These values were cross checked with Herwig which calculated $\sigma_{SUSY} = 6.506$ pb.

- W W + jets (EW)
  W-pairs decay to leptons (e, μ and τ, τ decay into leptons and hadrons) and neutrinos and may also be relevant. But the cross section for this process ($\sigma_{WW} \times BR = (95.9 \pm 1.1)$ fb) is far below all other background cross sections.
  WW was generated with Madgraph [54] and Pythia [55] and simulated with ATLFast 10.0.1.

Process	$\sigma \times BR[pb]$	generated events	events needed for 30fb^{-1}
$t\bar{t}$	776	15.7 M	5.5 M
$Z \rightarrow \tau\tau$	218.7	20 M	6.5 M
$Z \rightarrow \mu\mu$	1763.5	52.9 M	52.9 M
$Z \rightarrow e\,e$	1763.5	52.9 M	52.9 M
SUSY-120-20	6.25	1 M	187 K
SUSY-200-20	6.23	0.6 M	187 K
WW+jets	0.095	148 K	2850

Table 4.3: Data samples for the background processes.

Chapter 5

Reconstruction of the Higgs Particle

5.1 Collinear Approximation

Although there are four neutrinos in the final state, a reconstruction of the invariant Higgs mass is possible using the collinear approximation. Neutrinos cannot be detected directly by ATLAS because they are not electrically charged and have a negligible probability of interaction. But they are 'visible' as missing transverse momentum in the detector (Equation 3.5). A scheme of the Higgs decay is displayed in Figure 5.1.

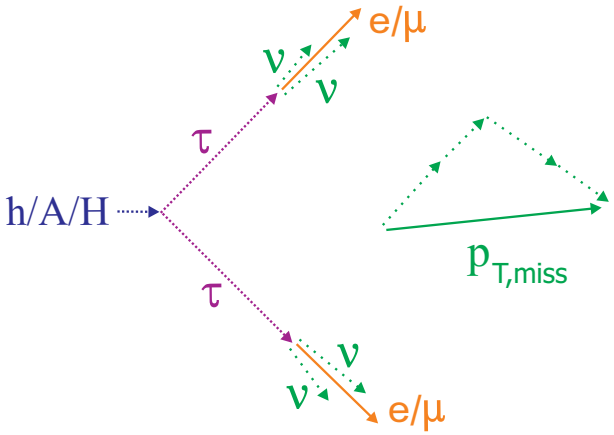

Figure 5.1: Scheme of the Higgs decay. The τ decay products are emitted in the direction of the τ's. The sum of the p_T of the four neutrinos form the $p_{T,miss}$ vector.

The collinear approximation is used to reconstruct the invariant mass of the two τ-leptons, in order to obtain the Higgs mass. There are four leptonic sub-decay channels of the two τ's:

$$\begin{aligned}
\tau^+\,\tau^- &\rightarrow e^+ + e^- + \bar{\nu}_e + \nu_e + \nu_\tau + \bar{\nu}_\tau \quad (\approx 25\%)\\
\tau^+\,\tau^- &\rightarrow \mu^+ + \mu^- + \bar{\nu}_\mu + \nu_\mu + \nu_\tau + \bar{\nu}_\tau \quad (\approx 25\%)\\
\tau^+\,\tau^- &\rightarrow e^+ + \mu^- + \nu_e + \bar{\nu}_\mu + \nu_\tau + \bar{\nu}_\tau \quad (\approx 25\%)\\
\tau^+\,\tau^- &\rightarrow e^- + \mu^+ + \bar{\nu}_e + \nu_\mu + \nu_\tau + \bar{\nu}_\tau \quad (\approx 25\%).
\end{aligned}$$

In the following, *lepton* (l) labels electron or muon coming from the τ decay.
The collinear approximation is based on the following assumptions:

- Heavy Higgs boson
  If the Higgs boson mass is large compared to the τ mass, the τ-leptons experience a strong Lorentz boost, i.e. they have a large energy compared to their rest mass. In the subsequent decay of the τ into a lepton and two neutrinos, the daughter particles are emitted in the direction of flight of the τ. So the neutrino direction is approximately the same as the lepton direction (they are collinear).
  In Figure 5.2 the angles on generator level between e and τ and between e and ν_e are displayed (Higgs mass 120 GeV data sample) as an example. Both distributions peak at angles around zero.

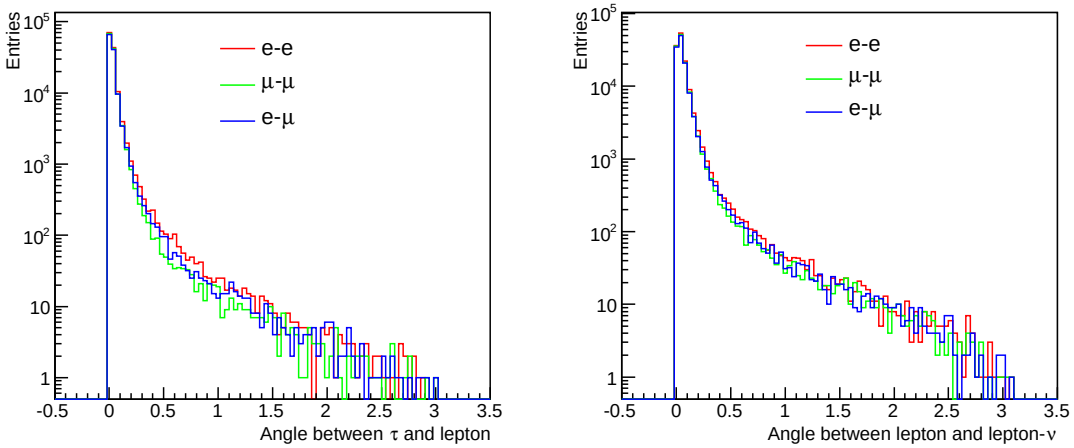

Figure 5.2: Angle between τ and lepton (left) and lepton and ν_ℓ (right). Values around zero correspond to the collinearity of the τ's and their daughter particles.

- Missing transverse momentum only comes from neutrinos

$$p_{T,miss} = \sum_{i=1..4} p_{T,\nu_i}. \tag{5.1}$$

  Other effects such as particles outside the η acceptance of the detector or shower fluctuations will lead to a missing momentum signature not related to the four neutrinos of the signal process. This leads to a deterioration of the Higgs mass resolution.
  In Figure 5.3 the p_T of the neutrinos $p_{T,\nu}$ (truth level) and $p_{T,miss}$ (simulation level) are displayed. Although both variables follow the same distribution (left), they show differences of several GeV (right) on an event-by-event basis. The plots are made for the 120 GeV Higgs mass dataset.

- The Higgs boson has a non-zero transverse momentum
  The collinear approximation only gives numerically stable results if the Higgs boson has a $p_T > 0$. Otherwise the leptons would be emitted back-to-back ($\Delta\Phi_{\ell\ell} = \pi$). In that case the $p_{T,miss}$vector would be collinear to the p_T of the leptons and the τ momentum could not be reconstructed as will be shown below. The mass resolution already deteriorates for angles close to π.

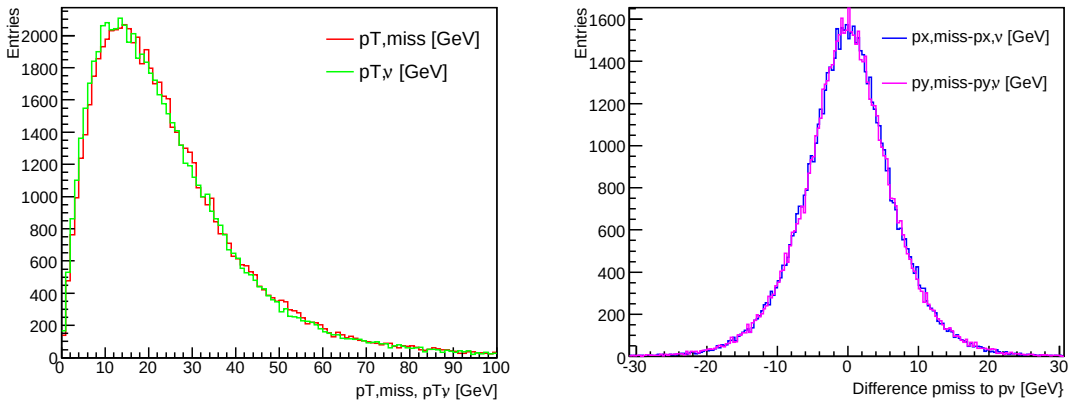

Figure 5.3: $p_{T,miss}$ distribution (left) and difference of $p_{T,miss}$ and $p_{T,\nu}$ broken down to x- and y components (right). Both plots correspond to a 120 GeV Higgs mass sample.

The algorithm uses p_T conservation:

$$\vec{p}_{T,\tau 1} + \vec{p}_{T,\tau 2} = \vec{p}_{T,\ell 1} + \vec{p}_{T,\ell 2} + \vec{p}_{T,miss}. \tag{5.2}$$

The τ-momenta ($i = 1, 2$) are substituted as follows:

$$\vec{p}_{T,\tau_i} = \frac{\vec{p}_{T,l_i}}{x_i}. \tag{5.3}$$

x gives the fraction of the τ momentum carried by the daughter lepton. x takes values between 0 and 1. This is valid because of the same flight direction. x_1 and x_2 can be calculated using 5.2 and 5.3 in the notation of the two components $\vec{p}_T = \begin{pmatrix} p_x \\ p_y \end{pmatrix}$:

$$\begin{aligned} x_1 &= \frac{p_{x,l_1} \cdot p_{y,l_2} - p_{y,l_1} \cdot p_{x,l_2}}{p_{y,l_2} \cdot p_{x,miss} - p_{x,l_2} \cdot p_{y,miss} + p_{x,l_1} \cdot p_{y,l_2} - p_{y,l_1} \cdot p_{x,l_2}} \\ x_2 &= \frac{p_{x,l_1} \cdot p_{y,l_2} - p_{y,l_1} \cdot p_{x,l_2}}{p_{x,l_1} \cdot p_{y,miss} - p_{y,l_1} \cdot p_{x,miss} + p_{x,l_1} \cdot p_{y,l_2} - p_{y,l_1} \cdot p_{x,l_2}}. \end{aligned} \tag{5.4}$$

The invariant $\tau - \tau$ mass is given as follows:

$$m^2_{\tau\tau} = (p_{\tau_1} + p_{\tau_2})^2. \tag{5.5}$$

Here $p_{\tau_i} = (E_{\tau_i}, \vec{p}_{\tau_i})$ labels the four momentum. Using $p^2_{\tau_i} = m^2_{\tau_i}$ one obtains:

$$m^2_{\tau\tau} = 2 \cdot \left(m^2_\tau + p_{\tau_1} \cdot p_{\tau_2}\right). \tag{5.6}$$

Neglecting the τ mass and using 5.3 leads to:

$$m^2_{\tau\tau} = 2 \cdot \left(\frac{p_{l_1} \cdot p_{l_2}}{x_1 \cdot x_2}\right). \tag{5.7}$$

Using the invariant lepton-lepton mass $m^2_{\ell\ell} \approx 2 \cdot p_{\ell_1} \cdot p_{\ell_2}$ and neglecting the electron and μ masses, leads to:

$$m_{\tau\tau} = \frac{m_{\ell\ell}}{\sqrt{x_1 \cdot x_2}}. \tag{5.8}$$

Equation 5.8 gives the approximate Higgs mass. The neglect of the lepton masses is valid because they are small compared to the Higgs masses of $m_A \geq 120$ GeV considered here.

5.2 Selection of Events

5.2.1 Trigger

The trigger is supposed to reduce the number of events for permanent storage. The ATLAS trigger system has been described in chapter 3. The ATLAS trigger conditions applying here are (in brackets are the official ATLAS nomenclatures [56]):

- two electrons with $p_T > 15$ GeV (2e15)
- two muons with $p_T > 10$ GeV (2μ10)
- one electron with $p_T > 25$ GeV (1e25)
- one muon with $p_T > 20$ GeV (1μ20)

In this analysis these trigger conditions are adapted on ATLFast level by using simple cuts.

5.2.2 Preselection Cuts

In order to get meaningful results from the collinear approximation, the following set of precuts was devised. This selection is used as a first method to get a look onto the reconstructed mass of signal and backgrounds.

- Trigger
  The event is selected, if any of the four trigger conditions is satisfied.
- Selection of the leptons (electrons or muons)
  It is decided which leptons are used for the reconstruction algorithm. The leptons need to have opposite charges. First, objects that were identified by ATLFast as isolated electrons or isolated muons get sorted by decreasing p_T. Depending on which trigger conditions were satisfied, it is then decided which of the sub decay channels applies for the event. Exclusively one channel ($e-e$ or $\mu-\mu$ or $e-\mu$) is selected.
  - Only 2e20 set on
    The pair of electron and positron with the highest p_T is selected and allocated to the $e-e$ channel.
  - Only 2μ10 set on
    The pair of muon and antimuon with the highest p_T is selected and allocated to the $\mu-\mu$ channel.
  - 2e20 and 2μ10 set on
    In the very rare case where the requirements for both di-lepton triggers are fulfilled, one category is chosen randomly.
  - 1e25 and 1μ15 set on
    The highest p_T pair of electron (positron) and antimuon (muon) is selected and allocated to the $e-\mu$ channel.

– Only 1e25 set on
In this case the number of electrons and muons is of importance. If there are no muons and more than one electron in the event, the highest p_T pair of electron and positron is selected for the $e-e$ channel. If there are muons and electrons in the event, an oppositely charged lepton pair is allocated to the mixed channel.

– Only 1μ15 set on
As in the previous case, depending on the number of electrons and muons, a pair is selected for either the $\mu-\mu$ or the mixed channel.

If no channel could be chosen because no lepton pair with opposite charges could be found, the event is rejected.
Figure 5.4 shows the p_T of the selected leptons for each channel and for two different Higgs mass hypotheses. The peaks in the p_T spectra match with the applied trigger cuts.

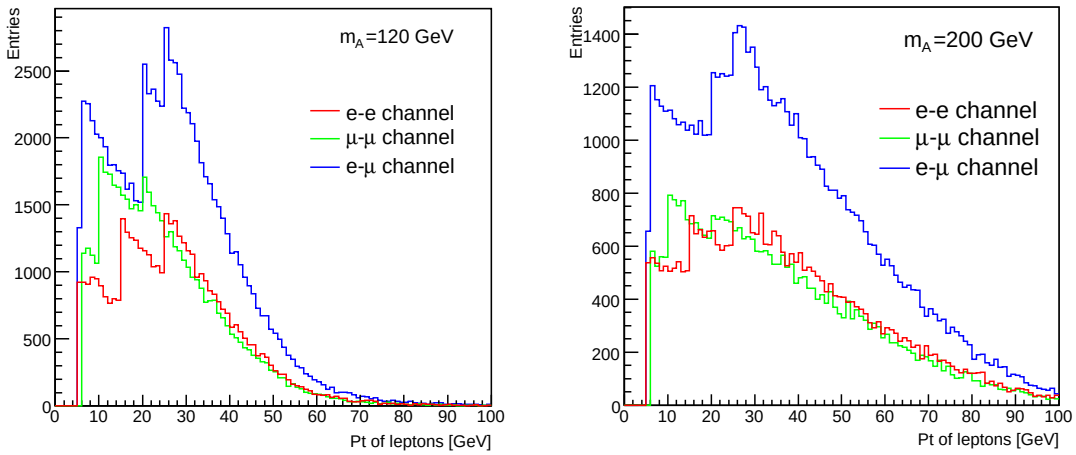

Figure 5.4: p_T spectrum of the selected leptons for two mass hypotheses after trigger cuts.

- At least one b-tag
Since the Higgs boson is produced in associated production with b-quarks, at least one b-tag is required in order to suppress the background from light jets.
In ATLFast a statistical b-tagging algorithm is implemented, based on the full simulation tagging probabilities. Furthermore, to calibrate the energy of the b-tagged jets, the routine ATLFast-B is included. The energy calibration is needed to get correct values for example for the invariant di-jet masses. The lowest p_T of a b-jet in ATLFast is 15 GeV, after the calibration with ATLFast-B this value is at around 17 GeV. Figure 5.5 shows the p_T of the leading b-jet broken down to the various truth jet types of the b-tagged jet. The plots were made for the 300 GeV Higgs sample. A small contamination from light and c-jets is obvious. The little discontinuities on the p_T distribution at 30 GeV and 50 GeV are due to ATLFast-B, applying a non-continuous function onto the non-calibrated jet p_T distribution [57].
In Figure 5.6 the η distributions for the selected leptons and the leading b-jet are displayed. In ATLFast all objects outside $-2.5 < \eta < 2.5$ are rejected. In contrast

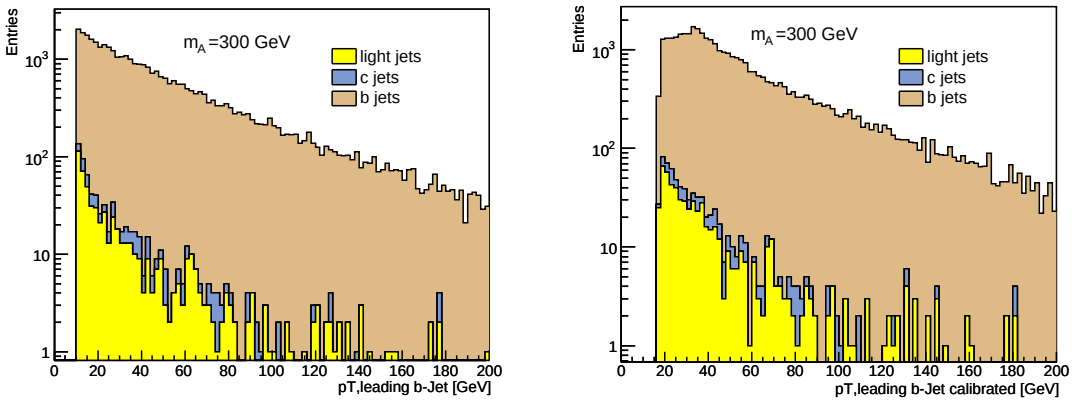

Figure 5.5: p_T of leading b-jet broken down to truth jet types non-calibrated (left) and calibrated (right) for a 300 GeV Higgs mass sample.

to Vector-Boson-Fusion (VBF), the η of the tagged b-jet cannot be used for a preselection of the signal signature, because the η_{b-jet} distribution is almost flat. The Φ distribution is displayed in Figure 5.7 has to be flat, because of the definition of Φ (Equation 3.1).

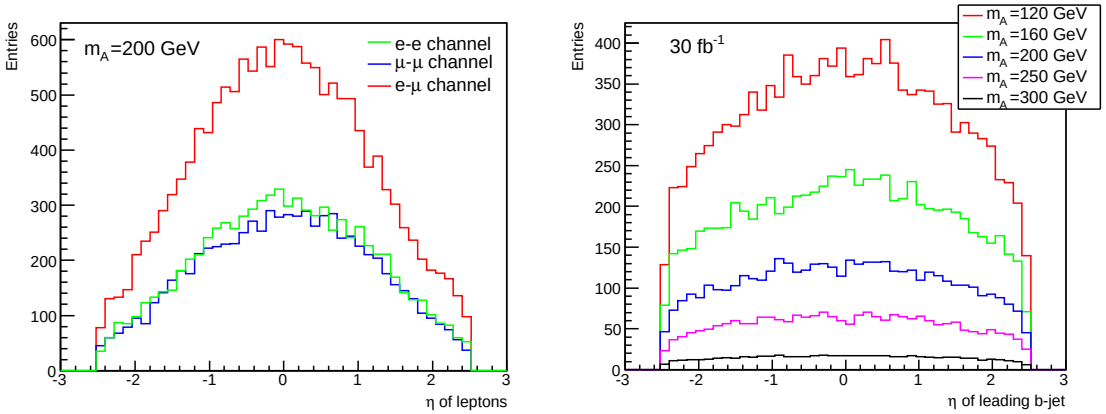

Figure 5.6: η of the selected leptons (left) and the leading b-jet (right).

- Cut on x_i
  Due to the definition of x in Equation 5.3, a cut on the physical region is applied:

$$0 < x_i < 1 \quad i = 1, 2. \tag{5.9}$$

In Figure 5.8 on the left side x_1 and x_2 are displayed. The events outside the allowed range are due to the $p_{T,miss}$ smearing. On the right side a plot of x_1 versus x_2 is shown.
To explain the different values of x_1 and x_2 it must be emphasized again, that the leptons are p_T sorted and the highest p_T pair is used for the reconstruction. Lepton number 1 in Equation 5.4 corresponds to the highest p_T lepton of this pair, lepton 2 has a lower p_T. As a consequence, x_1 peaks at higher values than x_2. If the

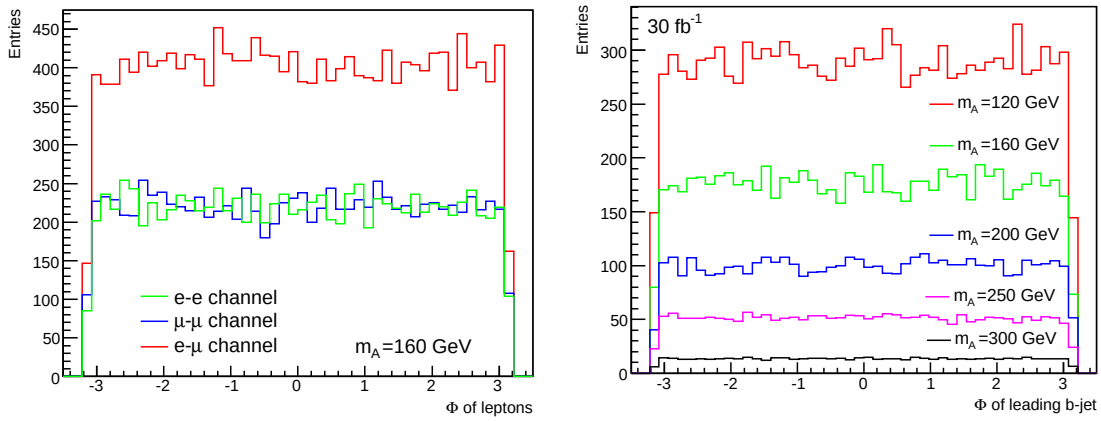

Figure 5.7: Φ of the selected leptons (left) and the leading b-jet (right).

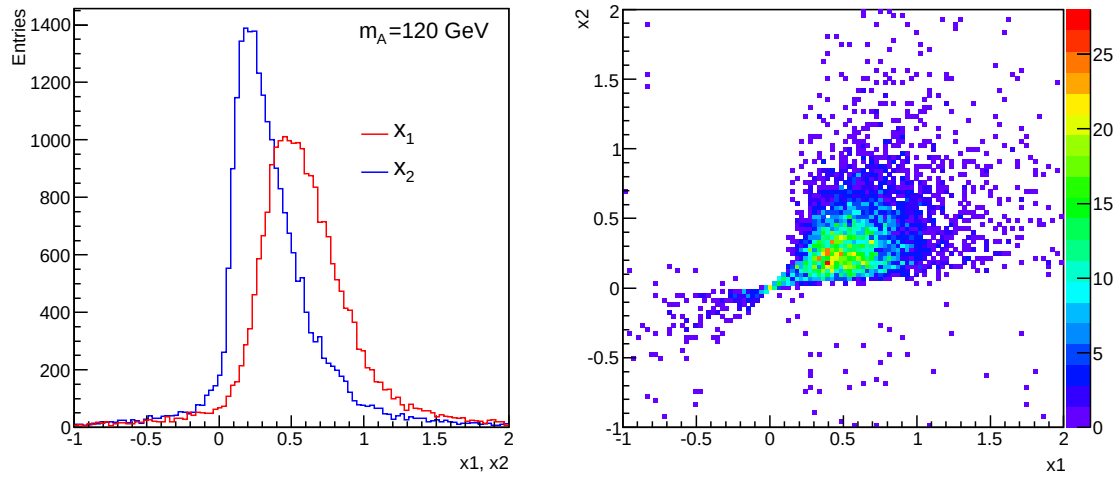

Figure 5.8: x_1 and x_2 for the 120 GeV Higgs signal.

leptons would be chosen randomly, the factors x_1 and x_2 would both peak at the same values. The product of $x_1 \cdot x_2$ (which is essential for the calculation of $m_{\tau\tau}$) however is not affected by the p_T sorting.

- Cut on $\Delta\Phi_{\ell\ell}$
  Because the collinear approximation does not work if the leptons are back-to-back, a cut on $\Delta\Phi_{\ell\ell}$ has to be applied. In Figure 5.9 $\Delta\Phi_{\ell\ell}$ for all five Higgs hypotheses is displayed (before cutting on the angle). The right plot shows that there is a strong correlation between $\Delta\Phi_{\ell\ell}$ and the p_T of the Higgs. Most leptons are emitted nearly back-to-back, which is due to the small $p_{T,Higgs}$. A comparison with a VBF analysis $H \rightarrow \tau\tau \rightarrow 2l + 4\nu$ [58] shows that the mean value of $p_{T,Higgs}$ produced in VBF is larger than when produced in association with b-quarks. The reference states a mean $p_{T,Higgs}$ for m_H=120 GeV of 87.97 GeV, whereas the corresponding value for the mean $p_{T,Higgs}$ in this analysis is only 56.16 GeV.
  A cut an $\Delta\Phi_{\ell\ell}$ has affects on both signal efficiency and mass resolution, as displayed in Figure 5.10.

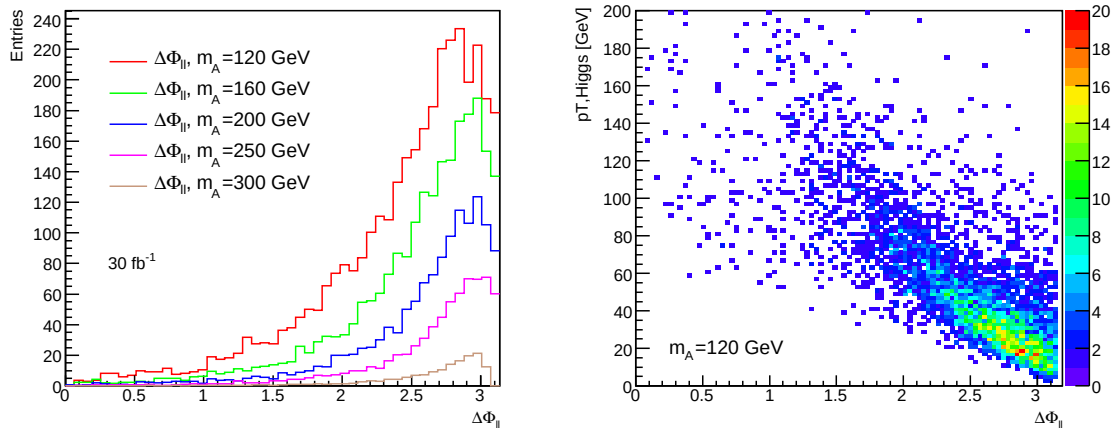

Figure 5.9: $\Delta\Phi_{\ell\ell}$ (left) and $\Delta\Phi_{\ell\ell}$ vs. Higgs p_T for m_A=120 GeV (right). The right plots shows that there is a correlation between $\Delta\Phi_{\ell\ell}$ and the p_T of the Higgs particle.

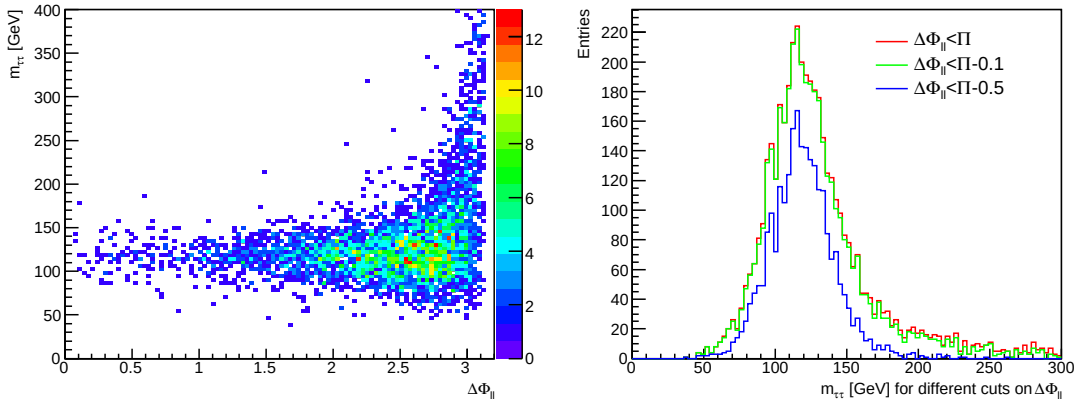

Figure 5.10: Dependency of the reconstructed Higgs mass on $\Delta\Phi_{\ell\ell}$. In the left plot $m_{\tau\tau}$ vs. $\Delta\Phi_{\ell\ell}$ is shown, in the right plot the Higgs mass is reconstructed for different cuts on $\Delta\Phi_{\ell\ell}$. Both plots were made for the 120 GeV Higgs mass sample.

It is obvious that a hard cut on $\Delta\Phi_{\ell\ell}$ decreases the signal events passing those precuts but also cuts away the high-energy tail in $m_{\tau\tau}$ and this way improves the mass resolution. Figure 5.11 shows that for m_A=250 GeV the signal goes down by almost 65 % when cutting on $\Delta\Phi < \pi - 0.5$. Mass dependent precuts would complicate the reconstruction unnecessarily, and so the following (Higgs mass independent) cut is applied:

$$\Delta\Phi_{\ell\ell} < \pi - 0.1 \approx 174.3^\circ. \tag{5.10}$$

This only affects the mass resolution slightly but has consequences for the product $x_1 \cdot x_2$. In Figure 5.12 on the left $\Delta\Phi_{\ell\ell}$ has been plotted versus $x_1 \cdot x_2$, showing a peak at $\Delta\Phi_{\ell\ell} \approx \pi$ and $x_1 \cdot x_2 \approx 0$. This peak would lead to unphysical infinite values of $m_{\tau\tau}$ according to Equation 5.8. The right plot shows that this zero peak is cut away when applying the cut on $\Delta\Phi_{\ell\ell}$.

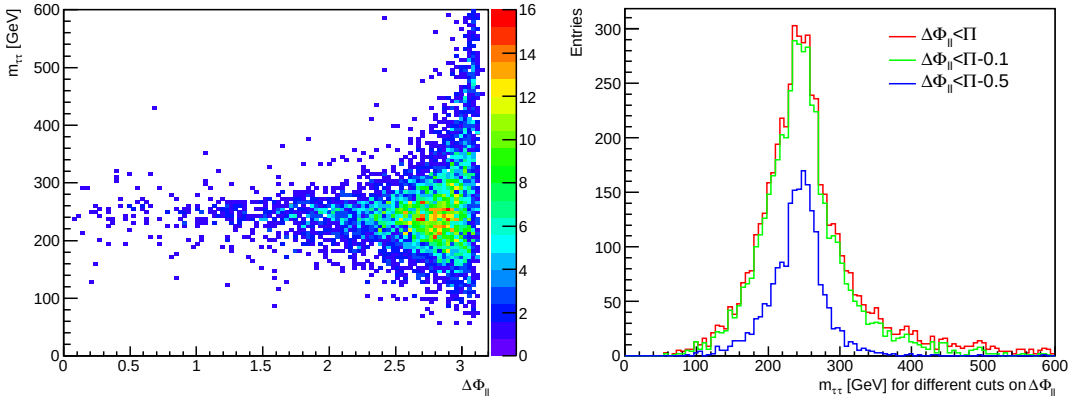

Figure 5.11: Dependency of the reconstructed Higgs mass on $\Delta\Phi_{\ell\ell}$. In the left plot $m_{\tau\tau}$ vs. $\Delta\Phi_{\ell\ell}$ is shown, in the right plot the Higgs mass is reconstructed for different cuts on $\Delta\Phi_{\ell\ell}$. Both plots are made for the 250 GeV Higgs mass sample.

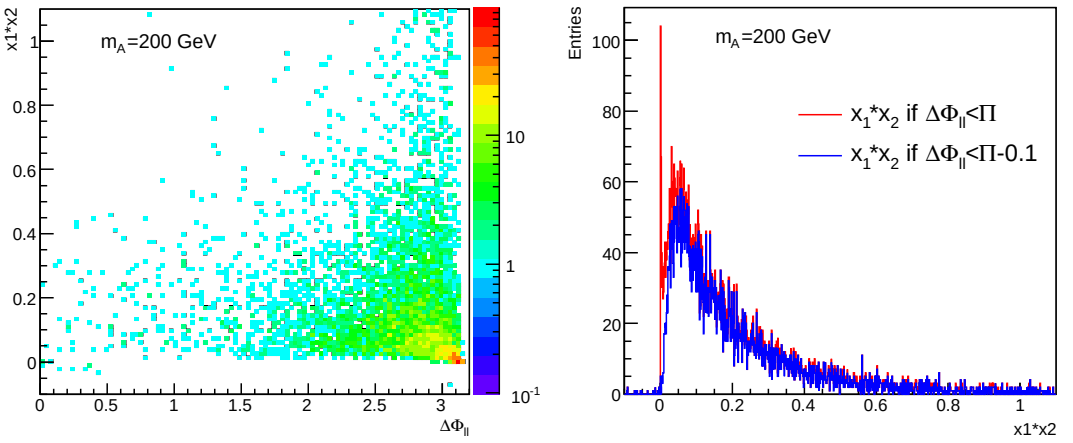

Figure 5.12: $x_1 \cdot x_2$ vs. $\Delta\Phi_{\ell\ell}$ (left) and $x_1 \cdot x_2$ for different cuts on $\Delta\Phi_{\ell\ell}$. The red line in the right figure demonstrates the collapse of the collinear approximation when no cut on $\Delta\Phi_{\ell\ell}$ is applied. Both plots are made from the 200 GeV Higgs mass sample.

5.3 Signal Reconstruction after the Preselection

In the following, all five Higgs mass hypotheses are being reconstructed using the described precuts. The events from all three sub-channels are being stacked.
Figure 5.13 shows the p_T distribution for the Higgs (left) and the leading b-jet for all signal samples (right), normalized to 30 fb^{-1} and $\tan\beta$=20. The mass dependent mean values are also given.
Figure 5.14 shows the invariant mass of the lepton pairs (left) and the invariant mass of the τ-leptons after collinear approximation for all mass hypotheses, normalized to 30 fb^{-1}.

It is obvious, that the mass resolutions worsen for larger values of m_A. So a discovery of a heavy Higgs is complicated not only due to the much lower cross section but also due to the larger reconstructed width.

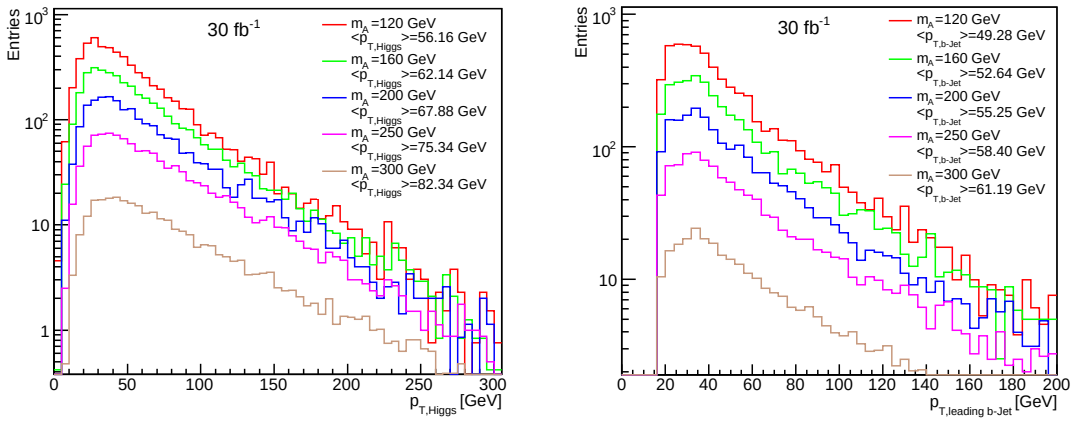

Figure 5.13: p_T of the Higgs (left) and the leading b-jet (right).

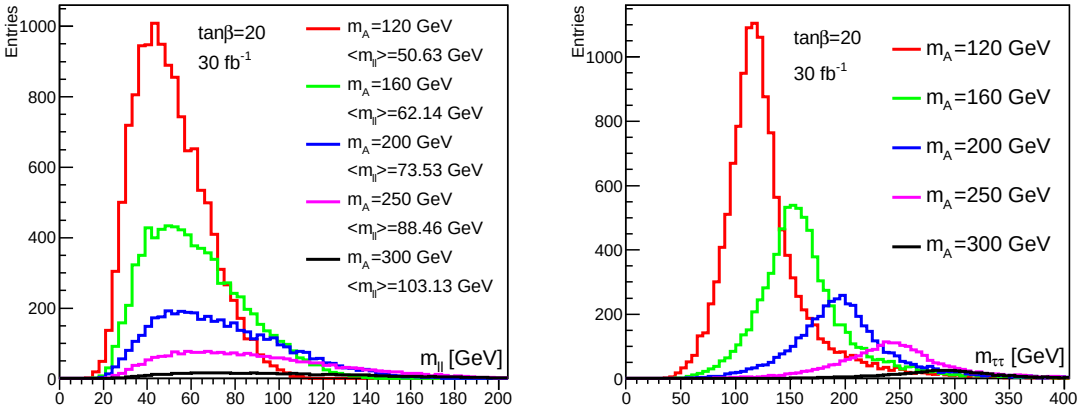

Figure 5.14: Invariant $m_{\ell\ell}$ (left) and invariant $m_{\tau\tau}$ (right).

A Gaussian is fitted to obtain the resolution of $m_{\tau\tau}$. The shape of $m_{\tau\tau}$ is not a single Gaussian, only the central part around the value of m_A can be fitted with a Gaussian (Figure 5.16). The range was Higgs mass dependent chosen. As a consequence, the width of the distribution depends on the fit range. Here the range $m_A - 60\ GeV < m_A < m_A + 40\ GeV$ is used. Figure 5.15 shows the reconstructed mass for a 160 GeV Higgs, in the right plot a comparison between the mass on ATLFast level and on truth level is shown. The mass distribution on truth level is obtained by applying the algorithm for the collinear approximation to the true leptons and neutrinos. The deterioration of the mass resolution between truth and fast simulation level is due to $p_{T,miss}$ smearing.
The fitted Higgs mass is a few GeV lower than the nominal m_A. This was noticed for all five Higgs signals. Furthermore, this left-shift of the mass gets larger for higher masses[1]. In Figure 5.16 all five Higgs mass hypotheses are fitted with a Gaussian for a comparison. In Figure 5.17 the true Higgs mass and the reconstructed mass are displayed on the left, and the reconstructed width versus the generated Higgs mass is shown on the right. The values for the plots are taken from Figure 5.16.

[1] Another study of $h/A/H \rightarrow \tau\tau$ does also show this shift in the invariant mass [59].

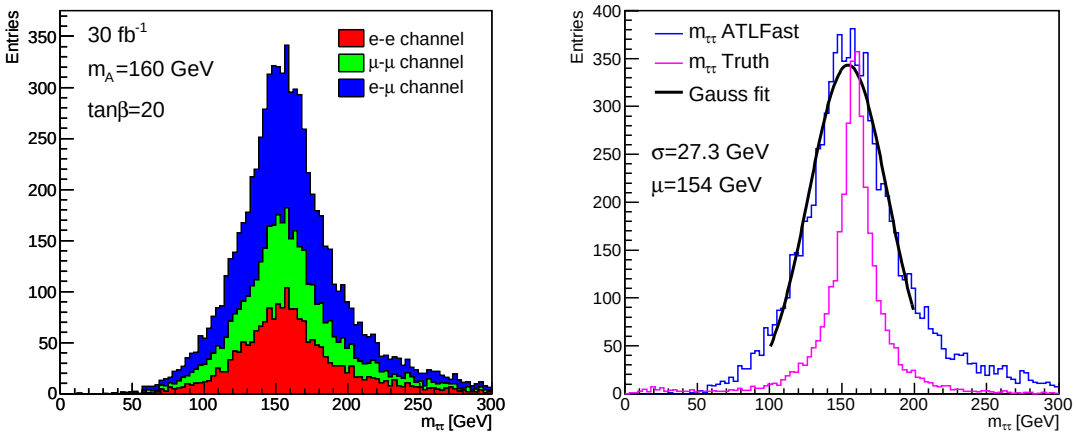

Figure 5.15: Stacked $m_{\tau\tau}$ for m_A=160 GeV (left) and mass resolution after collinear approximation on ATLFast and truth level (right).

In Table 5.1 the absolute number of events remaining after each preselection step for the five Higgs signal masses are listed. The numbers are normalized to an integrated luminosity of 30 fb^{-1} and assuming tan β=20. The value of the signal efficiency ϵ is given by:

$$\epsilon = \frac{\text{number of events after last preselection step}}{\text{number of events after trigger}} \cdot 100\,\% \tag{5.11}$$

It is evident that the efficiency increases for higher Higgs masses. This is mainly due to larger mean values for the p_T of the leptons and the leading b-jet, leading to slightly higher efficiencies for events passing the trigger and the b-tag, respectively.

m_A [GeV]	Trigger	e/μ Selection	$\geq$1 b-Tag	0<x_i<1	$\Delta\Phi_{\ell\ell}$<π-0.1	ϵ [%]
120	95 275	66 856	18 622	14 106	13 028	13.7
160	50 309	36 754	10 977	8 772	7 934	15.8
200	25 718	19 353	6 102	4 966	4 420	17.2
250	12 433	9 620	3 234	2 681	2 313	18.6
300	3 146	2 491	865	722	610	19.4

Table 5.1: Absolute number of signal events for $L = 30$ fb^{-1} and tan β=20.

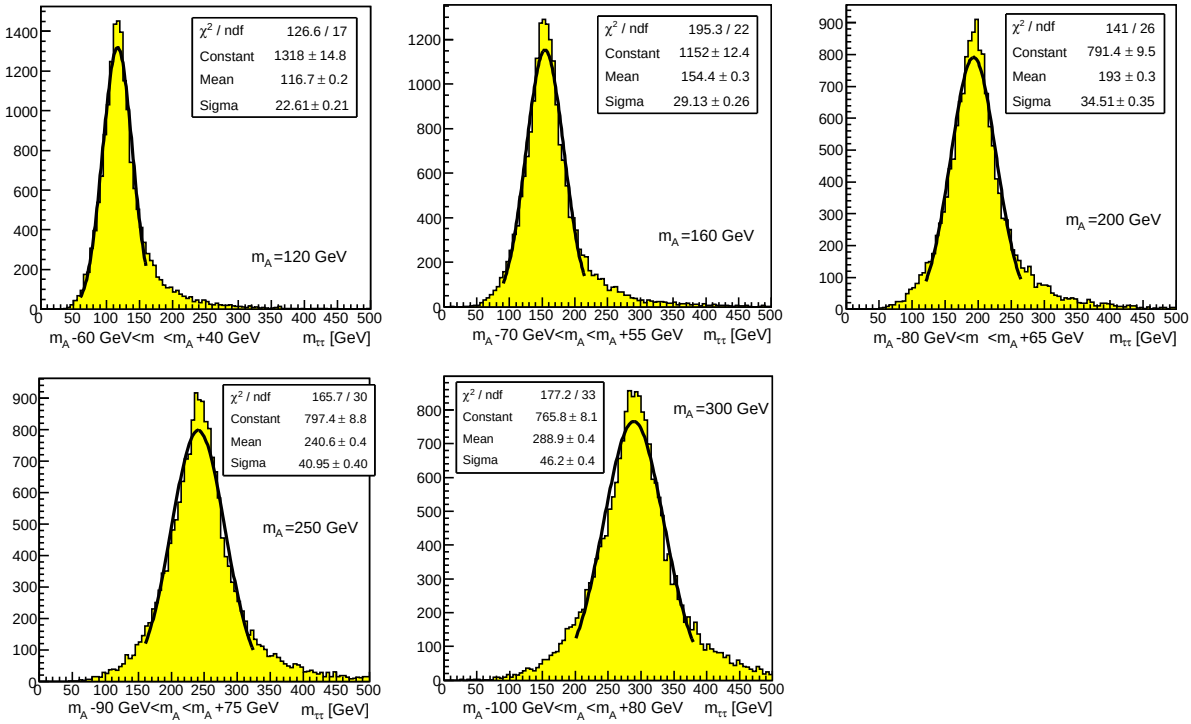

Figure 5.16: Invariant $\tau\tau$ mass for five Higgs mass hypotheses fitted with a single Gaussian in a Higgs mass dependent range. The asymmetric range was chosen to exclude the asymmetric high mass tail from the Gaussian fit and also to take the shift to lower masses into account.

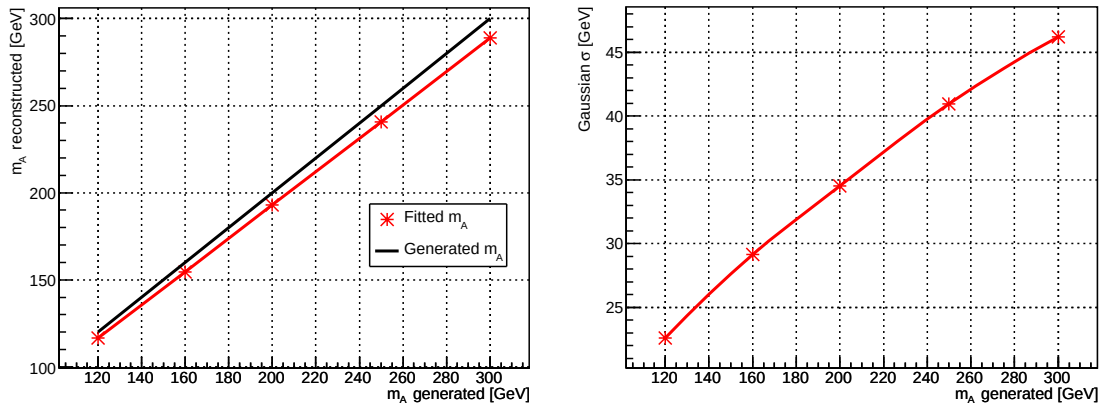

Figure 5.17: Invariant $\tau\tau$ mass (left) and Gaussian σ (right); both as functions of m_A. The shift of $m_{\tau\tau}$ to lower masses intensifies for higher valus of m_A.

5.4 Background reconstruction after the Preselection

The algorithm described for the Higgs reconstruction is now applied to all background samples. The same preselection cuts are used.

5.4.1 Remarks on Z+jets

Because Z+jets is the most important background, some relevant quantities have been studied in addition.

- Cut on $m_{\ell\ell}$ on generator level (Equation 4.7)
  The cut applied on the invariant lepton-lepton mass is 60 GeV$<m_{\ell\ell}$. To test how many events with $m_{\ell\ell}$ below 60 GeV are cut away by this, an extra sample with $10\ GeV < m_{\ell\ell} < 14\ TeV$ was generated (Sherpa 1.0.8, 237 500 events). The Drell Yan mass spectrum is displayed in Figure 5.18 for both triggered and not triggered events. Not triggered event means that any pair of an electron and a positron has been used without asking for a minimal p_T. When requiring the trigger conditions the mass distribution for the events with $m_{\ell\ell} < 60 GeV$ is flat and negligible. The right plots shows the correlation between the p_T of the leptons and the invariant mass for events without asking for the trigger. Leptons coming from the exchange of virtual photons have p_T values far below the trigger threshold (values around 5 GeV). Leptons coming from the exchange of Z^0 bosons have mean p_T values around 40 GeV and get selected by the trigger.
  As a conclusion to this study it is justified to use the cut $m_{\ell\ell} > 60$ GeV on all Z+jets samples without having excluded relevant events.

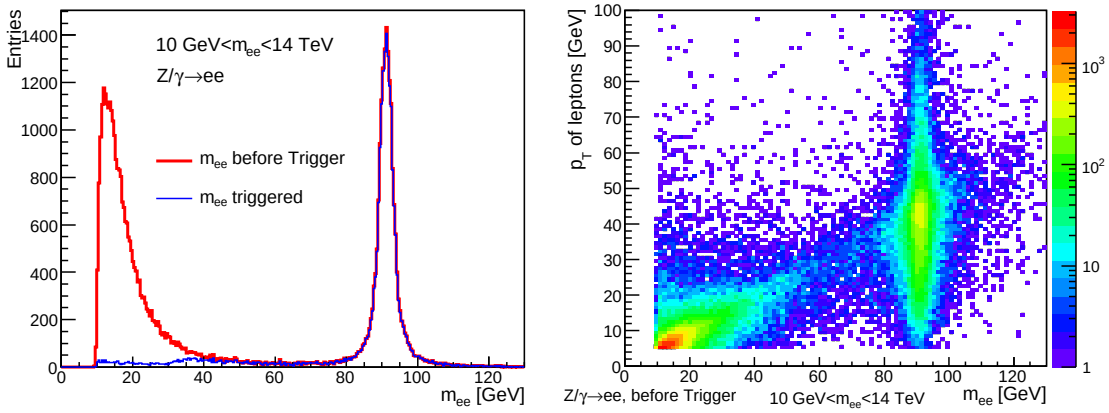

Figure 5.18: $m_{\ell\ell}$ (left) and lepton p_T vs. $m_{\ell\ell}$ for $Z/\gamma \rightarrow ee$ events (right).

- Mistagged b-jets
  In Figure 5.19 the p_T of the leading b-jet broken down to the truth jet types is displayed. As in Figure 5.5 for the signal, bumps in the distribution at 30 GeV and 50 GeV are due to the energy calibration by ATLFast-B. The large number of light jets comes from the underlying event.

- Collapse of the collinear approximation
  In Z+jets the same peak at $\Delta\Phi_{\ell\ell} = \pi$ and $x_1 \cdot x_2 = 0$ occurs as for the signal, leading

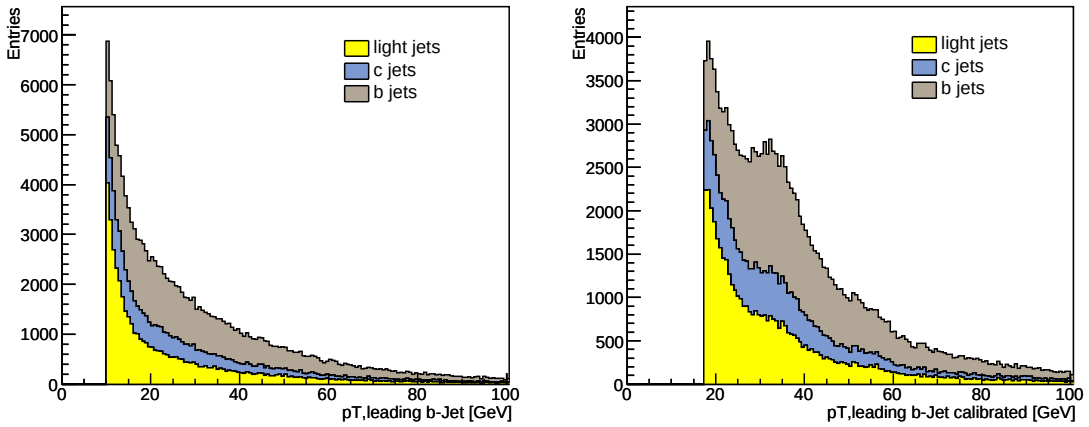

Figure 5.19: p_T of leading b-jet un-calibrated (left) and calibrated (right) for Z+jets.

to an infinite $m_{\tau\tau}$ (collapse of the collinear approximation). Figure 5.20 shows on the left side $\Delta\Phi_{\ell\ell}$ and on the right the product $x_1 \cdot x_2$ for different cuts on $\Delta\Phi_{\ell\ell}$. The cut applied on $\Delta\Phi_{\ell\ell}$ as given in Equation 5.10 however avoids this unphysical peak.

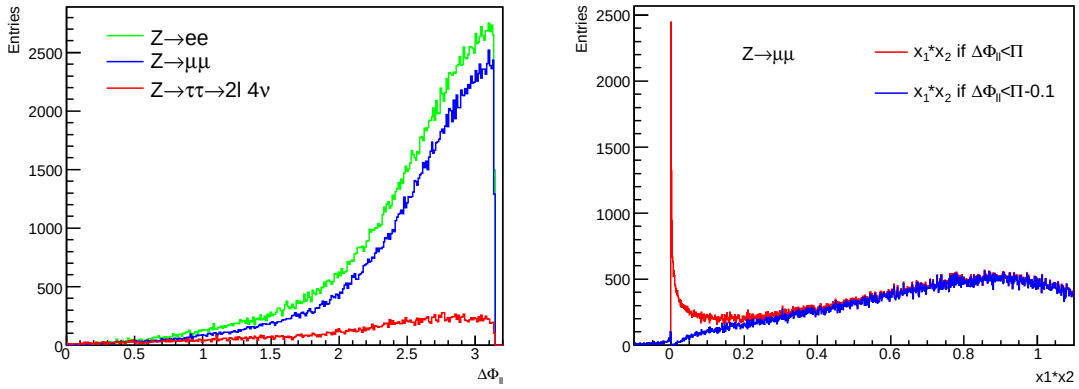

Figure 5.20: $\Delta\Phi_{\ell\ell}$ (left) and $x_1 \cdot x_2$ (right) for Z+jets.

5.4.2 Background Rejection and Mass Distribution after the Preselection

The absolute number of events passing each precut for all background processes considered are listed in Table 5.2, normalized to an integrated luminosity of 30 fb^{-1}. The rejection r is defined as follows:

$$r = \left(1 - \frac{\text{number of events after last preselection step}}{\text{number of events after trigger}}\right) \cdot 100\,\% \tag{5.12}$$

It became obvious that the WW+jets background is negligible after the precuts. From now on this process will not be considered any more. SUSY background is also minor

Process	Trigger	e/μ Select.	$\geq$1 b-Tag	$0<x_i<1$	$\Delta\Phi_{\ell\ell}<\pi$-0.1	r
$t\bar{t}$	2.63 M	943 223	704 694	168 190	158 229	93.9%
$Z \rightarrow \tau\tau$	1.5 M	880 200	23 969	18 672	17 092	98.8%
$Z \rightarrow \mu\,\mu$	38 M	23.5 M	506 181	147 440	135 840	99.6%
$Z \rightarrow e\,e$	35 M	23.5 M	580 389	206 513	188 050	99.5%
SUSY-120-20	27 694	11 499	6 383	1 953	1 889	93.2%
SUSY-200-20	28 046	12 126	6 457	2 329	2 257	92.0%
WW+jets	2 114	1 021	31	29	8	99.6%

Table 5.2: Absolute number of background events for $L = 30$ fb^{-1}.

compared to $Z + jets$ and $t\bar{t}$, but is not yet negligible. The contribution from Z+jets events is significantly reduced when requiring at least one b-tag.
Although more than 90 % of all background events are rejected by the precuts, there are still over 500 000 background events left, which is a very large number compared to the number of signal events (Table 5.1). In Figure C.1 the stacked mass distribution $m_{\tau\tau}$ for all three sub decay channels is displayed, including all remaining backgrounds and a Higgs signal at $m_A = 200GeV$ and $\tan\beta$=20 (marked as red).
In the following chapter it is explained, how a mass-dependent cut optimization can be used to increase the signal to background ratio and this way the significance of a discovery.

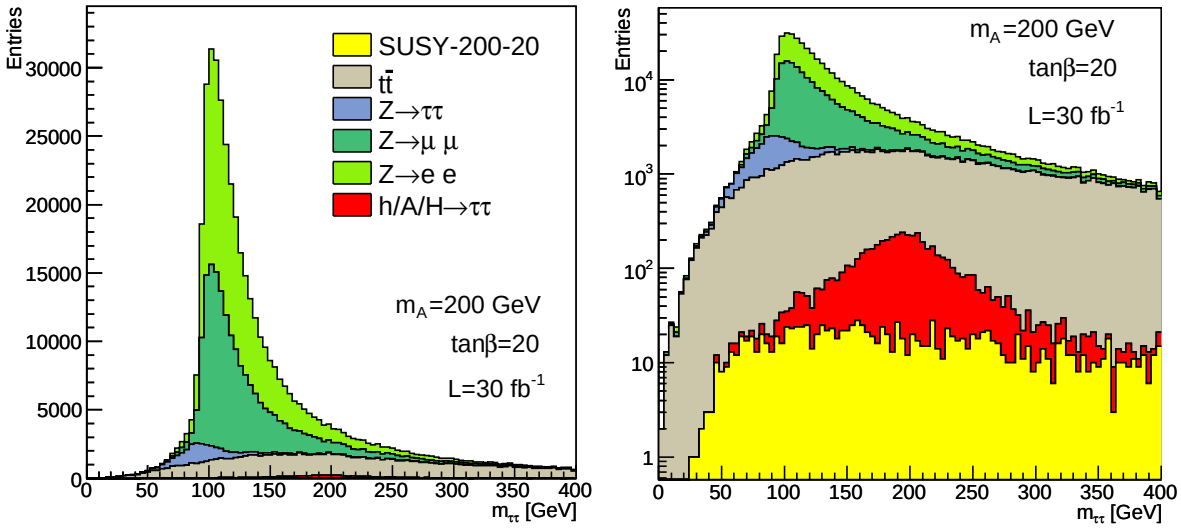

Figure 5.21: Stacked background events and 200 GeV Higgs signal events after precuts, normalized to an integrated luminosity of 30 fb^{-1}. A plot with the mass distribution broken down to the sub-decay channels is displayed in Appendix C.

Chapter 6

Cutanalysis

6.1 Method

The aim of the cutanalysis is the maximization of the statistical significance $\frac{S}{\sqrt{B}}$, given as follows:

$$\frac{S}{\sqrt{B}} = \frac{\text{Number of signal events}}{\sqrt{\text{Number of background events}}} \tag{6.1}$$

$\sqrt{B}$ is the size of the expected statistical fluctuations of the background, so $\frac{S}{\sqrt{B}}$ is directly correlated to the probability to get an upwards fluctuation of the background faking a signal. By consensus a discovery of a signal is made for $\frac{S}{\sqrt{B}} > 5$. This definition of the significance refers only to a statistical significance. In a real experiment systematics have to be included in an analysis which will lessen the significance.
An advantage of this definition of the significance is its independence of the shape of the mass distribution. Only numbers of events and therefore the cross sections and efficiencies are relevant.
The significance can be maximized by looking at distributions with distinct differences between signal and background. An optimal cut on such a distribution to reduce background while keeping much signal events can be obtained by the calculation of $\frac{S}{\sqrt{B}}$ for every cut value. Where the significance takes its maximum value, the cut is applied. Figure 6.1 demonstrates this method for example for $x_1 \cdot x_2$ in the e-e channel for a signal with $m_A = 120$ GeV and $\tan\beta$=20. It is also shown how the signal efficiency and background rejection depend on the cut value.
The cuts on the following variables will be optimized using this method:

- Invariant lepton-lepton mass $m_{\ell\ell}$
- p_T of the di-lepton system $p_{T,\ell\ell}$
- p_T of the leading b-jet $p_{T,b-jet}$
- p_T of the Higgs boson candidate $p_{T,Higgs}$
- $x_1 \cdot x_2$
- Missing transverse momentum

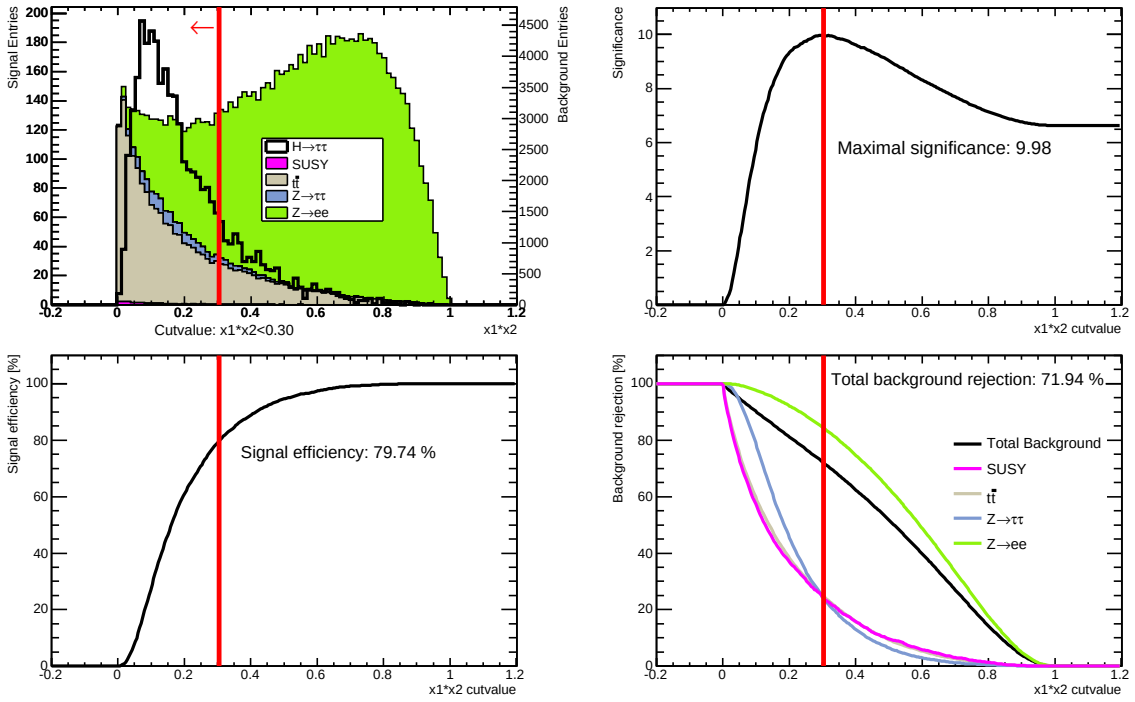

Figure 6.1: Demonstration of the cutmethod. An optimal cutvalue on $x_1 \cdot x_2$ is obtained by maximizing the significance (m_A=120 GeV, $\tan\beta$=20, 30 fb^{-1}). The top left plot shows the signal and background entries. The background is stacked and scaled for better visibility. The top right plots shows the significance having a distinct maximum. The bottom plots show the signal efficiency and the background rejection. The best cutvalue in this example is $x_1 \cdot x_2 = 0.3$, marked with a red line. The red arrow points into the direction of the kept region.

Other quantities such as $x_1 + x_2$, lepton p_T or $p_{T,b-jet} - p_{T,Higgs}$ have been tested. They would also be suited for cutting but are strongly correlated to the quantities listed above and do not improve the significance further. No cut on $m_{\tau\tau}$ will be applied but later a sliding mass window will be discussed.
The listed variable depend on the Higgs mass and show differences for each sub decay channel, so separate cut optimizations depending on mass and decay channels had to be performed.
Some or all of the variables considered might be significantly correlated. Two possible methods were considered:

- Multi-dimensional cuts
  By using two or higher dimensional cuts all possible correlations between these quantities are taken into account automatically.
  Such an optimization will use more time than optimizing an one-dimensional distribution.

- Iterative method
  Another way of dealing with correlations is to iterate the significance optimization on different distributions until the cutvalues converge and no or little further improvement can be achieved.

The iteration of millions of events is time-consuming, wherefore a skim of the generated samples had to be made. All events passing the preselection are skimmed into smaller data samples.

In this analysis a combination of both approaches has been used. At the beginning a two-dimensional cut on $m_{\ell\ell}$ and $p_{T,\ell\ell}$ was optimized in the $e-e$ and $\mu-\mu$ channels. This reduced the background contribution from $Z \to ee$ and $Z \to \mu\mu$, respectively. In the following one-dimensional cuts on five distributions are iteratively optimized. This reduces mainly the $t\bar{t}$ and SUSY background contributions. Figure 6.2 displays a scheme with the principle steps of the iteration. About five iterations where applied for obtaining the final cutvalues.

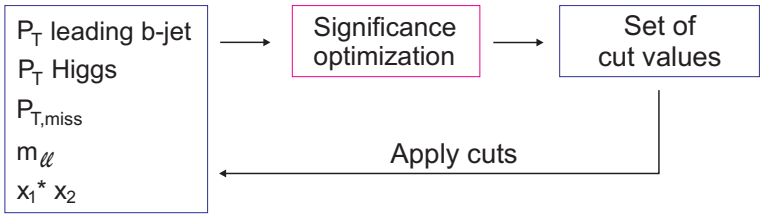

Figure 6.2: Scheme of the iterative cut optimization step. This is performed in all three channels separately.

The separate cut optimization in the three sub-channels is complicating the analysis but has some advantages. Although the $e-e$ and $\mu-\mu$ channels are very similar, there are differences in important quantities such as $p_{T,miss}$ which can then be taken into account. Since there are much less $Z \to ee$ and $Z \to \mu\mu$ background events in the mixed channel, the cutvalues in the $e-\mu$ channel differ significantly from these of the other two channels. The separation of the cutanalysis can also be used to optimize only one or two sub-channels or to compare the results for the obtained significance among the channels.

6.2 Cut optimization for a 120 GeV Higgs boson

6.2.1 Cutflow in the e − e channel

All optimized cut values for $m_A = 120$ GeV are summarized in Table 6.4 in section 6.2.4. In Figure 6.3 the first step, the two dimensional cut on $m_{\ell\ell}$ versus $p_{T,\ell\ell}$ is displayed. Events lying within the labeled rectangle are kept, every event outside this region is rejected. The position of the bottom left corner of the rectangle is calculated by maximizing the significance when cutting away all events with smaller values of $m_{\ell\ell}$ and $p_{T,\ell\ell}$ than the cutvalue. The top right corner of the rectangle marks the maximum of the significance when keeping all events with smaller values of $m_{\ell\ell}$ and $p_{T,\ell\ell}$ than the cutvalue. The figure shows that especially the $Z \to ee$ background (red entries in the background plot at $m_{\ell\ell} \approx$ 90 GeV) is rejected by this first cut.
The next steps of the cut procedure are five one-dimensional cuts. The plots in Figure 6.4 display the individual distributions and the optimal cut values. The events within the marked lines are kept. The figures are made after having applied the 2D cut. They show that many events originating from $Z \to \tau\tau$ events are lying within the kept region.

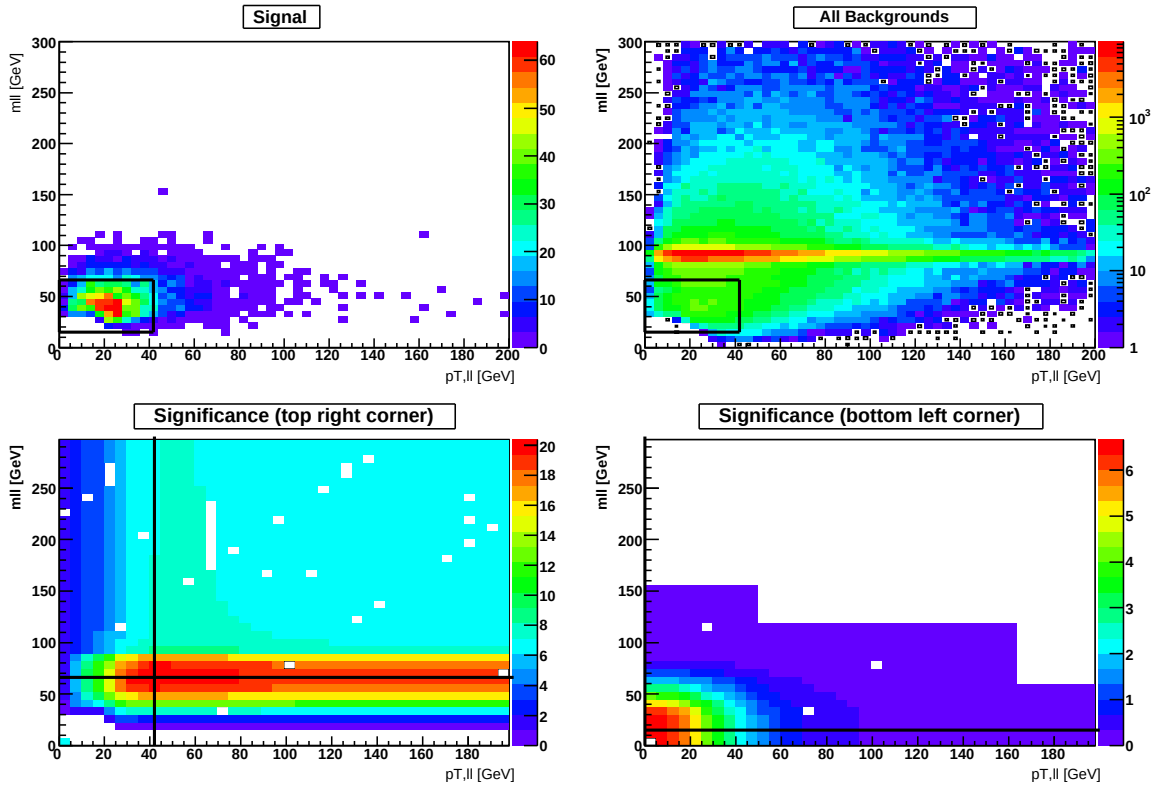

Figure 6.3: 2D cut on $m_{\ell\ell}$ vs. $p_{T,\ell\ell}$ in the $e-e$ channel for m_A=120 GeV and $\tan\beta$=20 at 30 fb^{-1}. The top left plot shows the signal events, the top right plot are the background events. The bottom plots show the significance depending on $m_{\ell\ell}$ vs. $p_{T,\ell\ell}$. The left plot shows the significance when cutting away events with $m_{\ell\ell}$ and $p_{T,\ell\ell}$ values *higher* than the cutvalue marking the top right corner of the black lined rectangle. The bottom right plot shows the significance when cutting away events with $m_{\ell\ell}$ and $p_{T,\ell\ell}$ values *smaller* than the cutvalue marking the bottom left corner of the black lined rectangle. Events inside the rectangle are kept.

This is due to the very similar event topology of $Z \to \tau\tau$ and $\Phi \to \tau\tau$ and the similar mass. The absolute number of events after each cut normalized to $L = 30$ fb^{-1} are given in Table 6.1. For the signal column the efficiency ϵ and for the background columns the rejection r are calculated. They are defined as follows:

$$\begin{aligned} \epsilon &= \frac{Event\ numbers\ after\ last\ cut}{Event\ numbers\ after\ precuts} \cdot 100\ \% \\ r &= 100\ \% - \epsilon \end{aligned} \tag{6.2}$$

The statistical significance for a signal after precuts was 6.6. After optimization a statistical significance of 24.9 was obtained for a Higgs boson of mass $m_H = 120$ GeV.

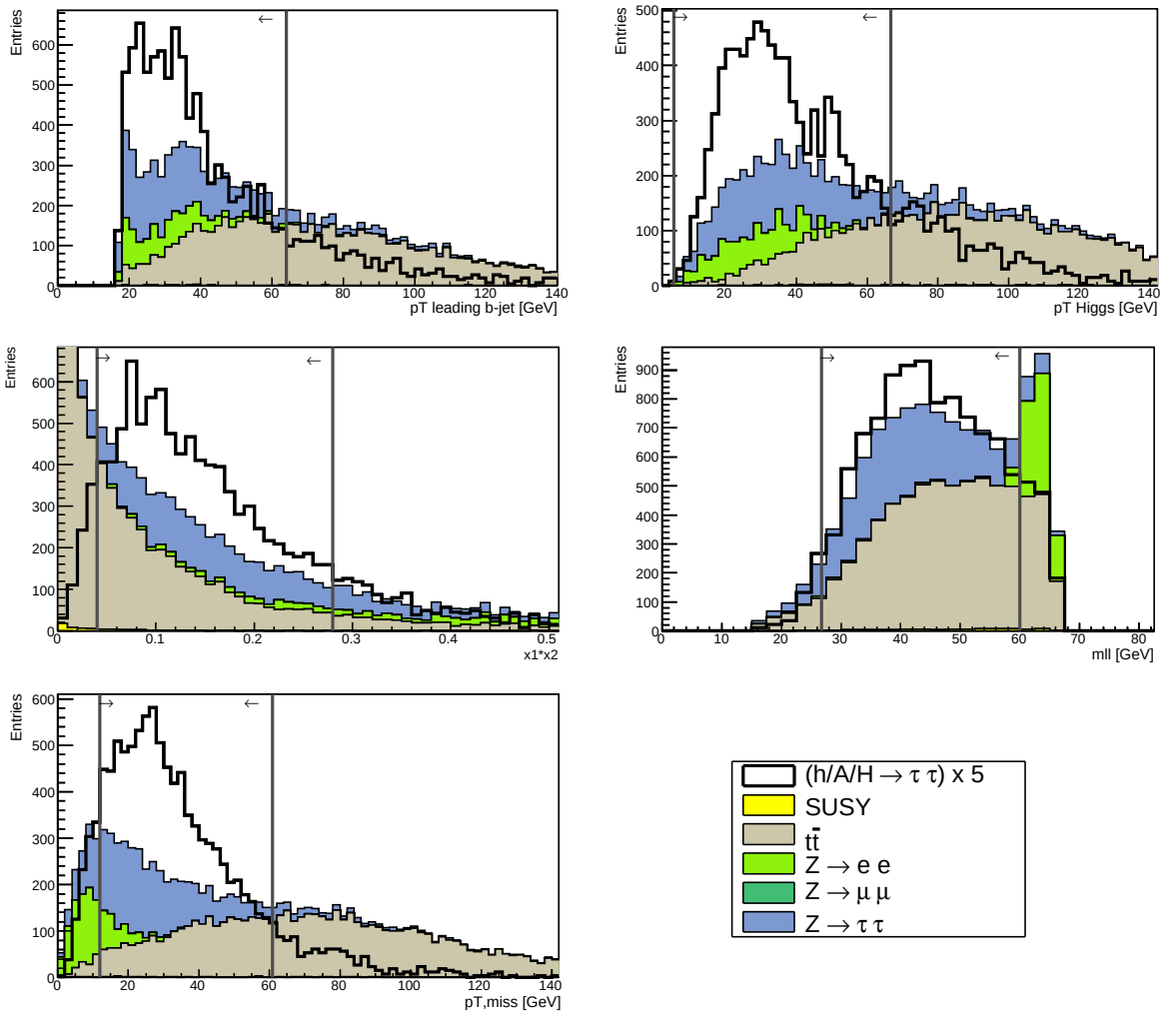

Figure 6.4: Distributions entering the cutanalysis for m_A=120 GeV in the $e-e$ channel (m_A=120 GeV, $\tan\beta$=20, L=30 fb^{-1}). The events kept in the analyse are indicated by the arrows. The displayed signal distributions are scaled for better visibility.

Cut	Signal	$t\bar{t}$	$Z \to ee$	$Z \to \tau\tau$	SUSY
Precuts	3 220	43 871	187 970	4 501	715
(15<$m_{\ell\ell}$<66) & (0<$p_{T,\ell\ell}$<42) GeV	2 178	6 914	1 039	3 263	87
(0<$p_{T,b-jet}$<64) GeV	1 795	2 787	1 000	2 787	23
(5<$p_{T,Higgs}$<67) GeV	1 614	803	993	2 437	11
0.04<$x_1 \cdot x_2$<0.28	1 235	401	251	1 620	3
(27<$m_{\ell\ell}$<60) GeV	1 113	336	53	1 518	3
(12<$p_{T,miss}$<61) GeV	1 027	314	33	1 357	2
ϵ resp. r [%]	31.9	99.3	99.9	69.8	99.7

Table 6.1: Number of events in the $e-e$ channel for m_A = 120 GeV, $\tan\beta$=20 and L=30 fb^{-1}.

6.2.2 Cutflow in the $\mu - \mu$ channel

The result for the two dimensional cut optimization is displayed in Figure 6.5. The following cuts on the one dimensional distributions are shown in Figure 6.6. The total number of events remaining are displayed in Table 6.2. The statistical significance has been increased from 8.4 after precuts to 30.6 after optimization for a Higgs boson of mass $m_H = 120$ GeV.

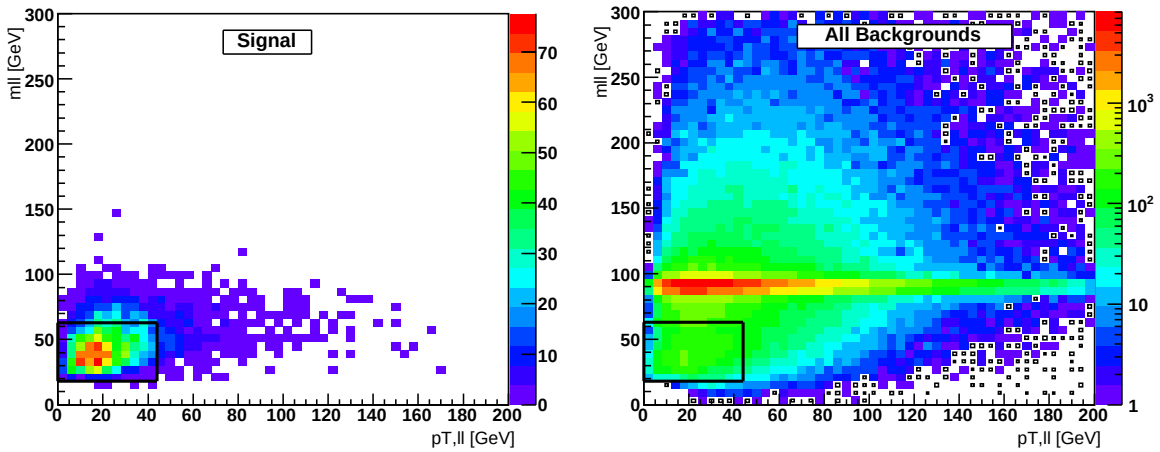

Figure 6.5: 2D cut on $m_{\ell\ell}$ vs. $p_{T,\ell\ell}$ in the $\mu - \mu$ channel for m_A=120 GeV, normalized to $L = 30\,\mathrm{fb}^{-1}$.

Cut	Signal	$t\bar{t}$	$Z \to \mu\mu$	$Z \to \tau\tau$	SUSY
Precuts	3 515	36 189	135 679	4689	471
$(18<m_{\ell\ell}<63)$ & $(0<p_{T,\ell\ell}<44)$ GeV	2 525	5579	462	3777	63
$(0<p_{T,b-jet}<64)$ GeV	2 102	2108	449	3236	14
$(5<p_{T,Higgs}<68)$ GeV	1 929	592	448	2886	7
$0.03<x_1 \cdot x_2<0.34$	1 674	357	125	2316	3
$(28<m_{\ell\ell}<60)$ GeV	1 510	299	13	1999	3
$(11<p_{T,miss}<60)$ GeV	1 407	278	10	1818	3
ϵ resp. r [%]	40.0	99.2	99.9	61.2	99.4

Table 6.2: Number of events in the $\mu - \mu$ channel for $m_A = 120$ GeV, $\tan\beta$=20 and L=30 fb^{-1}.

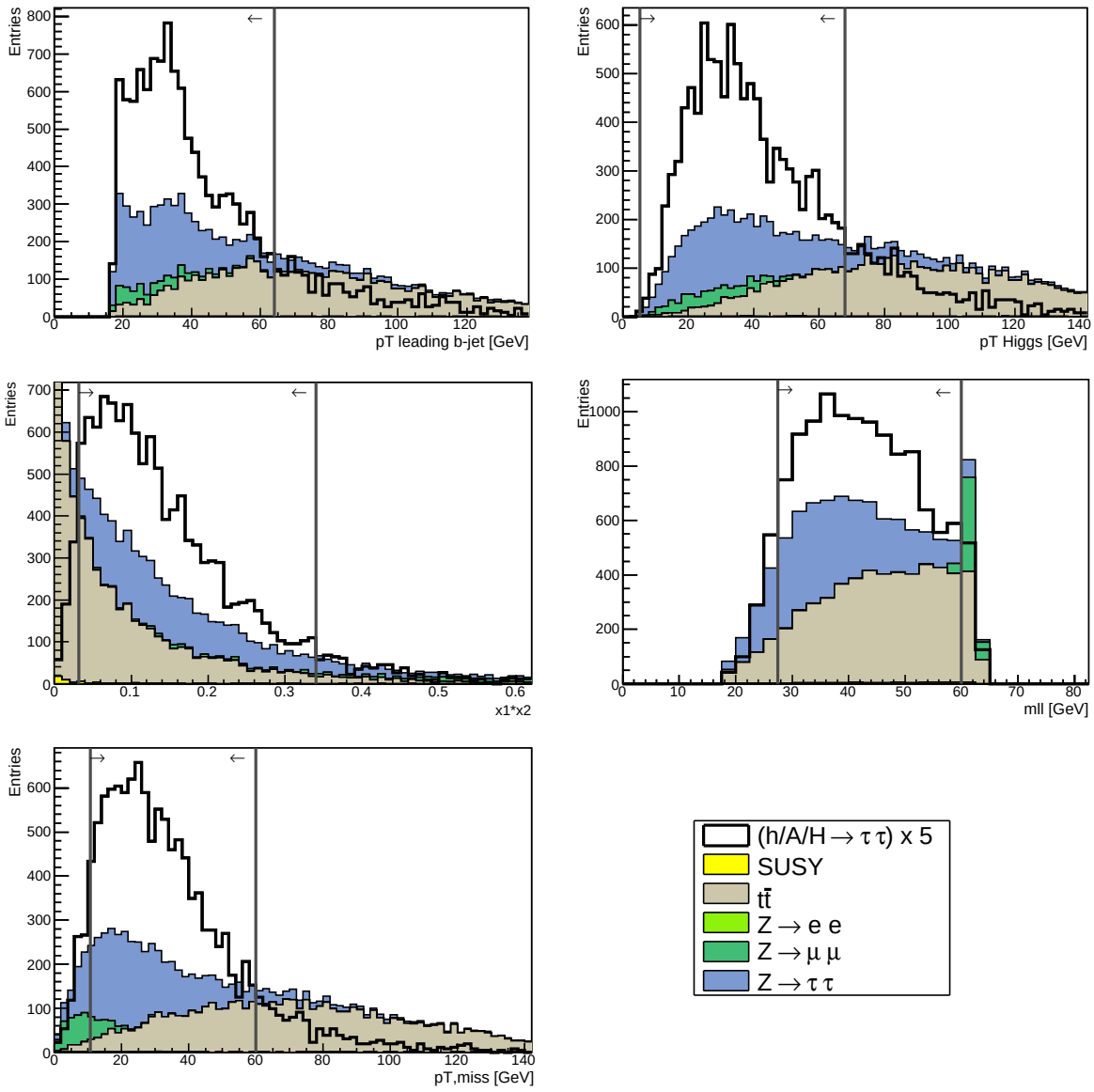

Figure 6.6: Distributions entering the cutanalysis in the $\mu-\mu$ channel (m_A=120 GeV, $\tan\beta$=20, L=30 fb^{-1}). The signal events are scaled for better visibility. The events kept in the analysis are indicated by arrows.

6.2.3 Cutflow in the e $-$ μ channel

In the mixed channel no 2D cut has been applied, due to the missing contribution from $Z \to \ell\ell$. The number of events are listed in Table 6.3 and the distributions displayed in Figure 6.7. The statistical significance has been increased from 21.2 after precuts to 40.0.

Cut	Signal	$t\bar{t}$	$Z \to ee$	$Z \to \mu\mu$	$Z \to \tau\tau$	SUSY
Precuts	6287	78 169	135	745	7 902	703
$(0<p_{T,b-jet}<44)$ GeV	3572	13455	42	127	4576	64
$(5<p_{T,Higgs}<47)$ GeV	2721	1014	27	71	3017	2
$0.03<x_1 \cdot x_2<0.8$	2589	894	26	64	2894	2
$(25<m_{\ell\ell}<73)$ GeV	2321	262	19	40	2821	1
$(3<p_{T,miss}<41)$ GeV	2186	218	17	38	2717	0
ϵ resp. r [%]	34.3	99.7	87.4	94.9	65.6	100

Table 6.3: Number of events in the $e-\mu$ channel for $m_A = 120$ GeV, $\tan\beta$=20 and L=30 fb^{-1}.

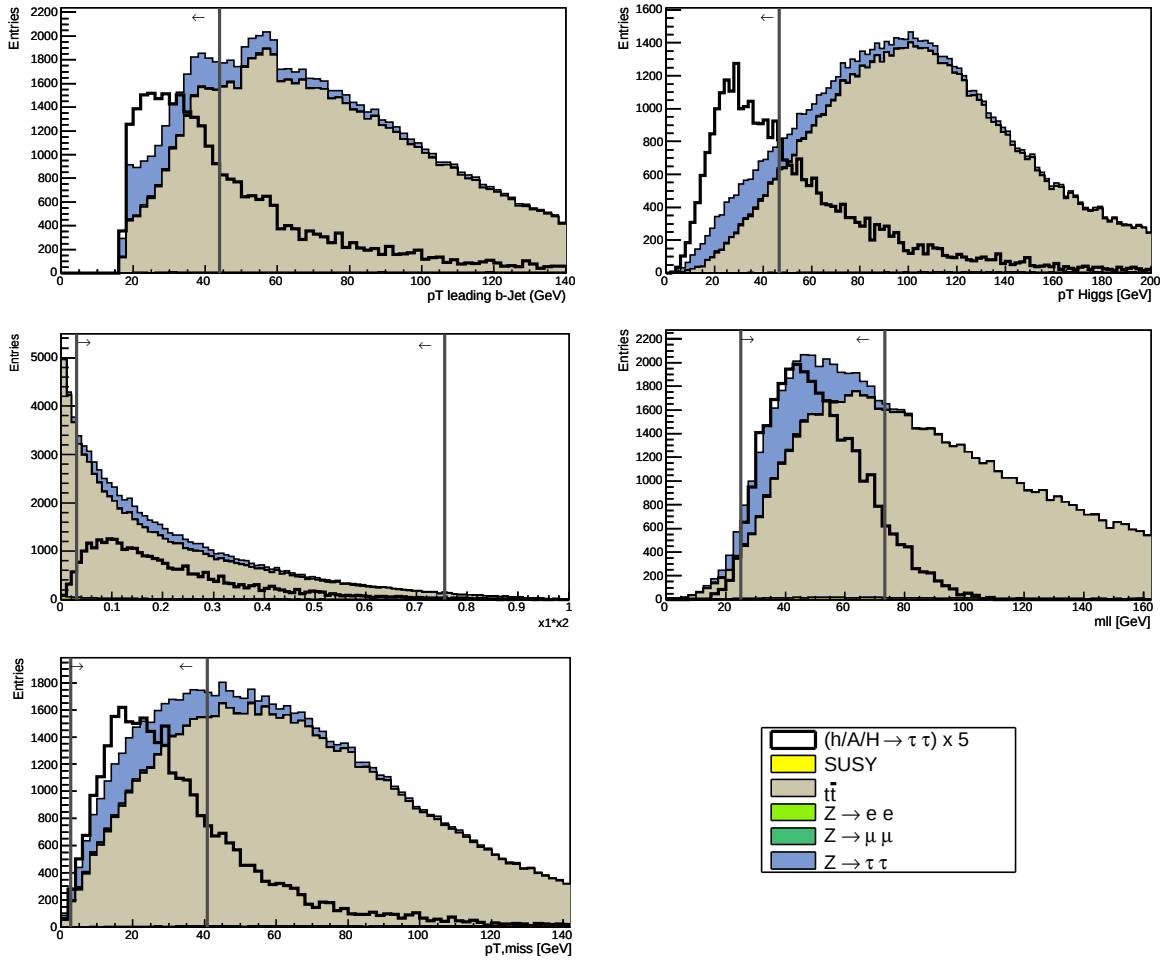

Figure 6.7: Distributions in the $e-\mu$ channel (m_A=120 GeV, $\tan\beta$=20, L=30 fb^{-1}). The signal events are scaled for better visibilty. Events kept in the analysis are indicated by arrows.

6.2.4 Summary and Results for m_A=120 GeV

The optimized cutvalues for the three channels are summarized in Table 6.4.

Quantity		$e-e$		$\mu-\mu$		$e-\mu$	
2D $m_{\ell\ell}$	[GeV]	15	66	18	63		
2D $p_{T,\ell\ell}$	[GeV]	0	42	0	44		
$p_{T,b-jet}$	[GeV]	0	64	0	64	0	44
$p_{T,Higgs}$	[GeV]	5.3	66.7	5.3	68	0	46.7
$x_1 \cdot x_2$		0.04	0.28	0.032	0.34	0.03	0.76
$m_{\ell\ell}$	[GeV]	26.7	60	27.5	60	25	73.3
$p_{T,miss}$	[GeV]	12	61	10.7	60	2.7	40.7

Table 6.4: Cutvalues for m_A=120 GeV.

The stacked $m_{\tau\tau}$ distributions after the cutoptimization are displayed in Figure 6.8. The dominant background from $Z \to ee$ and $Z \to \mu\mu$ events is relatively completely reduced. SUSY background turned out to be completely negligible either. The $t\bar{t}$ background is almost flat in $m_{\tau\tau}$ and was strongly reduced. $Z \to \tau\tau$ is irreducible as expected. Because of the large width of the reconstructed Higgs and Z^0 bosons, a separation of the two peaks is not possible at this m_A point. Yet - in the real experiment - a comparison of the counted events to the expectation following from the Z^0 cross section could also lead to a discovery of the Higgs particle.

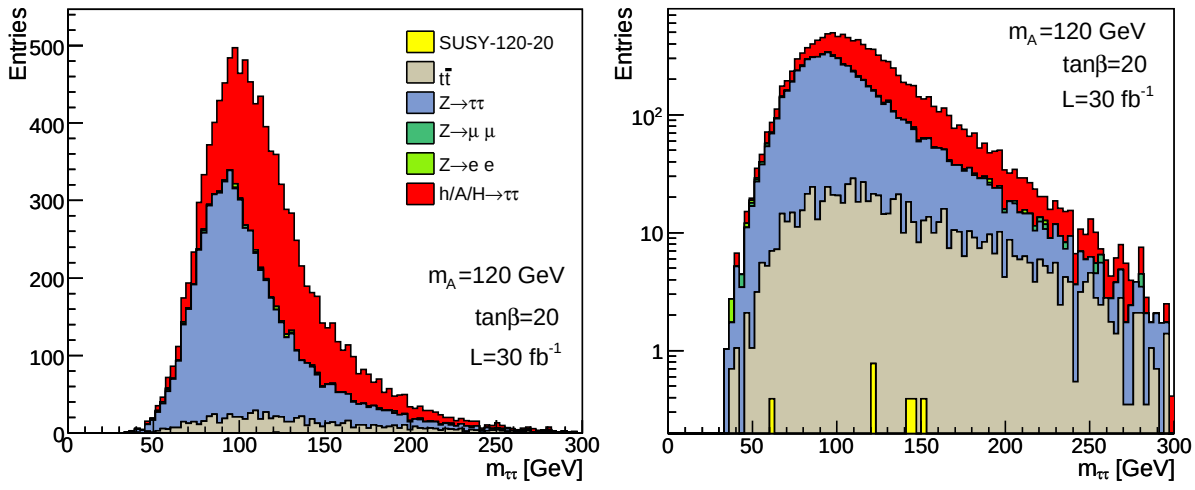

Figure 6.8: Final $m_{\tau\tau}$ spectrum after all cuts (m_A=120 GeV, $\tan\beta$=20, L=30 fb^{-1}). Red entries label events from Higgs decays. A plot with the mass distribution broken down to the sub-decay channels is displayed in Appendix C.

The final significance for an integrated luminosity of 30 fb^{-1} at $\tan\beta$=20 combining all sub channels is:

$$\frac{S}{\sqrt{B}} = \frac{4607}{\sqrt{6868}} = 55.59 \tag{6.3}$$

The number of events entered has been counted in the mass range $0 < m_A < 300$ GeV.

6.3 Cut optimization for a 160 GeV Higgs boson

For this cut optimization SUSY background has not been taken into account, because no sample for $m_A = 160$ GeV was available. This is justified because the cut optimization for a 120 GeV Higgs boson clearly showed that SUSY background is negligible after a few cuts.

6.3.1 Cutflow in the $e - e$ channel

The 2D cut is displayed in Figure 6.9. The other five distributions are shown in Figure 6.10. The absolute number of events are listed in Table 6.5. The statistical significance has been increased from 4.3 after precuts to 14.7.

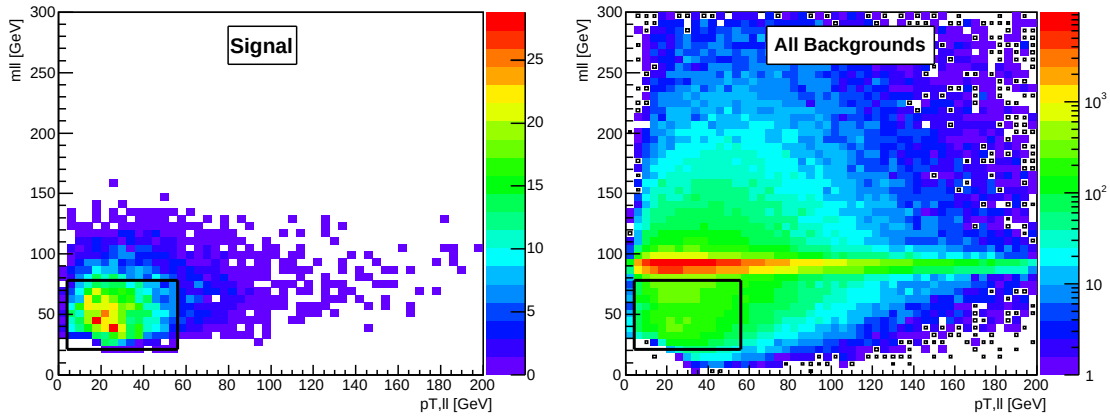

Figure 6.9: 2D Cut in the $e - e$ channel for m_A=160 GeV. ($\tan\beta$=20, L=30 fb^{-1}). The signal events are scaled for better visibilty. Events kept in the analysis are indicated by arrows.

Cut	Signal	$t\bar{t}$	$Z \to ee$	$Z \to \tau\tau$
Precuts	2070	43 871	187 970	4501
(21<$m_{\ell\ell}$<78) & (4<$p_{T,\ell\ell}$<56) GeV	1393	12033	4454	3801
(0<$p_{T,b-jet}$<70) GeV	1122	5519	4282	3233
(0<$p_{T,Higgs}$<71) GeV	973	1615	4245	2766
0.02<$x_1 \cdot x_2$<0.25	836	922	767	1733
(32<$m_{\ell\ell}$<78) GeV	800	889	761	1466
(15<$p_{T,miss}$<79) GeV	706	835	303	1183
ϵ resp. r [%]	34.1	98.1	99.8	73.7

Table 6.5: Number of events in the $e - e$ channel for $m_A = 160$ GeV, $\tan\beta$=20 and L=30 fb^{-1}.

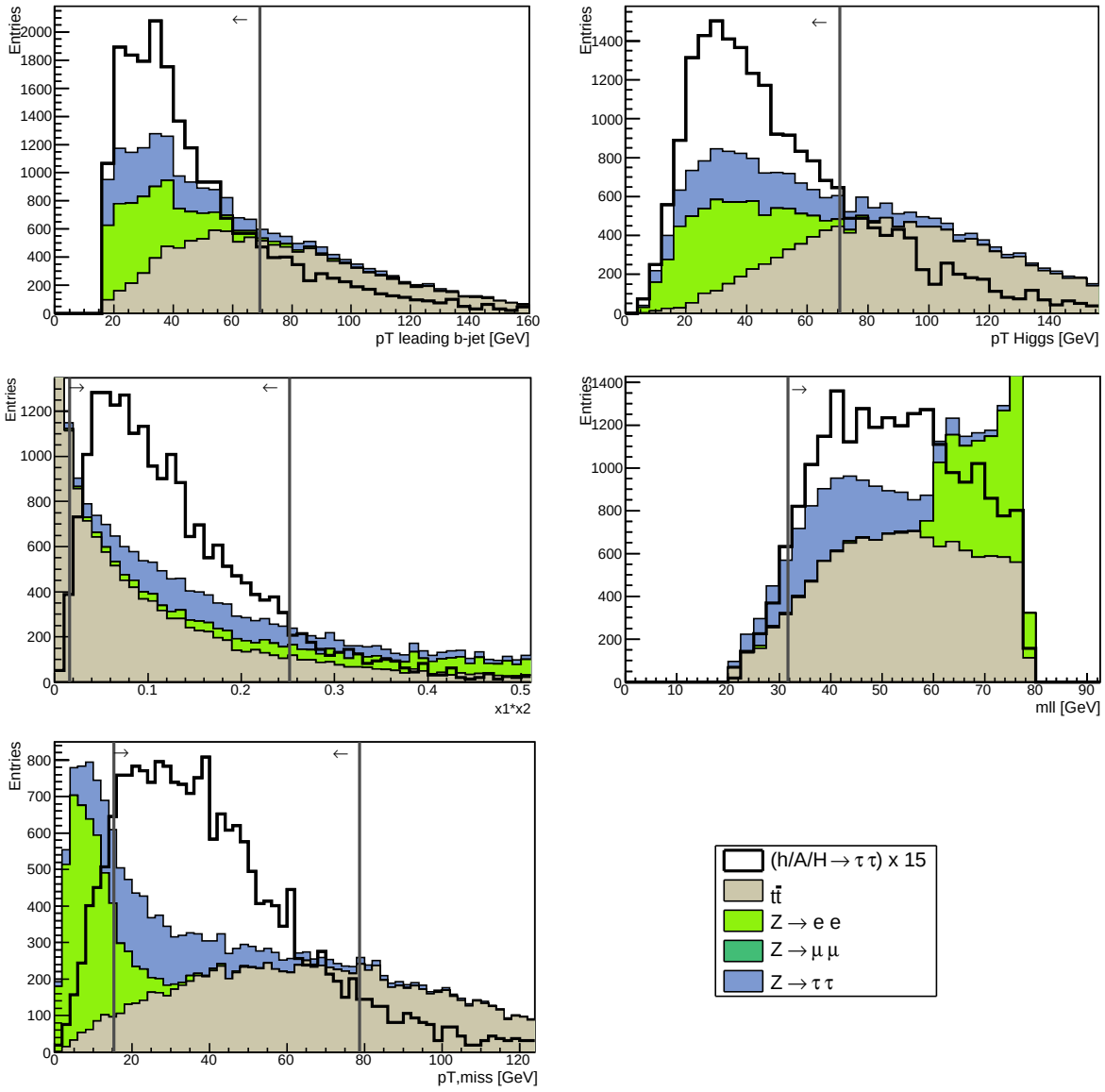

Figure 6.10: Distributions entering the cutanalysis in the $e - e$ channel (m_A=160 GeV, $\tan\beta$=20, L=30 fb^{-1}). The signal events are scaled for better visibility. Events kept in the analysis are indicated by arrows.

6.3.2 Cutflow in the $\mu - \mu$ channel

The 2D cut is shown in Figure 6.11. The other five distributions are displayed in Figure 6.12. The absolute number of events are listed in Table 6.6. After precuts the statistical significance takes a value of 4.9 in this channel. After applying the optimized cuts it is around 16.

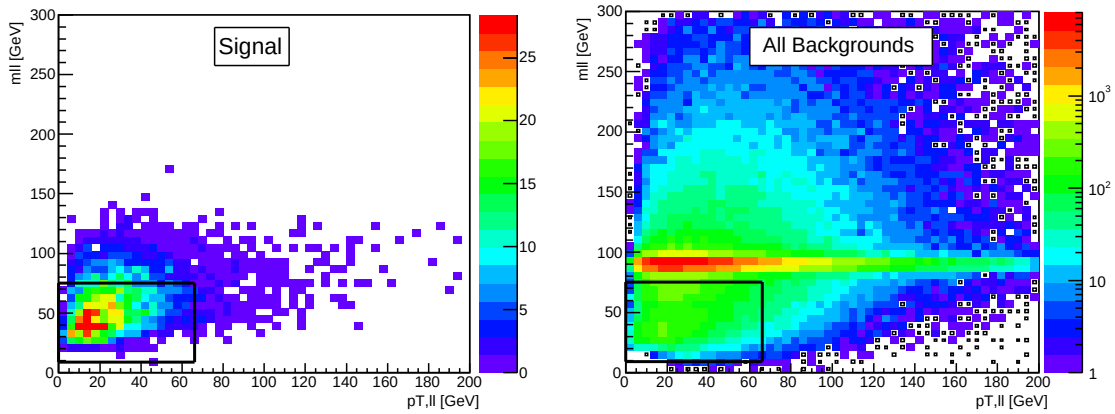

Figure 6.11: 2D Cut in the $\mu - \mu$ channel for m_A=160 GeV. ($\tan\beta$=20, L=30 fb^{-1}).

Cut	Signal	$t\bar{t}$	$Z \to \mu\mu$	$Z \to \tau\tau$
Precuts	2084	36189	135 679	4689
(21<$m_{\ell\ell}$<78) & (0<$p_{T,\ell\ell}$<56) GeV	1559	10834	3875	4276
(0<$p_{T,b-jet}$<67) GeV	1242	4416	3690	3610
(0<$p_{T,Higgs}$<75) GeV	1110	1315	3663	3218
0.02<$x_1 \cdot x_2$<0.22	869	652	478	1937
(33<$m_{\ell\ell}$<73) GeV	753	527	343	1124
(17<$p_{T,miss}$<80) GeV	612	495	96	850
ϵ resp. r [%]	29.3	98.6	99.9	81.9

Table 6.6: Number of events in the $\mu - \mu$ channel for m_A = 160 GeV, $\tan\beta$=20 and L=30 fb^{-1}.

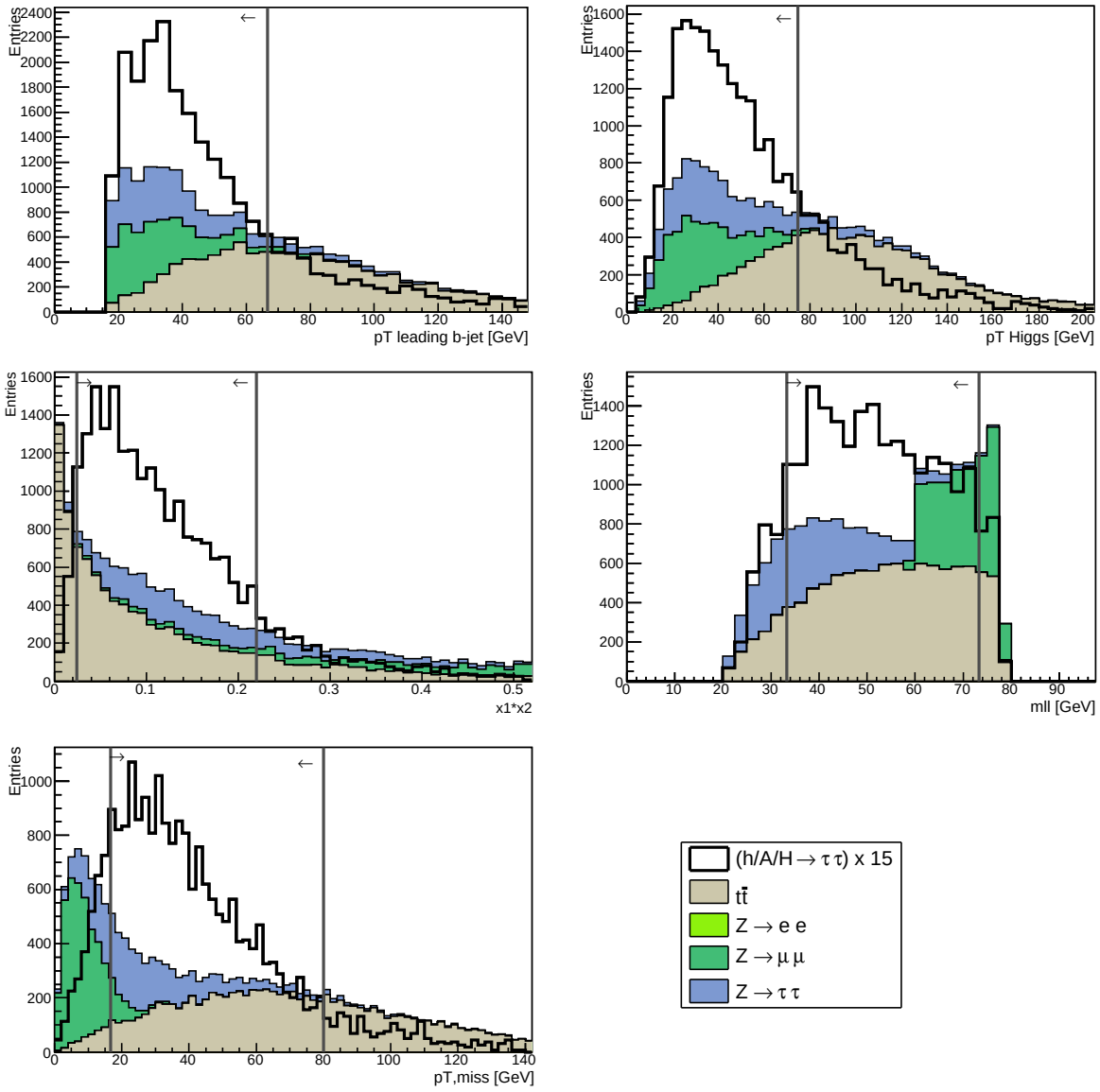

Figure 6.12: Distributions entering the cutanalysis in the $\mu - \mu$ channel (m_A=160 GeV, $\tan\beta$=20, L=30 fb^{-1}). The signal events are scaled for better visibility. Events kept in the analysis are indicated by arrows.

6.3.3 Cutflow in the e $-$ μ channel

The five one dimensional cut distributions are displayed in Figure 6.13. The absolute number of events are listed in Table 6.7. In the mixed channel the statistical significance has been increased from 12.8 to 26.4.

Cuts	Signal	$t\bar{t}$	$Z \to ee$	$Z \to \mu\mu$	$Z \to \tau\tau$
Precuts	3780	78169	135	745	7902
$(0<p_{T,b-jet}<51)$ GeV	2328	19024	49	142	5214
$(0<p_{T,Higgs}<55)$ GeV	1818	2220	37	91	3777
$0.03<x_1 \cdot x_2<0.5$	1636	1707	27	73	3362
$(49<m_{\ell\ell}<108)$ GeV	1087	792	6	26	958
$(3<p_{T,miss}<65)$ GeV	1101	748	6	26	954
ϵ resp. r [%]	29.1	99.0	95.6	96.5	87.9

Table 6.7: Number of events in the $e-\mu$ channel for $m_A = 160$ GeV, $\tan\beta$=20 and L=30 fb^{-1}.

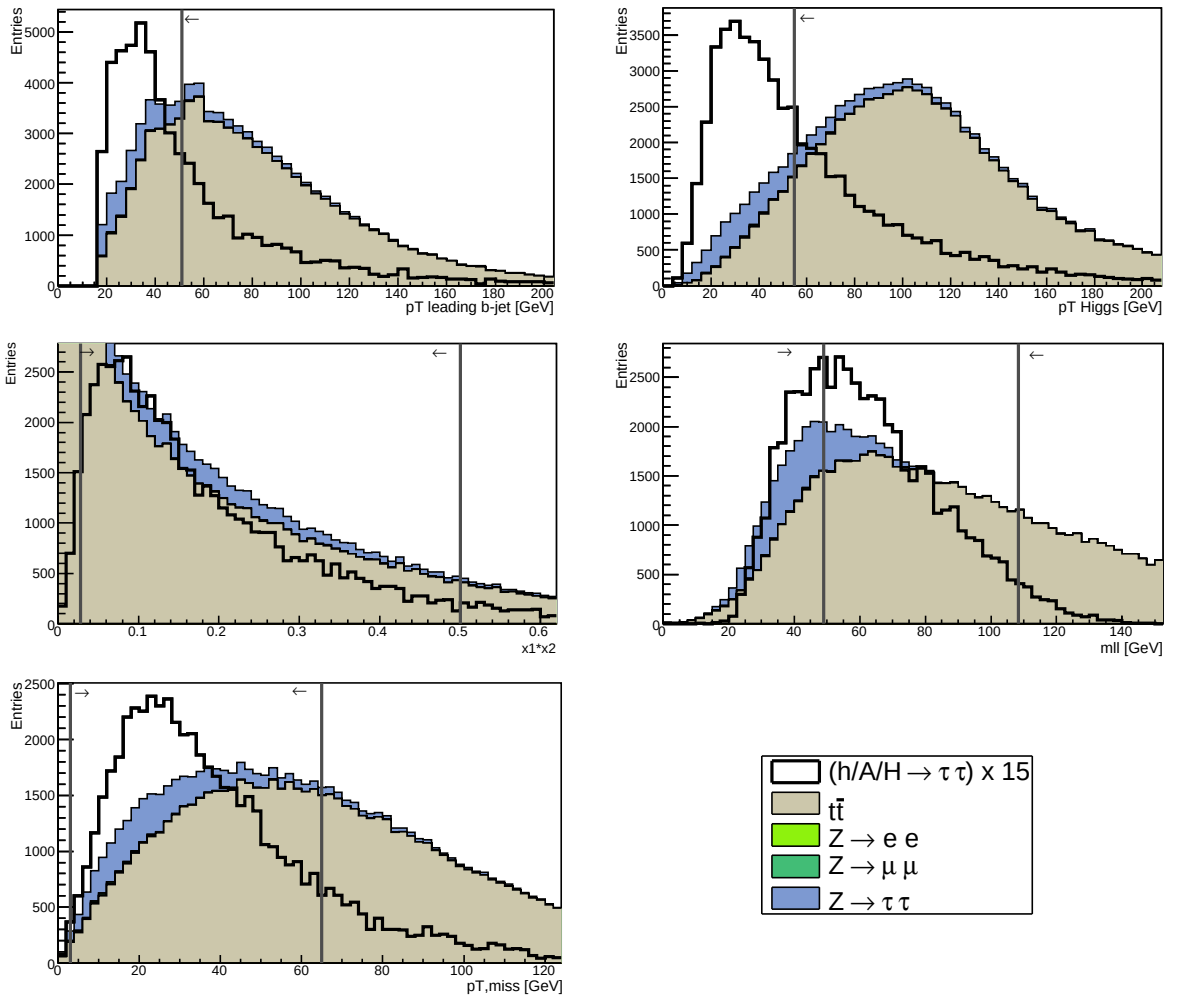

Figure 6.13: Distributions in the $e-\mu$ channel (m_A=160 GeV, $\tan\beta$=20, L=30 fb^{-1}). The signal events are scaled for better visibility. Events kept in the analysis are indicated by arrows.

6.3.4 Summary and Results for m_A=160 GeV

The optimized cutvalues are listed in Table 6.8.

Quantity		$e-e$		$\mu-\mu$		$e-\mu$	
2D $m_{\ell\ell}$	[GeV]	21	78	21	78		
2D $p_{T,\ell\ell}$	[GeV]	4	56	0	66		
$p_{T,b-jet}$	[GeV]	0	69.3	0	66.7	0	51
$p_{T,Higgs}$	[GeV]	0.0	70.7	0	74.7	0	54.7
$x_1 \cdot x_2$		0.016	0.252	0.024	0.22	0.028	0.5
$m_{\ell\ell}$	[GeV]	31.7	78	33.3	73.3	49	108.3
$p_{T,miss}$	[GeV]	15.3	78.7	16.7	80.0	3.0	65

Table 6.8: Cutvalues for m_A=160 GeV.

The final $m_{\tau\tau}$ spectrum after all cuts is displayed in Figure 6.14. The main background contributions are events from $Z \to \tau\tau$ decays. $t\bar{t}$ is not as flat as the $m_{\tau\tau}$ shape for m_A=120 GeV (Figure 6.8) but has a clear mamimum at 160 GeV. There are also some entries coming from $Z \to \ell\ell$ at masses around 160 GeV.

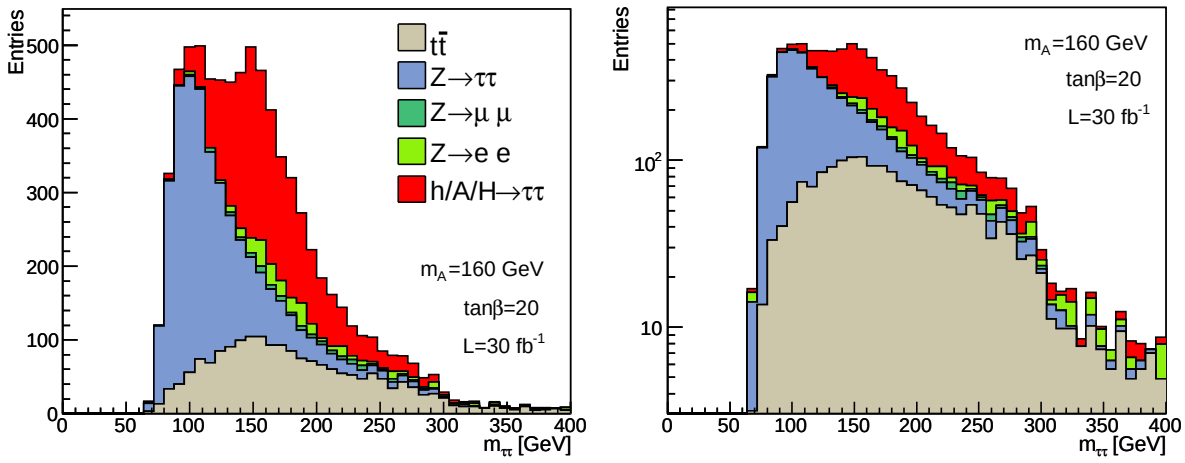

Figure 6.14: Final $m_{\tau\tau}$ spectrum after all cuts (m_A=160 GeV, tan β=20, L=30 fb^{-1}).

The significance in the mass range $0 < m_A < 400$ GeV for tan β=20 amounts to:

$$\frac{S}{\sqrt{B}} = \frac{2421}{\sqrt{5263}} = 33.38 \tag{6.4}$$

This value is smaller than the significance for a 120 GeV Higgs boson. This is consistent with the smaller cross section.

6.4 Cut optimization for a 200 GeV Higgs boson

The optimization was also applied for the 200 GeV Higgs mass hypotheses, including SUSY background.

6.4.1 Cutflow in the e – e channel

The 2D cut is shown in Figure 6.15. The other five distributions are displayed in Figure 6.16. The absolute number of events are listed in Table 6.9. The statistical significance has been improved from 2.4 after precuts to 8.2.

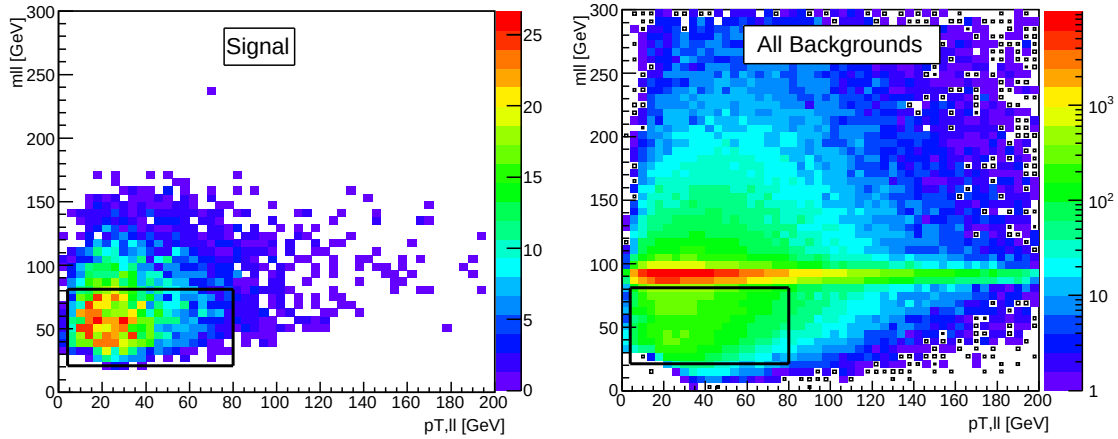

Figure 6.15: 2D Cut in the $\mu - \mu$ channel for m_A=200 GeV. ($\tan\beta$=20, L=30 fb^{-1}).

Cuts	Signal	$t\bar{t}$	$Z \to ee$	$Z \to \tau\tau$	SUSY
Precuts	1163	43 871	187970	4501	734
(24<$m_{\ell\ell}$<84) & (4<$p_{T,\ell\ell}$<74) GeV	720	16057	9593	4035	197
(0<$p_{T,b-jet}$<55) GeV	460	4749	8250	2963	40
(0<$p_{T,Higgs}$<63) GeV	376	915	7665	2379	13
0.02<$x_1 \cdot x_2$<0.16	269	372	602	838	4
(39<$m_{\ell\ell}$<80) GeV	227	313	374	373	3
(20<$p_{T,miss}$<200) GeV	196	284	78	214	2
ϵ resp. r [%]	16.9	99.4	99.9	94.6	99.7

Table 6.9: Number of events in the $e - e$ channel for m_A = 200 GeV, $\tan\beta$=20 and L=30 fb^{-1}.

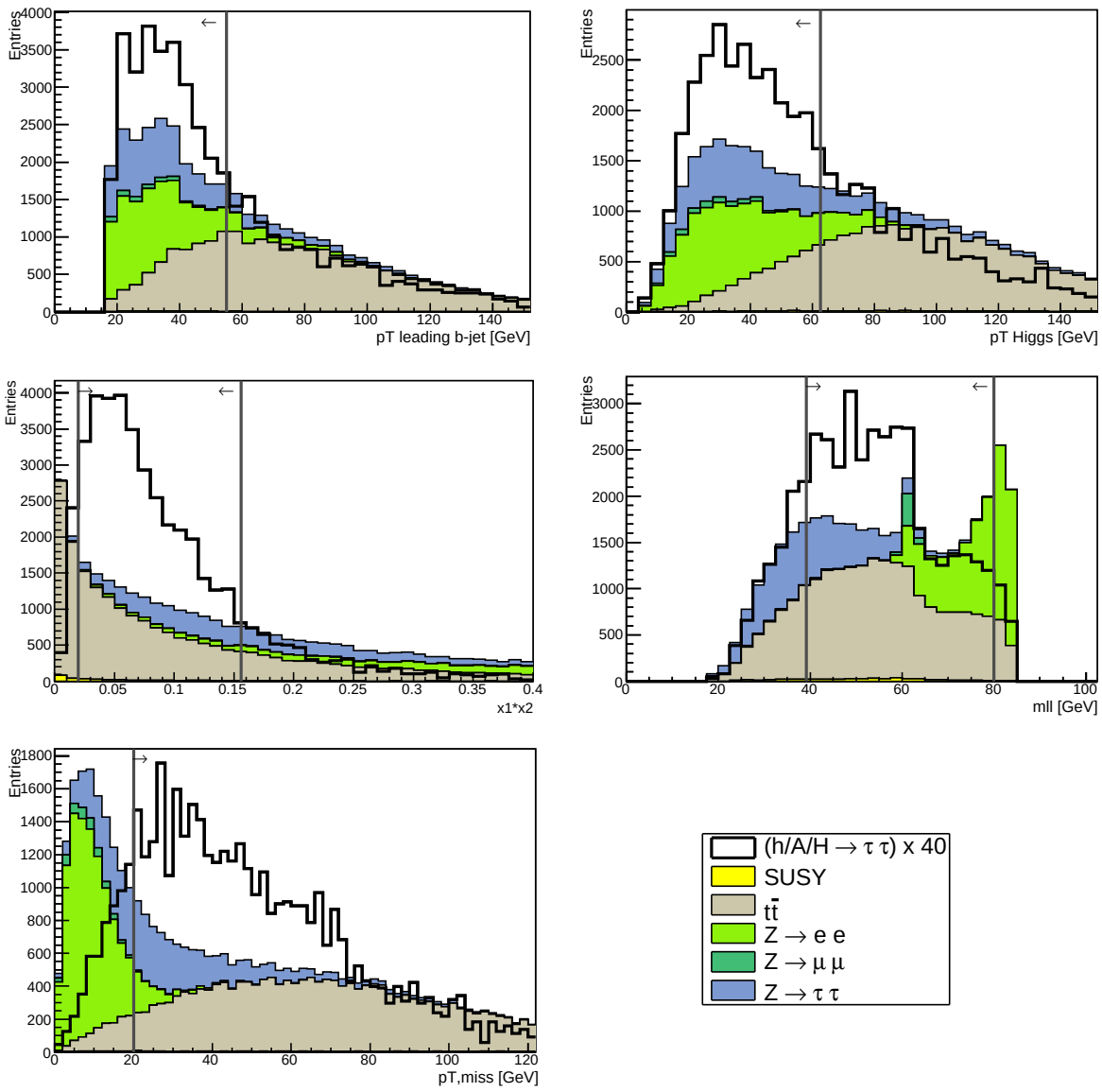

Figure 6.16: Distributions entering the cutanalysis in the $e - e$ channel (m_A=200 GeV, $\tan\beta$=20, L=30 fb^{-1}). The signal events are scaled for better visibility. Events kept in the analysis are indicated by arrows.

6.4.2 Cutflow in the $\mu - \mu$ channel

The 2D cut is shown in Figure 6.17. The other five distributions are displayed in Figure 6.18. The absolute number of events are listed in Table 6.10. The statistical significance has been optimized to 8.7 from a value of 2.6. after precuts.

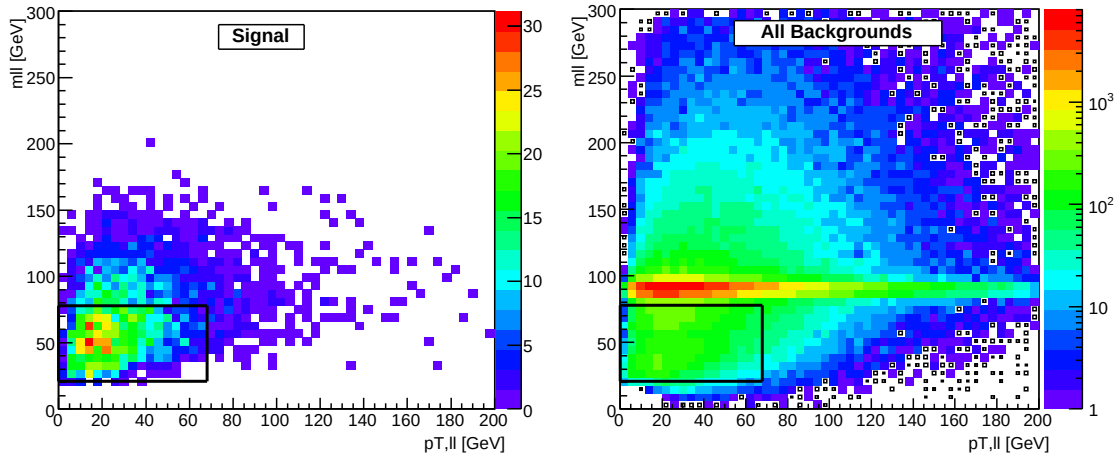

Figure 6.17: 2D Cut in the $\mu - \mu$ channel for m_A=200 GeV. ($\tan\beta$=20, L=30 fb^{-1}).

Cut	Signal	$t\bar{t}$	$Z \to \mu\mu$	$Z \to \tau\tau$	SUSY
Precuts	1074	36189	135679	4689	486
(21<$m_{\ell\ell}$<81) & (0<$p_{T,\ell\ell}$<64) GeV	649	11257	5197	4264	136
(0<$p_{T,b-jet}$<67) GeV	486	4625	4949	3617	36
(0<$p_{T,Higgs}$<67) GeV	406	1078	4838	3099	17
0.02<$x_1 \cdot x_2$<0.13	279	374	286	1085	3
(39<$m_{\ell\ell}$<78) GeV	224	299	240	257	2
(16<$p_{T,miss}$<95) GeV	208	287	88	194	2
ϵ resp. r [%]	19.4	99.2	99.9	95.9	99.6

Table 6.10: Number of events in the $\mu - \mu$ channel for m_A = 200 GeV, $\tan\beta$=20 and L=30 fb^{-1}.

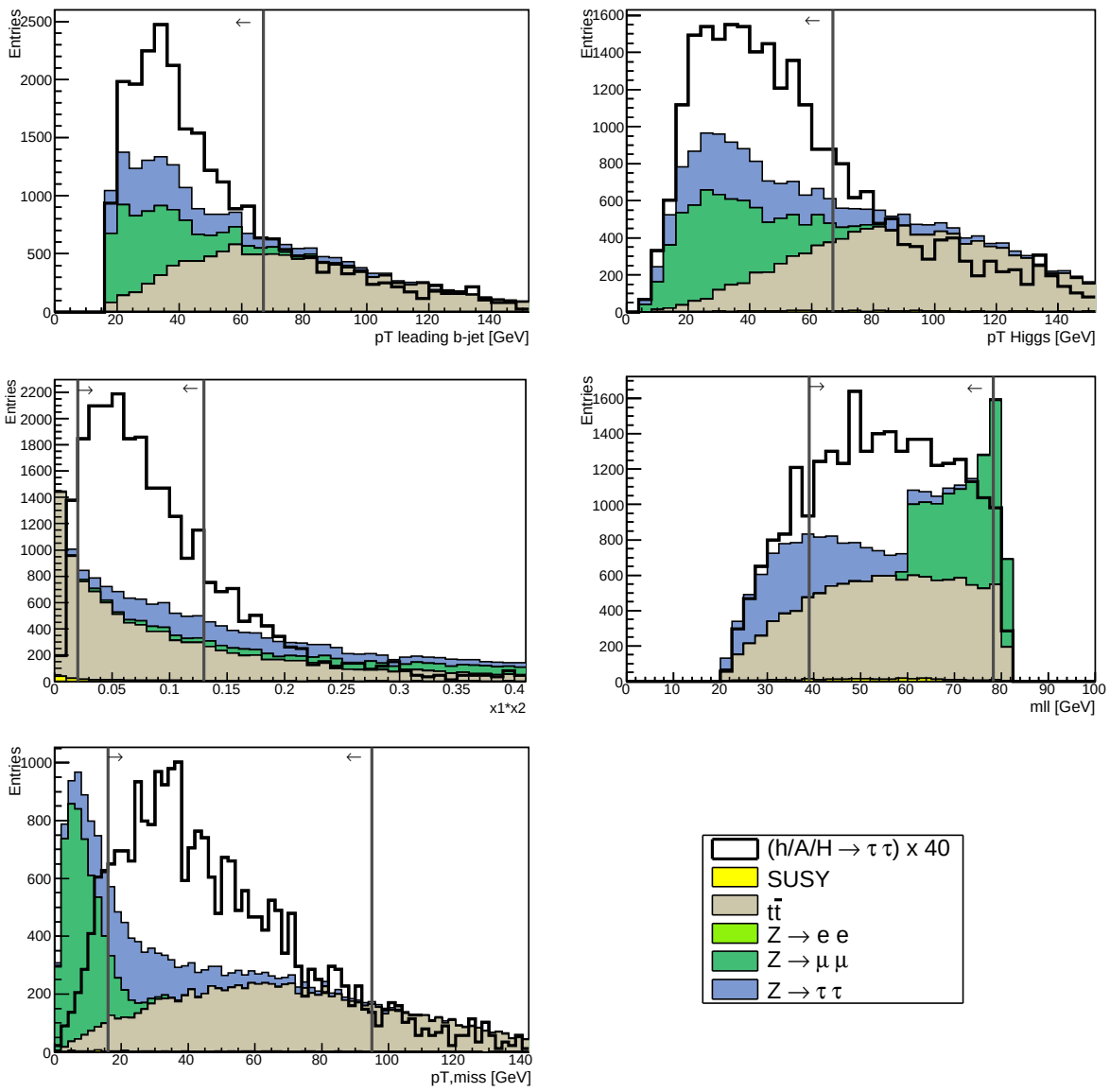

Figure 6.18: Distributions entering the cutanalysis for the $\mu - \mu$ channel (m_A=200 GeV, $\tan\beta$=20, L=30 fb^{-1}). The signal events are scaled for better visibility. Events kept in the analysis are indicated by arrows.

6.4.3 Cutflow in the e − μ channel

The five enumerated distributions are displayed in Figure 6.19. The absolute number of events are listed in Table 6.11. In this channel the statistical significance has been improved from a value of 7.4 after precuts to 16.7.

Cut	Signal	$t\bar{t}$	$Z \to ee$	$Z \to \mu\mu$	$Z \to \tau\tau$	SUSY
Precuts	2183	78169	135	745	7902	677
$(0<p_{T,b-jet}<44)$ GeV	1084	13455	42	127	4577	64
$(0<p_{T,Higgs}<43)$ GeV	664	755	26	60	2789	2
$0.05<x_1 \cdot x_2<0.4$	480	464	15	38	2106	1
$(60<m_{\ell\ell}<126)$ GeV	325	226	2	10	155	1
$(13<p_{T,miss}<75)$ GeV	287	197	0	8	95	0
ϵ resp. r [%]	13.1	99.7	100	98.9	98.8	100

Table 6.11: Number of events in the $e - \mu$ channel for m_A = 200 GeV, $\tan\beta$=20 and L=30 fb^{-1}.

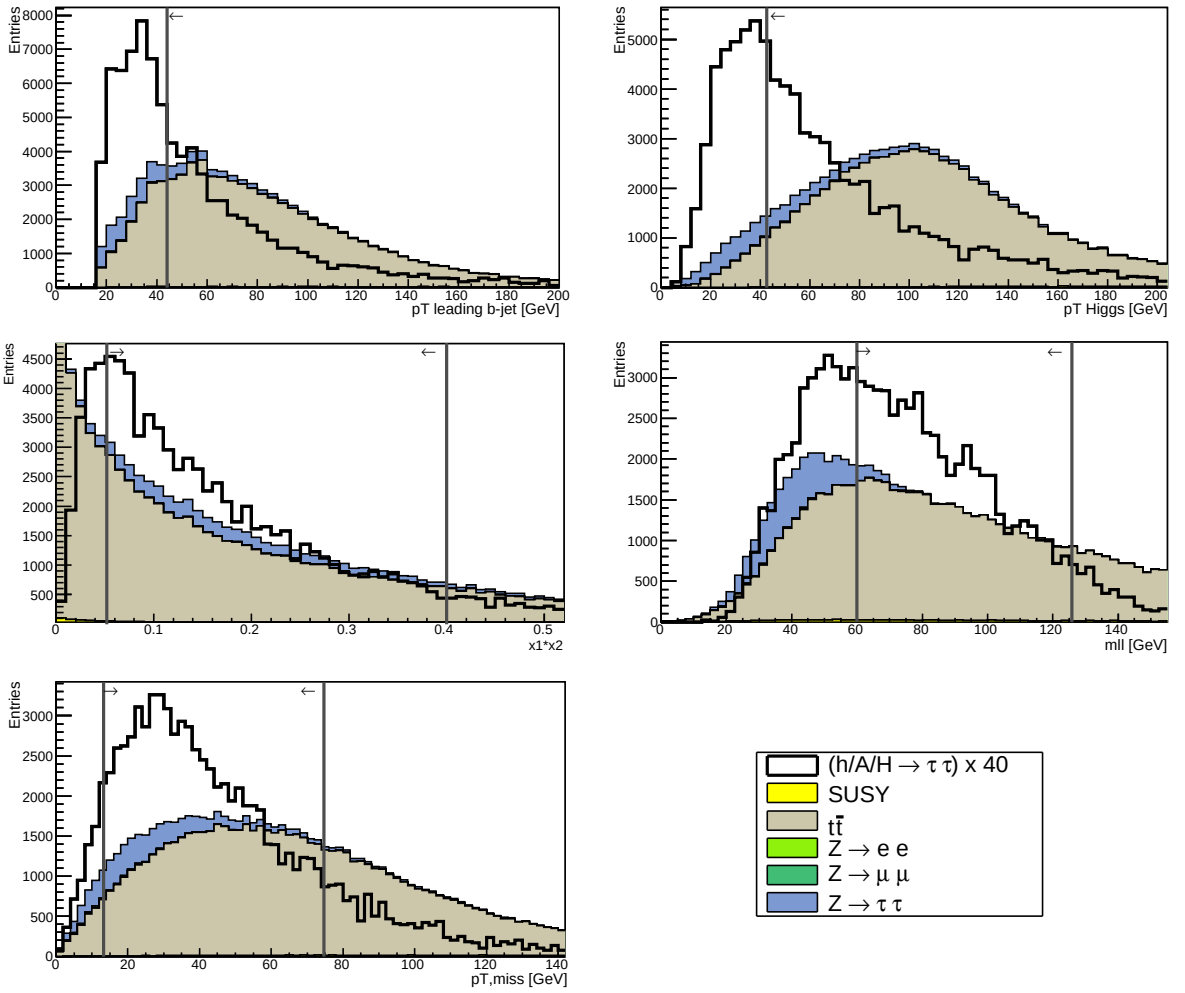

Figure 6.19: Distributions in the $e - \mu$ channel (m_A=200 GeV, $\tan\beta$=20, L=30 fb^{-1}). The signal events are scaled for better visibility. Events kept in the analysis are indicated by arrows.

6.4.4 Summary and Results for m_A=200 GeV

All optimized cutvalues are listed in Table 6.12.

Quantity		$e-e$		$\mu-\mu$		$e-\mu$	
2D $m_{\ell\ell}$	[GeV]	24	84	21	81		
2D $p_{T,\ell\ell}$	[GeV]	4	74	0	64		
$p_{T,b-jet}$	[GeV]	0	55	0	67	0	44
$p_{T,Higgs}$	[GeV]	0	62.7	0	67	0	42.7
$x_1 \cdot x_2$		0.02	0.156	0.02	0.13	0.05	0.4
$m_{\ell\ell}$	[GeV]	39.2	80	39	78.3	60	125.8
$p_{T,miss}$	[GeV]	20	200	16	95	13.3	74.7

Table 6.12: Cutvalues for m_A=200 GeV.

The result for $m_{\tau\tau}$ is shown in Figure 6.20. The remaining background is dominated by events from $t\bar{t}$ and $Z \rightarrow \tau\tau$. In the region around m_A=200 GeV there are also small contributions from $Z \rightarrow \ell\ell$. SUSY background has become negligible also for this Higgs mass hypotheses.

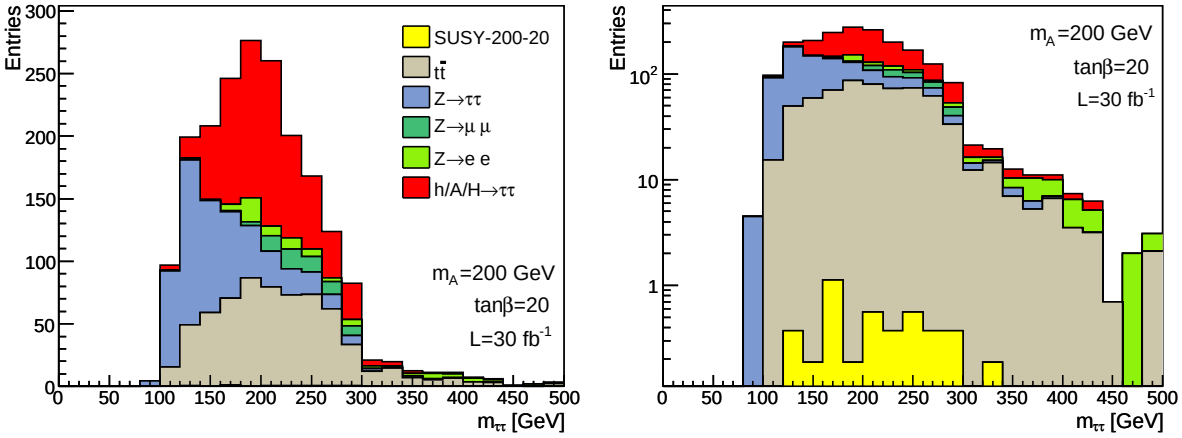

Figure 6.20: Final $m_{\tau\tau}$ spectrum after all cuts (m_A=200 GeV, tan β=20, L=30 fb^{-1}).

The significance at tan β=20 in the mass range $0 < m_A < 500$ GeV is calculated to:

$$\frac{S}{\sqrt{B}} = \frac{657}{\sqrt{1306}} = 18.22. \tag{6.5}$$

Due to the fact that the 200 GeV Higgs boson has the smallest cross section of all three optimized mass hypotheses, the smallest value of the significance is expected.

6.5 Sliding Mass Window

A sliding mass window is applied on the remaining mass distributions to get the maximum of the significance depending on the range wherein the events get counted. The range of the window is $m_A \pm \Delta m$ with $0 < m_A < 500\ GeV$. The range is chosen individually for each mass hypotheses according to the invariant mass resolution. Events inside the window are counted to obtain the value of $\frac{S}{\sqrt{B}}$. The number of signal events is then given as follows:

$$S = \sum_{bins\ in\ m_A-\Delta m}^{bins\ in\ m_A+\Delta m} Number\ of\ events\ per\ bin \tag{6.6}$$

The background events are counted accordingly.
It is assumed that a Gaussian distribution describes the signal $m_{\tau\tau}$ shape approximately. Figure 6.21 shows the signal $m_{\tau\tau}$ events after having applied the optimized cuts, fitted with a Gaussian.

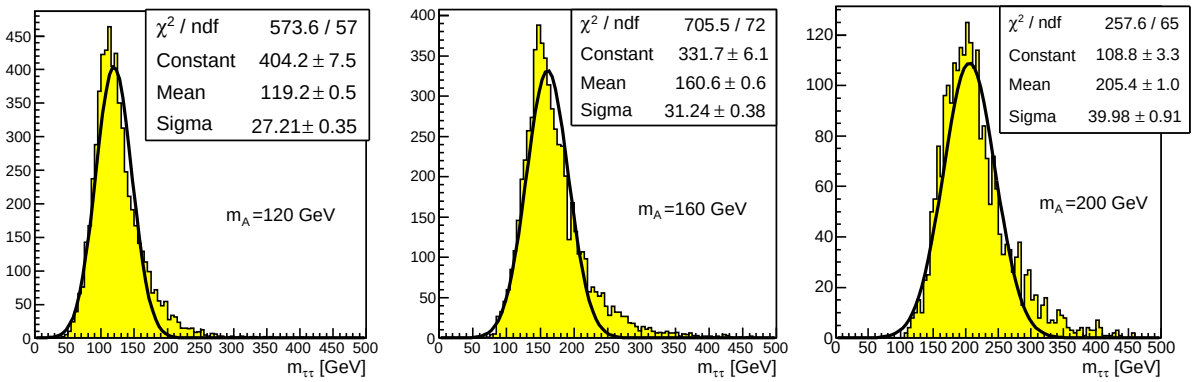

Figure 6.21: Signal $m_{\tau\tau}$ shape after cut optimization fitted with Gaussian. The differences of the fit values to the values in chapter 5 are due to correlations of the cut variables to the $m_{\tau\tau}$ resolution. In addition, here the full $m_{\tau\tau}$ shape has been fitted with a Gaussian, not only the central part.

The σ for each mass hypotheses is taken from 6.21. The range chosen for the sliding mass window is $1.65 \cdot \sigma < m < 2.0 \cdot \sigma$. The asymmetric range is chosen to take the high energy tail into account.
Especially for $m_A = 160$ GeV the sliding window leads to a further improvement of the significance. Here the maximum value of $\frac{S}{\sqrt{B}}$ is 44, which is much higher than 33 (Equation 6.4). The reason for this is that the background shape is not flat but increases for $m_A \to m_Z$ and the window cuts away events from $Z \to \tau\tau$.
The trend for an increasing value of m_A is that the combined significance is not much better than the significance in the $e - \mu$ channel. The reason for this is that for $m_A \geq 200$ GeV the mean invariant lepton-lepton mass of the Higgs events comes close to values around 90 GeV (Figure 5.14), where the dominant $Z \to \ell\ell$ background peaks. So reducing $Z \to \ell\ell$ by a cut on $m_{\ell\ell}$ also strongly reduces the number of signal events. As a conclusion an optimization for Higgs particles heavier than 200 GeV might be reduced to the mixed channel. This would simplify the analysis while obtaining similar results.

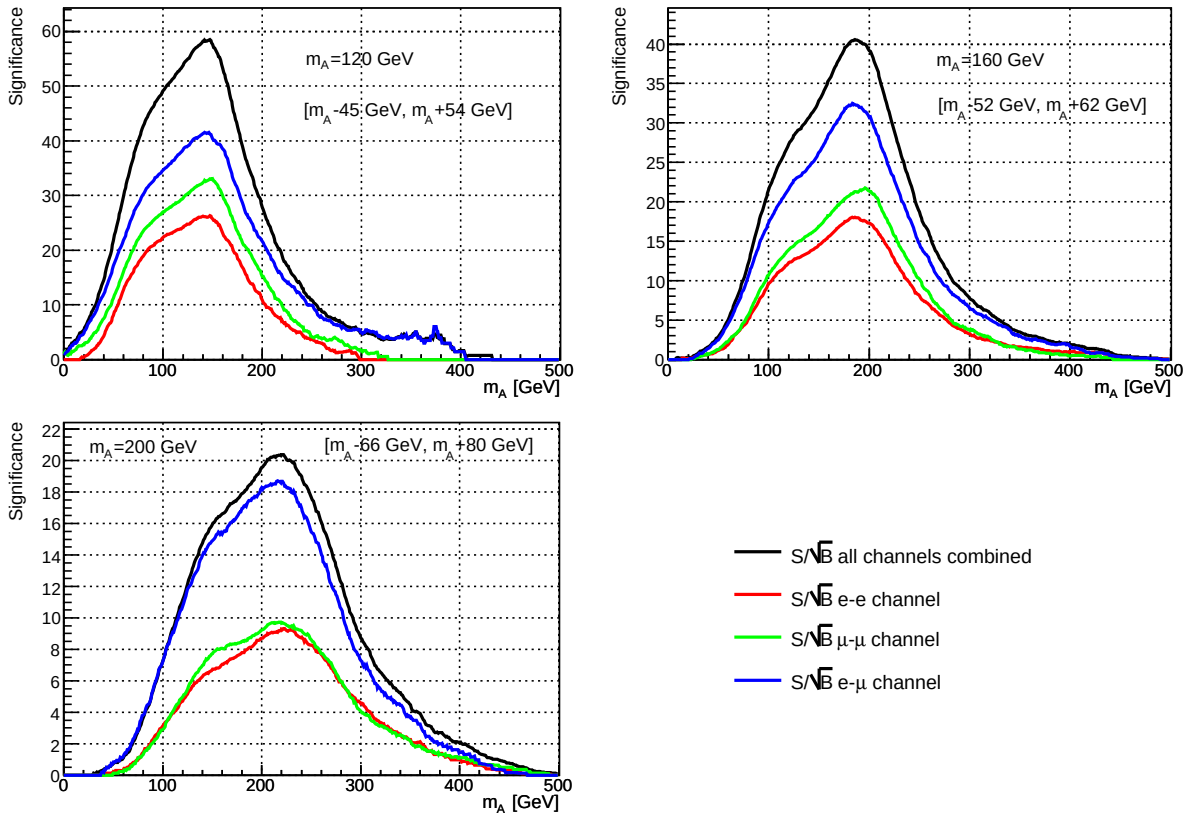

Figure 6.22: Significance for the three Higgs mass hypotheses obtained by sliding a mass window over $m_{\tau\tau}$. The window has a mass dependent size of $m_A - 1.65\,\sigma < m_A < m_A + 2.0\,\sigma$, where σ is the Gaussian width, obtained from Figure 6.21. ($\tan\beta = 20,\ L = 30\ \mathrm{fb}^{-1}$)

6.6 Combined Results in the $\mathbf{m_h^{max}}$-Scenario

With the optimized results for the three Higgs mass hypotheses at $\tan\beta$=20 a scan of the statistical significance in the m_A-$\tan\beta$ plane can be performed. This can be used to find limits on a discovery in the $\mathrm{m_h^{max}}$scenario. Usually a discovery is claimed if $\frac{S}{\sqrt{B}} \geq 5$.
To extrapolate the significance as function of $\tan\beta$ it is not necessary to make further optimizations. The background cross section is independent from $\tan\beta$, because SUSY background turned out to be negligible. As described in Chapter 4, the signal cross section increases with $\tan^2\beta$. Therefore, the number of signal events also depends on $\tan^2\beta$.
The number of signal events N for example for $\tan\beta$=10 - at a given value of m_A and a constant integrated luminosity L - is given as follows:

$$L = \frac{N_{m_A,\tan\beta=20}}{(\sigma \times BR)_{m_A,\tan\beta=20}} = \frac{N_{m_A,\tan\beta=10}}{(\sigma \times BR)_{m_A,\tan\beta=10}} \tag{6.7}$$

$$N_{m_A,\tan\beta=10} = N_{m_A,\tan\beta=20} \cdot \frac{(\sigma \times BR)_{m_A,\tan\beta=10}}{(\sigma \times BR)_{m_A,\tan\beta=20}} \tag{6.8}$$

The significance can be scaled accordingly:

$$\left(\frac{S}{\sqrt{B}}\right)_{\tan\beta=10} = \left(\frac{S}{\sqrt{B}}\right)_{\tan\beta=20} \cdot \frac{\sum_{\substack{degenerate\\bosons}} (\sigma_{b\bar{b}\,\Phi} \times BR_{\Phi\to\tau\tau})_{\tan\beta=10}}{\sum_{\substack{degenerate\\bosons}} (\sigma_{b\bar{b}\,\Phi} \times BR_{\Phi\to\tau\tau})_{\tan\beta=20}} \tag{6.9}$$

The initial values of the significance at $\tan\beta$=20 are taken from the results of the sliding mass window displayed in Figure 6.22.
The scaled significance as function of $\tan\beta$ for all three optimized mass hypotheses is shown in Figure 6.23. The left plot reflects the quadratic dependency of the cross section on $\tan\beta$. In the right plots an interpolation of the optimized and $\tan\beta$ dependent significance in the $m_A - \tan\beta$ plane and the discovery contour are displayed.
A Higgs boson with a mass of 120 GeV can be discovered using the described cut-and-count method if $\tan\beta$>6. A 160 GeV Higgs particle can be discovered for values of $\tan\beta$>7. A 200 GeV Higgs boson might be discovered if $\tan\beta$>10 is realized in nature.
If systematic uncertainties are considered, the significance will decrease and the discovery contour will shift to higher values of $\tan\beta$ (Chapter 8).

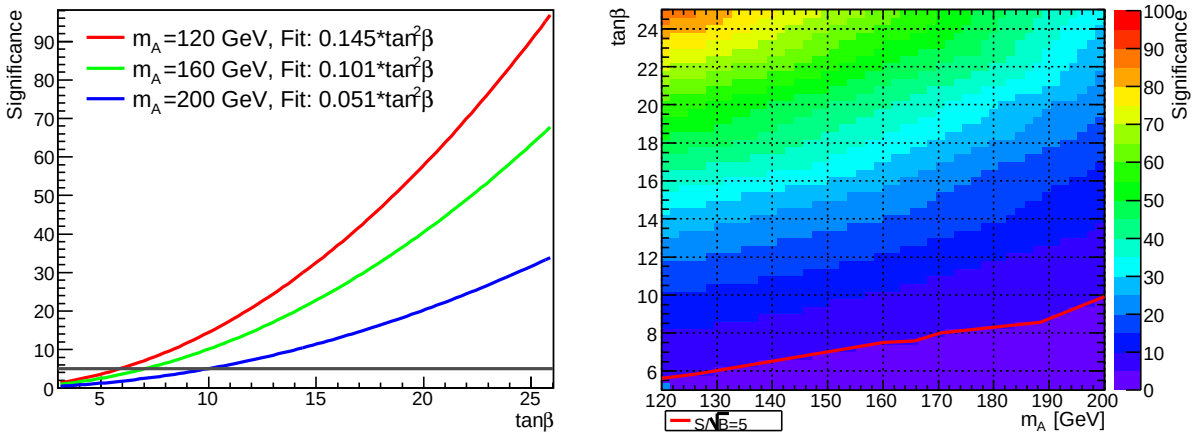

Figure 6.23: Extrapolation of the significance as function of $\tan\beta$ (left). The significance shows a quadratic dependency and was fitted with a quadratic function for m_A=120 GeV, m_A=160 GeV and m_A=200 GeV. The right plot shows an interpolation of the significance of the three optimized Higgs hypotheses in the mass range of 120 $GeV < m_A < 200\ GeV$. The interpolation was calculated by ROOT [60] which uses the Delaunay triangles method. The $\frac{S}{\sqrt{B}} = 5$ contour is marked red.

Chapter 7

Fit Approach

7.1 Motivation and Method

So far this analysis has been a cut-and-count study. Other methods might be used to exploit more information, especially from data. One possible approach is to fit the invariant $\tau\tau$ mass spectrum with a suitable lineshape for signal and background to separate them and to extract for example the Higgs mass. The shape and normalization of the background could be extracted from data and therefore the analysis would not be affected by the uncertainty on the cross section of the background process. The large $m_{\tau\tau}$ resolution due to the collinear approximation however complicates a fit.
In the following an approach is discussed to test the feasibility of a fit with an analytic function. This study is preliminary and its goal is only to assess the feasibility of this method.
For the fit not the full MC samples but smaller samples corresponding to an integrated luminosity of 30 fb^{-1} have been used to reproduce a realistic expectation of event numbers and distributions after 3 years of LHC running.
The cutanalysis shows that the signal shape does not form a sharp peak, due to the collinear approximation. But due to the huge cross sections at high values of $\tan\beta$, the huge number of events form a detectable signal peak on top of the smooth background shape.
In order to get a suitable $m_{\tau\tau}$ shape for a fit approach, softer cuts have to be applied fulfilling the following requirements:

- Mass independent
  The goal of the fit will be to extract the Higgs mass as one of the fitted parameters, therefore no mass dependent cuts must be applied.

- Keeping events which form the Z^0 peak
  Enough events from the $Z \rightarrow \tau\tau$ background process should be kept in order to allow for a precise determination of the background shape and the normalization in the fit. The Z^0 mass is a well known parameter and can be used as an input to the fit. Furthermore, the events from the Higgs decay are supposed to 'sit' on the mass energy tail of the Z peak and form an observable peak.

- High signal efficiency

In order to keep enough signal events the efficiency must not be too low for the considered Higgs masses in the range between 120 GeV and 200 GeV.

A series of tests has been performed to find a suitable set of cuts complying all of the listed criteria in all three sub channels. The chosen cutvalues are listed in Table 7.1. A comparison of the signal efficiency after the fit cuts and the optimized cuts (chapter 6) is displayed in Figure 7.1. The resulting fitted $m_{\tau\tau}$ shape without a Higgs signal is displayed in Figure 7.2. The fit parameters are listed in Table 7.2.

Quantity		$e-e$ channel	$\mu-\mu$ channel	$e-\mu$ channel
$p_{T,b-jet}$	[GeV]	$0\ldots53$	$0\ldots53$	$0\ldots53$
$p_{T,Higgs}$	[GeV]	$0\ldots60$	$0\ldots60$	$0\ldots60$
$m_{\ell\ell}$	[GeV]	$0\ldots60$	$0\ldots80$	$0\ldots158$
$p_{T,miss}$	[GeV]	$14\ldots80$	$20\ldots80$	$0\ldots80$

Table 7.1: Higgs mass independent cuts as preparation for the fit.

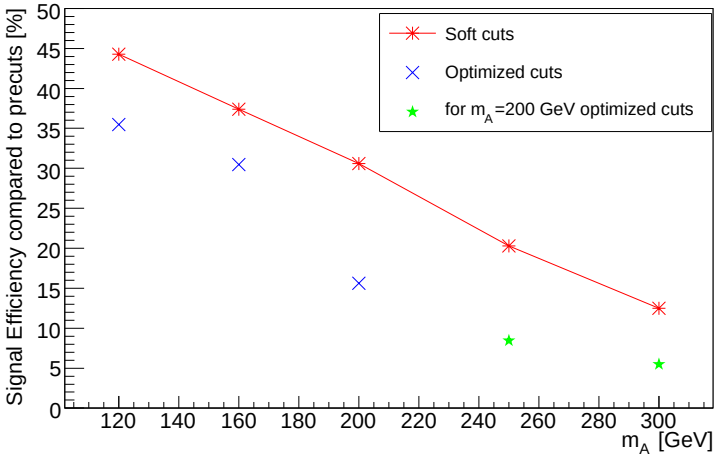

Figure 7.1: Comparison of signal efficiencies after soft cuts (red) and optimized cuts (blue). Since no optimization was performed for m_A=250 GeV and m_A=300 GeV the green markers show the signal efficiencies after having applied the optimized cuts for m_A=200 GeV.

This shape is dominated by $Z \rightarrow \tau\tau$ events and is fitted with a Crystal Ball function [61; 62; 63]:

$$f_{BG}(m) = \begin{cases} A \cdot e^{\left(-\frac{1}{2}\cdot\left(\frac{m-m_0}{\Delta m}\right)^n\right)} & m < m_0 + a\cdot\Delta m \\ A \cdot \frac{e^{\left(-\frac{1}{2}\cdot a^2\right)}\cdot\left(\frac{n}{a}\right)^n}{\left(\frac{m-m_0}{\Delta m}+\frac{n}{a}-a\right)^n} & m > m_0 + a\cdot\Delta m \end{cases} . \tag{7.1}$$

A, m_0, Δm and n are free parameters.
A Crystal Ball function is a Gaussian with a 'power' tail in this case at high masses. A gives the normalization of the background, m_0 is equal to the Z^0 mass, Δm is the width of the Gaussian describing the Z. The tail is described with a $\frac{1}{(m-m_0)^n}$ function attached to the Gaussian in the point $m = m_0 + a\cdot\Delta m$. n is an exponent describing the steepness of the tail.

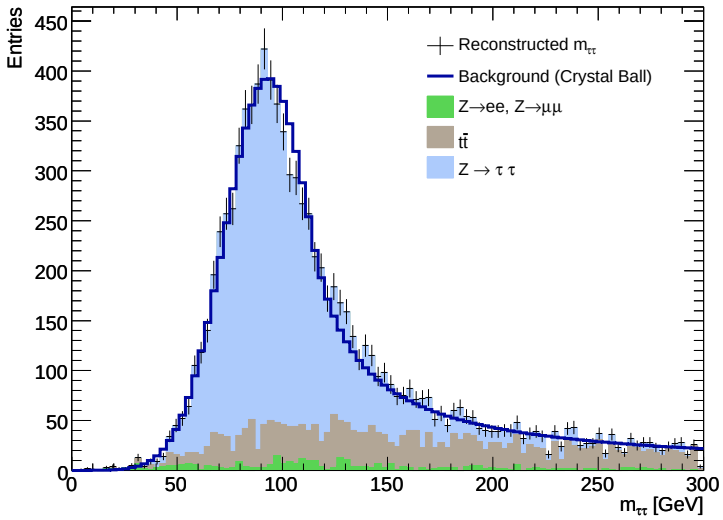

Figure 7.2: Fitted background shape without a Higgs hypotheses. The fitted parameters and the minimal χ^2 are listed in Table 7.2 in the column labeled 'background'.

The power tail is divergent and a natural choice is to set the point of divergence $m = m_0$ equal to m_0, leading to the condition [64]:

$$a = \sqrt{n}. \tag{7.2}$$

This also reduces the number of free parameters and leads to the following form of the Crystal Ball function:

$$f_{BG}(m) = \begin{cases} A \cdot e^{\left(-\frac{1}{2}\cdot\left(\frac{m-m_0}{\Delta m}\right)^2\right)} & m < m_0 + \sqrt{n}\cdot\Delta m \\ \frac{A}{\left(\sqrt{\frac{e}{n}}\cdot\frac{m-m_0}{\Delta m}\right)^n} & m > m_0 + \sqrt{n}\cdot\Delta m \end{cases}. \tag{7.3}$$

Using the Crystal Ball function the Z^0 shape can be described. The $t\bar{t}$ shape is not explicitly described with a term of its own; still the plot 7.2 indicates that indeed the function used can describe the shape of the total background. The fit parameters are listed in Table 7.2. Contributions to the background from SUSY particles are excluded because it became obvious that they are negligible.
The signal shape is approximately described by a Gaussian. The signal properties obtained by a fit with a Gaussian after having applied the soft cuts are displayed in Figure 7.3.
The Gaussian describing the signal f_{Higgs} has three parameters: Normalization, Higgs mass and Higgs width. It is added to the Crystal Ball function to form the complete fit function:

$$f_{Fit} = f_{BG} + f_{Higgs}, \tag{7.4}$$

which has then seven free parameters in total.
The fit is has been done using the MINUIT package [65]. It is a binned fit, minimizing the χ^2 by varying the parameters. The χ^2 is given as follows:

$$\chi^2 = \sum_{bins} \frac{(f_{Fit} - y)^2}{y}. \tag{7.5}$$

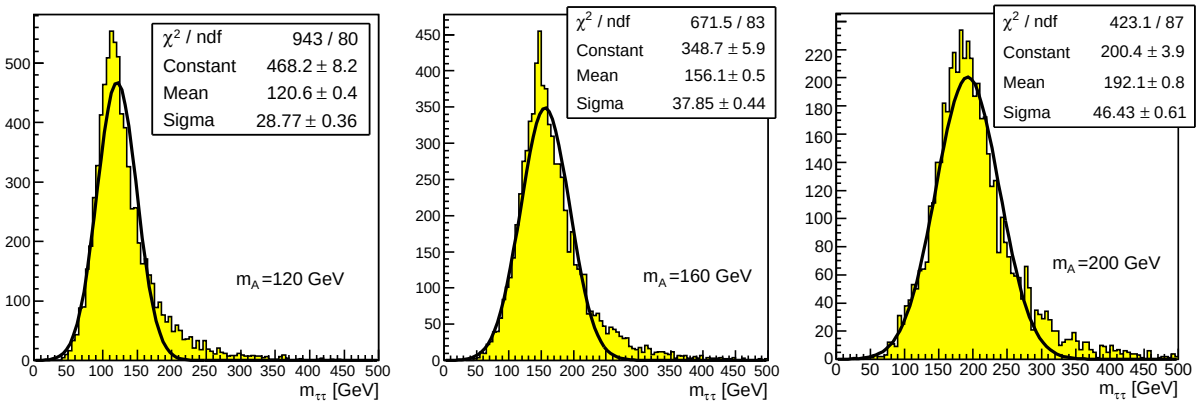

Figure 7.3: Invariant $\tau\tau$ mass for three Higgs mass hypotheses fitted with a Gaussian after having applied the soft cuts.

f_{Fit} is the fit function, y is the number of events observed in each bin in $m_{\tau\tau}$ The best minimal achievable value for χ^2 is zero. If the hypothesis is true, the average value of χ^2 is equal to he number of degrees of freedom (ndf). ndf is equal to the number of bins minus the number of parameters.

7.2 Fit Results

In the following three fit examples are shown in Figures 7.4-7.6 below. The corresponding fit values are given in Table 7.2. The results are discussed in Section 7.3.
From the fit the significance can be obtained by the following equation:

$$\left(\frac{S}{\sqrt{B}}\right)_{Fit} = \frac{\int f_{Higgs}(m)\,dm}{\sqrt{\int f_{BG}(m)\,dm}}. \tag{7.6}$$

The integration range is equal to the mass range displayed in the fit figures.

Parameter/Fit	Background	m_A=120 GeV	m_A=160 GeV	m_A=200 GeV
χ^2/ndf	154/96	189/94	194/97	148/93
Normalization A	393 ± 7	376 ± 51	393 fixed	498 ± 9
σ_Z [GeV]	20.6 ± 0.4	18.3 ± 0.5	20.6 fixed	19.3 ± 0.4
Exponent n	1.04 ± 0.02	0.83 ± 0.08	1.04 fixed	1.16 ± 0.03
m_Z [GeV]	93.3 ± 0.4	93.3 fixed	93.3 fixed	91.8 ± 0.5
Higgs normalization	-	16447 ± 2704	9741 ± 312	1677 ± 604
σ_A [GeV]	-	28.4 ± 1.0	36.7 ± 1.4	56.9 ± 1.3
m_A [GeV]	-	116 ± 4	152 ± 2	178 ± 2
Connection	114.3	107.8	114.3	112.5
$\left(\frac{S}{\sqrt{B}}\right)_{Fit}$	-	57.5	33.6	49
$\left(\frac{S}{\sqrt{B}}\right)_{count}$	-	54.7	33.5	29.3

Table 7.2: Fit parameters. The corresponding figures are 7.2-7.6. The fitted parameters of the Gaussian describing the Higgs can be compared to the parameters given in Figure 7.3. The connection point of the Gaussian to the Crystal ball function $m_Z + \sqrt{n} \cdot \sigma_Z$ and the significance of each example is also given. The 200 GeV column shows the largest discrepancy between the significance obtained in a cut and count analysis and the significance obtained in the fit. The value of the fitted Z mass is not equal to the true Z mass due to the applied cuts.

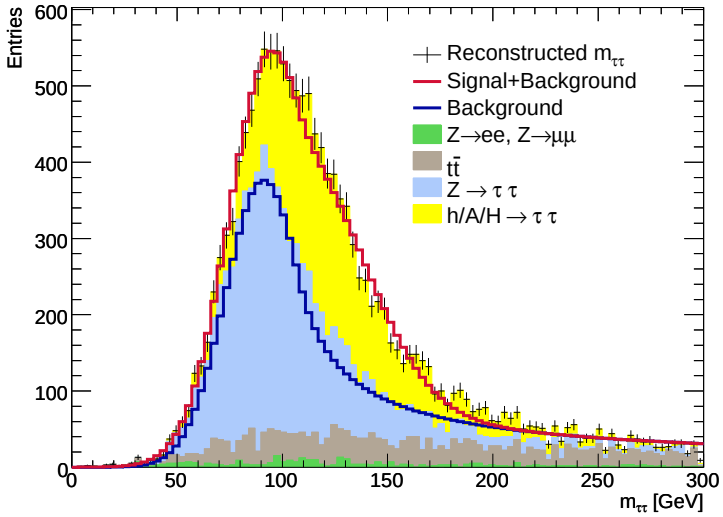

Figure 7.4: Fit of background and signal for a 120 GeV Higgs mass hypotheses. The mass of the Z^0 is fixed in this fit; all other parameters float. The values obtained from the fit are listed in Table 7.2. $\tan\beta$ is 20, the integrated luminosity is 30 fb^{-1}. A floating value of the Z mass could not reproduce the correct signal and background fractions.

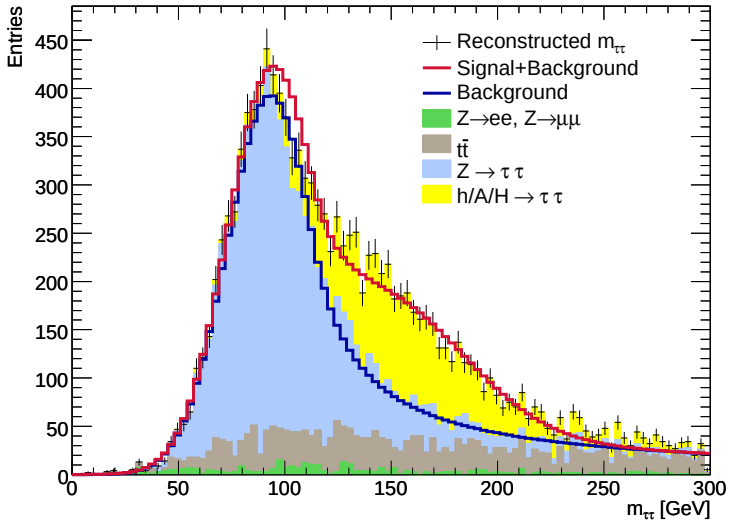

Figure 7.5: Fit of background and signal for m_A=160 GeV, $\tan\beta$=20, normalized to $L = 30\text{fb}^{-1}$. The four background fit parameters are fixed and taken from the fit to the background shape only. The parameters for the Gaussian describing the signal are floated in the fit. Their values are listed in Table 7.2. Not fixing background parameters would lead to a wrong Higgs mass of about 135 GeV.

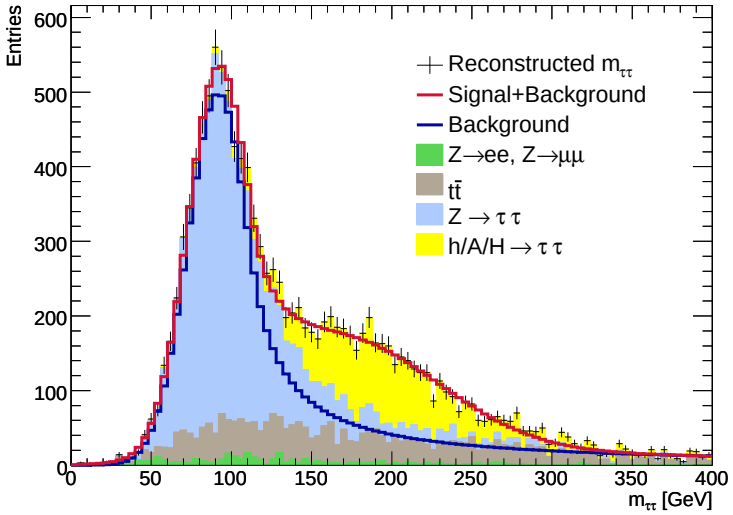

Figure 7.6: Fitted $m_{\tau\tau}$ shape with a 200 GeV Higgs mass hypotheses and $\tan\beta$=30, normalized to $L = 30\text{fb}^{-1}$. All seven fit parameters are floated and their values are listed in Table 7.2. Due to the huge amount of signal events and the fact, that the signal events are not close to the Z^0 peak, a fit with all parameters floating is working. Yet, the obtained significance from the fit is too high. The background is under-estimated by 15 %, while the signal is over-estimated by 30 %, leading to a 40 % higher significance compared to the cut-and-count method.

7.3 Conclusions

The signal events form a detectable peak, yet the fit parameters do not well agree with the expectation. Obtaining the Higgs mass from the discussed fits leads to values which are about 10 GeV too low. Only for some points in the $m_A - \tan\beta$ plane a fit with free parameters converges and leads to acceptable results. High values of $\tan\beta$ lead to more signal events and therefore a better distinction from the background. Signal events for values of m_A close to the Z mass enlarge the Z peak. They form no peak of their own, but a measurable discrepancy from the expectation for a background-only hypothesis, if $m_A \neq m_Z$. The uncertainty on the Z cross section is the reason why the normalization of the Crystal Ball function can not be fixed. The example for $m_A = 160$ GeV pointed out that this mass range is very hard to fit if the background parameter values are not fixed. The main uncertainty in this fit is the shape of the signal. Especially the high energy tail is not consistent with a Gaussian. It has been tested, whether the signal shape could also be described with a Crystal Ball function, but it became clear that this way the $t\bar{t}$ shape is absorbed in the signal, leading to higher values of $\frac{S}{\sqrt{B}}$ than a cut-and-count analysis shows.
A solution would be to include the $t\bar{t}$ shape in the analytical function and to obtain its normalization at high masses where they are the dominant contribution the total background. Therefore it could also help to refine the choice of cuts.
Another possible method is to study effects that would improve the $m_{\tau\tau}$ resolution of the signal. This will of course also affect the resolution of the $Z \to \tau\tau$ mass. One way to do this would be to cut harder on $\Delta\Phi_{\ell\ell}$ (as discussed in section 5.3) or on the p_T of the Higgs candidate. But this will reduce the number of signal events significantly and low statistic will not lead to a converging fit.

Chapter 8

Discussion of Uncertainties

8.1 Idea

The described cut-and-count analysis of Chapter 6 cannot be applied to data if the used Monte Carlo description may differ from experimentally gained data. Furthermore, systematic uncertainties have not been taken into account so far. The significance of a discovery depends on the statistical, systematic and theoretical uncertainties of the number of signal and background events. Main contributions are given by the uncertainties on cross sections and identification efficiencies. For this analysis the b-tagging, electron and muon identification are crucial.
In the following a method is described how these factors can be considered. The idea is to develop a method to obtain the number of and the uncertainty on $Z \to \tau\tau \to \ell\ell + 4\nu$ events from data. This is still under investigation, some preliminary but promising results will be shown below. The method will be applied for the 120 GeV Higgs mass hypotheses, because after applying the optimized cuts $Z \to \tau\tau$ events are the dominating contribution to the background.
First, a control sample will be constructed which contains mostly $Z \to \ell\ell$ events. This control sample will be called region B. Region A covers the signal region where mostly Higgs events and $Z \to \tau\tau$ events are gathered. Next, the full MC data sample will be split into two sub-samples: One will be called 'MC' and the other 'Data'. In Table 8.1 the 'new' samples are listed.

Process	Monte Carlo	'Data'
$Z \to \tau\tau$	17.6 M (77.2 fb^{-1})	2.28 M (10 fb^{-1})
$Z \to \mu\mu$	35.3 M (20 fb^{-1})	17.6 M (10 fb^{-1})
$Z \to ee$	35.3 M (20 fb^{-1})	17.6 M (10 fb^{-1})

Table 8.1: Split MC samples. The size of the 'data' samples is chosen to be enough for an integrated luminosity of 10 fb^{-1}, because for $Z \to \ell\ell$ events no more than overall $L = 30\,\text{fb}^{-1}$ was available. The MC events will be scaled to $L = 10\,\text{fb}^{-1}$.

The number of $Z \to \tau\tau \to 2e + 4\nu$ events in the data sample in region A can be obtained by the following equation:

$$(Z \to \tau\tau \to 2e + 4\nu)^A_{Data} = \frac{(Z \to ee)^B_{Data}}{(Z \to ee)^B_{MC}} \cdot (Z \to \tau\tau \to 2e + 4\nu)^A_{MC}\,. \tag{8.1}$$

This is perfectly valid if the following two conditions are fulfilled:

- $$\frac{(Z \to ee)^B_{Data}}{(Z \to ee)^B_{MC}} = \frac{(Z \to \tau\tau \to 2e + 4\nu)^B_{Data}}{(Z \to \tau\tau \to 2e + 4\nu)^B_{MC}}. \tag{8.2}$$

  This is valid if $Z \to ee$ events behave like $Z \to \tau\tau \to ee + 4\nu$ events.

- $$\frac{(Z \to ee)^B_{Data}}{(Z \to ee)^B_{MC}} = \frac{(Z \to \tau\tau \to 2e + 4\nu)^A_{Data}}{(Z \to \tau\tau \to 2e + 4\nu)^A_{MC}}. \tag{8.3}$$

  This is fulfilled if $Z \to \tau\tau \to e + 4\nu$ events in region B behave like $Z \to \tau\tau \to e + 4\nu$ events in region A.

In the ratio $\frac{(Z\to ee)^B_{Data}}{(Z\to ee)^B_{MC}}$ systematic uncertainties from b-tagging efficiencies, lepton identification and light jet rejection are included. The ratio can be determined with high statistic in the sideband B and it is independent from the signal. One is independent on uncertainties of the luminosity, too. This scaling can be adapted to $Z \to \tau\tau \to 2\mu + 4\nu$ events accordingly. For the mixed channel $Z \to \tau\tau \to e\mu + 4\nu$ the geometric mean of both channels is used.

8.2 Construction of the Control Sample

The aim is to construct a control sample where mostly events from $Z \to \ell\ell$ decays are gathered (sideband region). Distributions of important kinetic variables of both regions however should look similar, which must be validated.
For region A the precuts and the optimized cuts for a 120 GeV Higgs mass are applied (Table 6.4). The cuts for region B, the control sample, are listed in Table 8.2. The precuts

Quantity	Region A		Region B	
	$e-e$	$\mu-\mu$	$e-e$	$\mu-\mu$
$m_{\ell\ell}$ [GeV]	26.7 ... 60	27.5 ... 60	75 ... 100	75 ... 100
$p_{T,\ell\ell}$ [GeV]	0 ... 42	0 ... 44	0 ... 42	0 ... 44
$\Delta\Phi_{\ell\ell}$	0 ... $\pi - 0.1$		0 ... π	
x_1, x_2	0 ... 1		$-\infty$ ... ∞	
$p_{T,b-jet}$ [GeV]	0 ... 64		0 ... 64	
$p_{T,Higgs}$ [GeV]	5 ... 67	5 ... 68	5 ... 67	5 ... 68
$x_1 \cdot x_2$	0.04 ... 0.28	0.03 ... 0.34	$-\infty$ ... ∞	
$p_{T,miss}$ [GeV]	12 ... 61	11 ... 60	12 ... 61	11 ... 60

Table 8.2: Different cuts for region A and region B. To both regions the same trigger conditions are applied, two leptons with opposite charges are selected and at least one b-tag is required.

have been modified for the control sample to be as general as possible. The cut on $m_{\ell\ell}$ in the region B leads to an enrichment of the control sample with $Z \to \ell\ell$ by covering values around 90 GeV. In Figure 8.1 a plot of $m_{\ell\ell}$ vs. $p_{T,\ell\ell}$ with the borders of the two regions after applying the cuts is displayed. The $m_{\tau\tau}$ shapes for both regions for the $e-e$

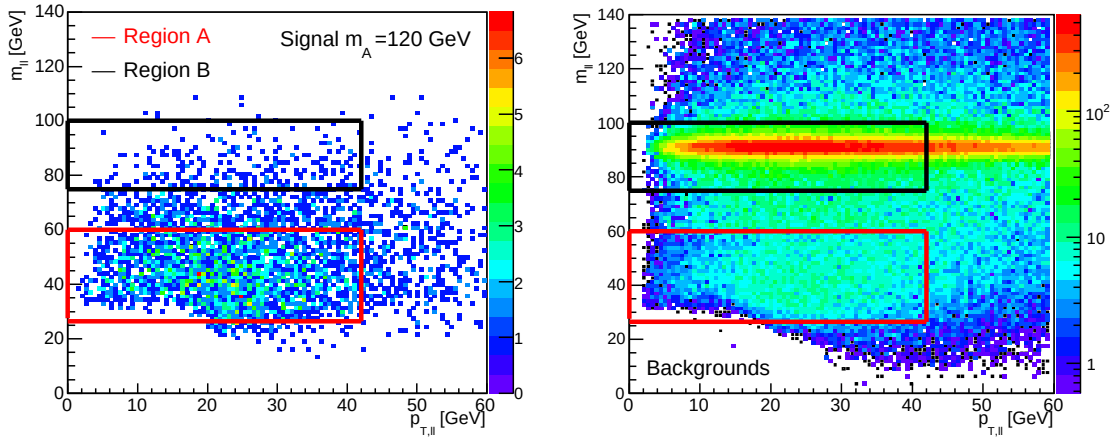

Figure 8.1: Signalregion (marked by a red rectangle, region A) and controlregion (black rectangle, region B) in the $m_{\ell\ell} - p_{T,\ell\ell}$ plane. In the left picture are the signal events and in the right one are the background events in the $e - e$ channel displayed.

and $\mu - \mu$ channels are displayed in figure 8.2. In the right plot a non-physical double peak structure of the invariant mass is visible. This is a consequence because the mass is reconstructed using the collinear approximation although there are no neutrinos involved in $Z \to \ell\ell$ events. It is also obvious that the control sample is dominated by $Z \to \ell\ell$ events. Exact numbers of events from the different processes are given in Table 8.3.

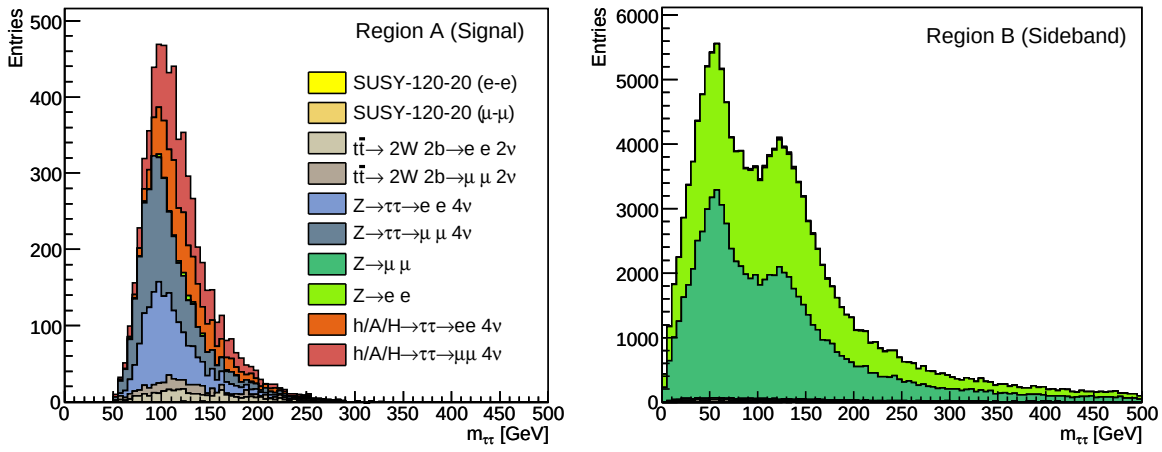

Figure 8.2: Invariant $\tau\tau$ mass in region A (left) and region B (right), broken down to $e - e$ and $\mu - \mu$ channel. The value of $\tan\beta$ is 20, $L = 30\,\mathrm{fb}^{-1}$. The non-physical mass distribution in the control sample is a consequence of the modified precuts. The mass is being reconstructed without cutting on the physical region of x_1 and x_2. The region A is dominated by $Z \to \tau\tau$ and signal events, the sideband region is filled with events from $Z \to \ell\ell$ decays.

Since the contamination of the control sample with events different from $Z \to \ell\ell$ decays is so small (below 5 %), as from now on all other processes in region B will be neglected, to simplify the feasibility study of this method.

	Region A		Region B	
Process	$e-e$	$\mu-\mu$	$e-e$	$\mu-\mu$
all	2 750	3 538	73 716	79 882
$Z \to \tau\tau$	50.0 %	52 %	0.13 %	0.03 %
$Z \to e\,e$	1.2 %	0 %	97.4 %	0 %
$Z \to \mu\mu$	0 %	0.2 %	0 %	98.6 %
$t\bar{t}$	11.4 %	7.8 %	1.9 %	1.1 %
SUSY	0.07 %	0.07 %	0.01 %	0.01 %
Signal	37.3 %	39.7 %	0.6 %	0.3 %

Table 8.3: Fraction of number of events in the regions A and B, broken down to $e-e$ and $\mu-\mu$ channel. The in row 'all' given absolute number of events is normalized to $L = 30\,\text{fb}^{-1}$, obtained in the mass range of Figure 8.2 ($0<m_A<500$ GeV).

8.3 Validation of the Control Sample

In the following it is tested how well the control sample reflects the behavior of events in the signal region (A). The comparison is made between the $Z \to \ell\ell$ events in the control sample and the $Z \to \tau\tau$ events from region A, both for the full MC statistic without splitting the MC data.
A first test is the comparison of the b-tagging efficiencies. In table 8.4 is listed, how many b-tagged jets truly originate from b-jets.

	$e-e$ channel	$\mu-\mu$ channel
$Z \to \tau\tau$ for Region A	51 %	50 %
$Z \to \ell\ell$ for Region B	53 %	51 %

Table 8.4: b-tagging efficiency in region A and B broken down to $e-e$ and $\mu-\mu$ channel. The numbers are very similar.

The p_T of the leading b-jet in region A and region B is displayed in Figure 8.3. The discontinuities at 35 GeV and 50 GeV are due to the energy calibration by ATLFast-B (as discussed in Chapter 5). The distribution of p_T of the leading lepton and the sub-leading lepton is compared in Figures 8.4 and 8.5, respectively. As expected, the distributions show differences between region A and region B. The lepton p_T from $Z \to \ell\ell$ events peak at values around 45 GeV, the events from $Z \to \tau\tau$ decays peak at lower values of p_T.

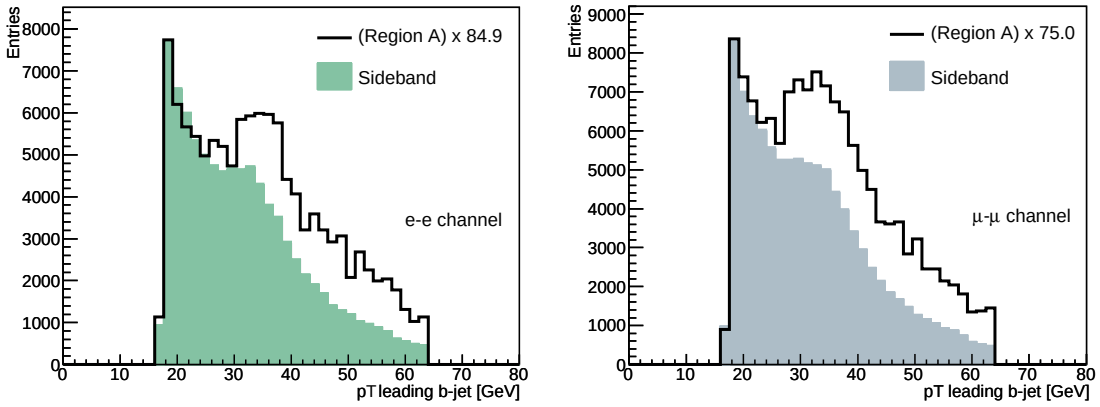

Figure 8.3: The p_T of the leading b-jet for the regions A and B. On the left side are the events for the $e - e$ channel, on the right side the events for the $\mu - \mu$ channel. The distributions are very similar. The $Z \to \tau\tau$ events (region A) are scaled for better visibility.

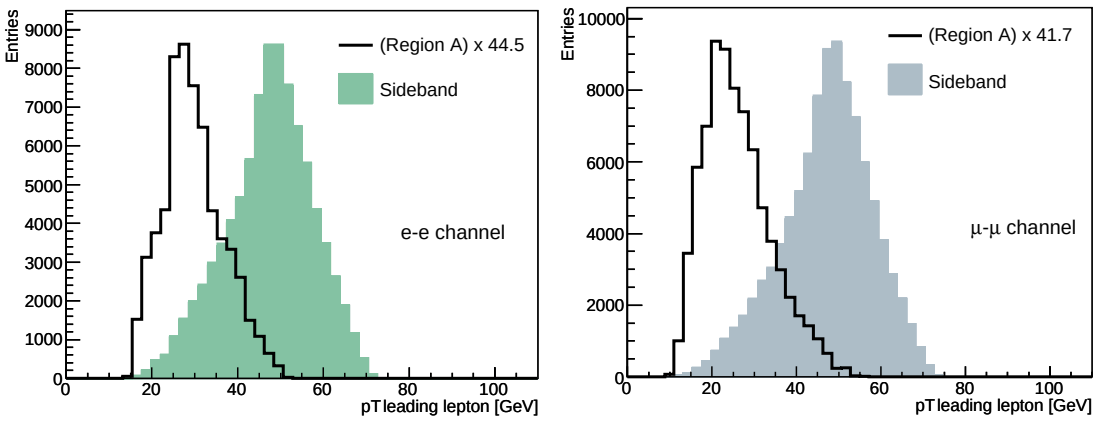

Figure 8.4: The p_T of the leading lepton for the regions A and B. On the left side are the events for the $e - e$ channel, on the right side the events for the $\mu - \mu$ channel. As expected, the p_T of leptons from $Z \to \ell\ell$ peak at higher values than leptons from $Z \to \tau\tau$. The $Z \to \tau\tau$ events (region A) are scaled for better visibility.

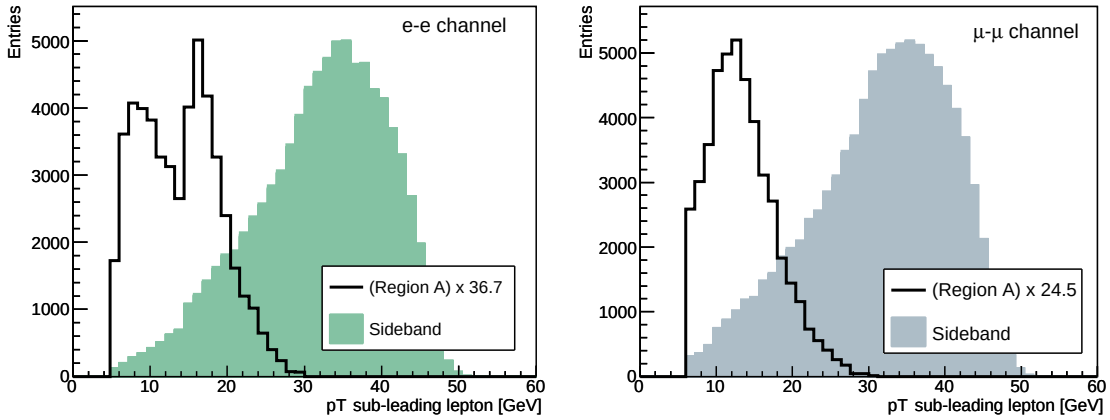

Figure 8.5: The p_T of the sub-leading lepton for the regions A and B. On the left side are the events for the $e-e$ channel, on the right side the events for the $\mu-\mu$ channel. The p_T difference between the leptons of the two samples is even higher than it is for the p_T of the leading lepton. The $Z \rightarrow \tau\tau$ events (region A) are scaled for better visibility.

8.4 Calculation of the $Z \to \tau\tau$ Event Number and Uncertainty in Data

The calculation of the events number of $Z \to \tau\tau$ events in the data sample is performed in bins of p_T of the leading lepton versus the p_T of the subleading lepton. This way the method is less dependent on the p_T differences between signal region and sideband region than performing the calculation in only one bin. In Figure 8.6 the 2D p_T distributions for the MC and data samples are shown for example in the $e - e$ channel.

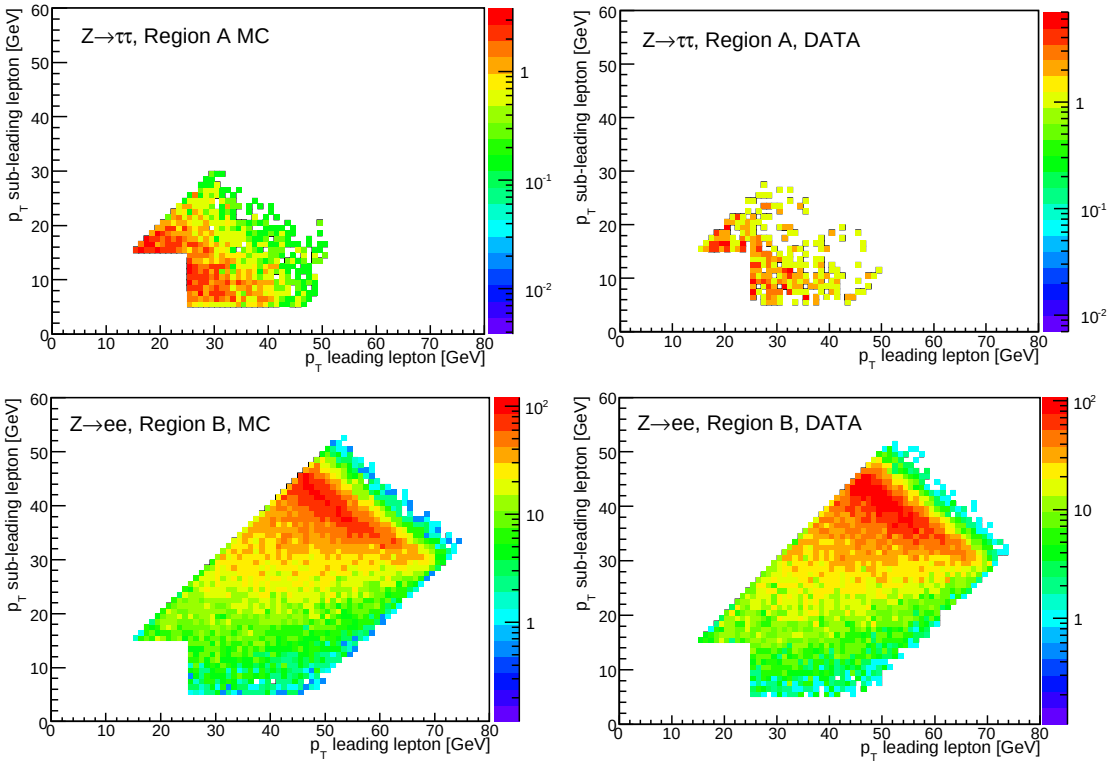

Figure 8.6: $p_{T,\ell 1}$ vs. $p_{T,\ell 2}$ of region A and region B for the MC and data samples. The white rectangles without events in the bottom left corner of each plot are due to trigger cuts (Section 5.2.1).

The number of $Z \to \tau\tau \to 2e + 4\nu$ events in region A in the data sample is given as follows:

$$(Z \to \tau\tau \to 2e + 4\nu)^A_{Data} = \sum_{i,j} \frac{\left((Z \to ee)^B_{Data}\right)_{i,j}}{\left((Z \to ee)^B_{MC}\right)_{i,j}} \cdot \left((Z \to \tau\tau \to 2e + 4\nu)^A_{MC}\right)_{i,j}, \quad (8.4)$$

where i and j give the number of the bin. Using Gaussian propagation of uncertainty, the variance on the number of events for the $e-e$ channel is given by the following formula:

$$
\begin{aligned}
(\Delta_{e-e})^2 \;\equiv\; & \left(\Delta\left(Z\to\tau\tau\to 2e+4\nu\right)^A_{Data}\right)^2 \\
= & \sum_{i,j} \frac{\left(\left(Z\to\tau\tau\to 2e+4\nu\right)^A_{MC}\right)^2_{i,j}\cdot\left(\Delta\left(Z\to ee\right)^B_{Data}\right)^2_{i,j}}{\left(\left(Z\to ee\right)^B_{Data}\right)^2_{i,j}} \\
+ & \sum_{i,j} \frac{\left(\left(Z\to ee\right)^B_{Data}\right)^2_{i,j}}{\left(\left(Z\to ee\right)^B_{MC}\right)^2_{i,j}}\cdot\left(\Delta\left(Z\to\tau\tau\to 2e+4\nu\right)^A_{MC}\right)^2_{i,j} \\
+ & \sum_{i,j} \frac{\left(\left(Z\to\tau\tau\to 2e+4\nu\right)^A_{MC}\right)^2_{i,j}\cdot\left(\left(Z\to ee\right)^B_{Data}\right)^2_{i,j}}{\left(\left(Z\to ee\right)^B_{MC}\right)^4_{i,j}}\cdot\left(\Delta\left(Z\to ee\right)^B_{MC}\right)^2_{i,j}.
\end{aligned}
\tag{8.5}
$$

The equations in the $\mu-\mu$ channels is equivalent.
The results are displayed in Figure 8.7. They show some dependance on the chosen binning but seem to be very promising.

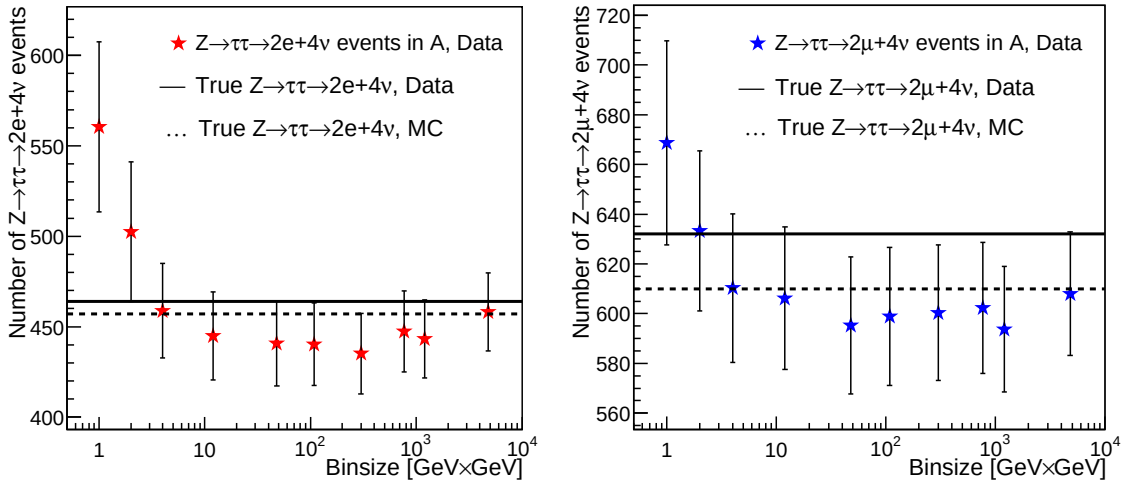

Figure 8.7: Number of $Z\to\tau\tau$ events as function of binsize. Left are the numbers of events for the $e-e$ channel, on the right the event numbers are displayed for the $\mu-\mu$ channel. The black line gives the true expectation on the number of $Z\to\tau\tau$ events in the data sample. The dashed line gives the expectation on the number of $Z\to\tau\tau$ events in the MC sample.

The calculated values are slightly lower than the MC expectation. The difference of the MC expectation to the number in the data sample is probably due to statistical fluctuation. Yet, the numbers agree well. For a binsize of 4 GeV^2 the calculated event number agree almost perfectly with the MC expectation for both channels. The values for this binsize are:

$$
\begin{aligned}
\left(Z\to\tau\tau\to 2e+4\nu\right)^A_{Data} &= 459 \quad , \quad \Delta\left(Z\to\tau\tau\to 2e+4\nu\right)^A_{Data} = 26.2 \\
\left(Z\to\tau\tau\to 2\mu+4\nu\right)^A_{Data} &= 610 \quad , \quad \Delta\left(Z\to\tau\tau\to 2\mu+4\nu\right)^A_{Data} = 29.9.
\end{aligned}
\tag{8.6}
$$

The relative errors for this 10 fb^{-1} predictions are:

$$\begin{aligned} \frac{\Delta\left(Z \to \tau\tau \to 2e + 4\nu\right)^{A}_{Data}}{\left(Z \to \tau\tau \to 2e + 4\nu\right)^{A}_{Data}} &= 5.7\,\% \\ \frac{\Delta\left(Z \to \tau\tau \to 2\mu + 4\nu\right)^{A}_{Data}}{\left(Z \to \tau\tau \to 2\mu + 4\nu\right)^{A}_{Data}} &= 4.9\,\%. \end{aligned} \tag{8.7}$$

Using those numbers, the geometric mean for the mixed channel is given as follows:

$$\begin{aligned} \left(Z \to \tau\tau \to e\mu + 4\nu\right)^{A}_{Data} &= 529 \\ \Delta\left(Z \to \tau\tau \to e\mu + 4\nu\right)^{A}_{Data} &= 28.0 \\ \frac{\Delta\left(Z \to \tau\tau \to e\mu + 4\nu\right)^{A}_{Data}}{\left(Z \to \tau\tau \to e\mu + 4\nu\right)^{A}_{Data}} &= 5.3\,\%. \end{aligned} \tag{8.8}$$

This calculation described in Section 8.4 must be repeated for a 30 fb^{-1} 'data' sample.

8.5 Influence of Uncertainties on the Significance

The modified significance with a relative systematic uncertainty ϵ is given as follows:

$$\frac{S}{\sqrt{B}} \to \frac{S}{\sqrt{B + \epsilon^2 \cdot B^2}}. \tag{8.9}$$

In Figure 8.8 the significance for different values of ϵ as function of m_A and $\tan\beta$ is shown. Assuming $\epsilon = 5\,\%$, a Higgs boson with a mass of 120 GeV can be discovery if $\tan\beta$>10. A Higgs particle with a mass of 160 GeV may be found if $\tan\beta$>11, a Higgs mass of 200 GeV may lead to a discovery if $\tan\beta$>14.5 is realized in nature.

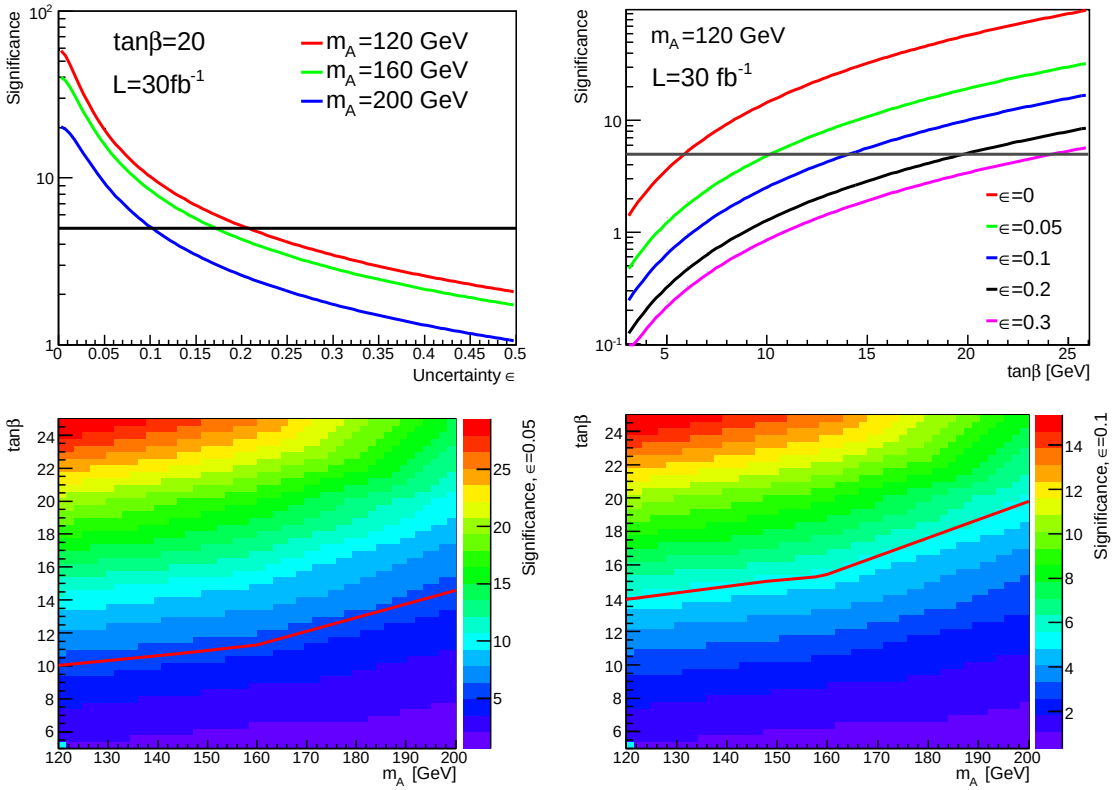

Figure 8.8: Significance for different values of the uncertainty ϵ. The upper left plot shows the significance as function of ϵ for three Higgs mass hypotheses. In the upper right plot the significance for several values of ϵ for $m_A = 120$ GeV as function of $\tan\beta$ is displayed. The two bottom figures show the significance as function of m_A versus $\tan\beta$ for two values of ϵ (bottom left: $\epsilon = 5\,\%$, bottom right: $\epsilon = 10\,\%$. The 5 σ contours are marked red.

Chapter 9

Conclusion

A study of the b-quark associated Higgs production in the decay mode $b\bar{b}\ h/A/H \rightarrow \tau\ \tau \rightarrow 2\ \ell + 4\ \nu$ with the ATLAS detector at LHC has been performed. The discovery potential of a mass degenerated neutral MSSM Higgs boson has been determined for different points in the $m_A - \tan\beta$ plane in the $\mathrm{m_h^{max}}$-scenario.
The signal process has been generated using the Monte Carlo generator Sherpa. The ATLAS detector response has been obtained by using the fast simulation ATLFast. The mass degeneration, branching ratios and cross sections depending on m_A and $\tan\beta$ have been studied. The Higgs boson mass has been reconstructed using the collinear approximation. The validity of this approximation and its dependence on cuts have been studied. The resulting invariant $\tau\tau$ mass shows a large width due to a relatively small mean value of the p_T of the Higgs particle. Cut optimizations for three low and medium Higgs masses have been performed separately in the three sub-decay channels to increase the significance for a discovery. The discovery potential as function of $\tan\beta$ in the mass range $120\,GeV < m_A < 200\,GeV$ has been obtained. A fit of the $m_{\tau\tau}$ shape has been attempted by using a different set of cuts. Although the fit seems to be promising the parametrization has to be improved further.
As a result of this study the channel $b\bar{b}\ h/A/H \rightarrow \tau\ \tau \rightarrow 2\ \ell + 4\ \nu$ has been proven to be among the most promising channels in ATLAS, if Supersymmetry is realized in nature. Assuming no systematic uncertainty, a Higgs boson with a mass of $m_A = 120$ GeV can be discovered if $\tan\beta$>6. If the Higgs particle has a mass of 160 GeV it will be discovered if $\tan\beta$>7. If its mass is about 200 GeV it can be discovered if a value of $\tan\beta$>10 is realized in nature.
Further studies are necessary before the data acquisition starts. Improvements of the significance of a discovery could be achieved by performing trigger studies, upgrading lepton identification algorithms and increasing b-tagging efficiencies. Therefor this analysis has to be repeated using full detector simulation.
Another challenging plan is to develop a reliable method to estimate the background from data. A new method how to obtain the number of $Z \rightarrow \tau\tau$ events from data has been attempted successfully and will be pursued further. Another promising method is described in [66]. There the p_T values of muons from $Z \rightarrow \mu\mu$ decays get reweighted to simulate $Z \rightarrow \tau\tau \rightarrow \mu\mu + 4\nu$ decays. This works well for Vector-Boson-Fusion analysis and the $\mu - \mu$ channel. It will be tested whether this method can be applied onto the studied channel of the b-quark associated Higgs production.

In addition, uncertainties on cross sections of signal and backgrounds must be considered. The reliability of the used Monte Carlo description must be cross checked with the experimental gained data once these are available.
A combination of the lepton-lepton decay mode with the hadron-lepton and hadron-hadron mode could improve the significance further. A scan of the significance in the other MSSM scenarios could be interesting, too.

Appendix A

Introduction to Supersymmetry Algebra

In Supersymmetry (SUSY) the matter particles and the force carriers are united in one concept. A SUSY transformation Q is an operation linking fermionic and bosonic states [67]:

$$\begin{aligned} Q|Boson\rangle &\propto |Fermion\rangle \\ Q|Fermion\rangle &\propto |Boson\rangle. \end{aligned} \tag{A.1}$$

In the following a very simple model is being constructed showing some ideas of this concept. The model assumes non-interacting bosons and fermions in a field free space, using second quantization. The many-body wavefunction Ψ can be given as a state in the Fock space:

$$|\Psi\rangle = |n_1, n_2, ..., n_i, ...\rangle. \tag{A.2}$$

n_i gives the number of particles in the state i, for fermions n can only be 0 or 1 due to the Pauli principle. In the model the many body states are products of fermionic states $|n_F\rangle$ and bosonic states $|n_B\rangle$:

$$|n_B n_F\rangle = |n_B\rangle \cdot |n_F\rangle. \tag{A.3}$$

Bosons (fermions) are created by the creation operator b^+ (f^+) and annihilated by b (f). The usual commutator relations apply in this model:

$$\begin{aligned} [{b_i}^+, b_j]_- &= \delta_{ij} \\ [{f_i}^+, f_j]_+ &= \delta_{ij}. \end{aligned} \tag{A.4}$$

The SUSY operators Q are now defined as:

$$\begin{aligned} Q^+ &= b\, f^+ \\ Q &= b^+ f. \end{aligned} \tag{A.5}$$

Q^+ annihilates a boson and creates a fermion, Q creates a boson and annihilates a fermion.

$$\begin{aligned} Q^+|n_B n_F\rangle &\propto |n_B - 1, n_F + 1\rangle \\ Q|n_B n_F\rangle &\propto |n_B + 1, n_F - 1\rangle. \end{aligned} \tag{A.6}$$

Because Q^+ and Q are not hermitic operators, new linear combinations can be defined:

$$\begin{aligned} Q_1 &= Q^+ + Q \\ Q_2 &= -i(Q^+ - Q). \end{aligned} \tag{A.7}$$

Using energy conservation under a SUSY transformation, it can be shown that the SUSY Hamiltonoperator H_S takes a simple form:

$$H_S = Q_1^2 = Q_2^2. \tag{A.8}$$

In a harmonic potential (SUSY oscillator) the SUSY operators get multiplied with a factor $\sqrt{\hbar\omega}$ and H_S takes the form:

$$H_S = \hbar\omega(b^+b + f^+f) = H_B + H_F. \tag{A.9}$$

H_B (H_F) is the Hamiltonoperator for a bosonic (fermionic) harmonic oscillator:

$$\begin{aligned} H_B &= \hbar\omega(b^+b + \frac{1}{2}) \\ H_F &= \hbar\omega(f^+f - \frac{1}{2}). \end{aligned} \tag{A.10}$$

If N_B (N_F) is the number of bosons (fermions) in the system, then the energy levels of the bosonic (fermionic) oscillator are:

$$\begin{aligned} E_B &= \hbar\omega(N_B + \frac{1}{2}) \\ E_F &= \hbar\omega(N_F - \frac{1}{2}). \end{aligned} \tag{A.11}$$

So finally the energy levels (eigenvalues) of the SUSY oscillator are:

$$E_S = \hbar\omega(N_B + N_F). \tag{A.12}$$

In the last equation there is no zero state energy. From this one can conclude one general remark on SUSY models: Zero state energies in quantum field theories often lead to divergences and infinities, but in SUSY models such divergences are handled better or even disappear.

Appendix B

Feynman Graphs for the Signal Process included in Sherpa

2→2 Process

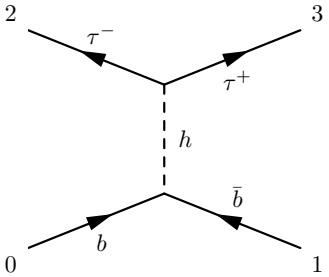

Graph 1

2→3 Processes

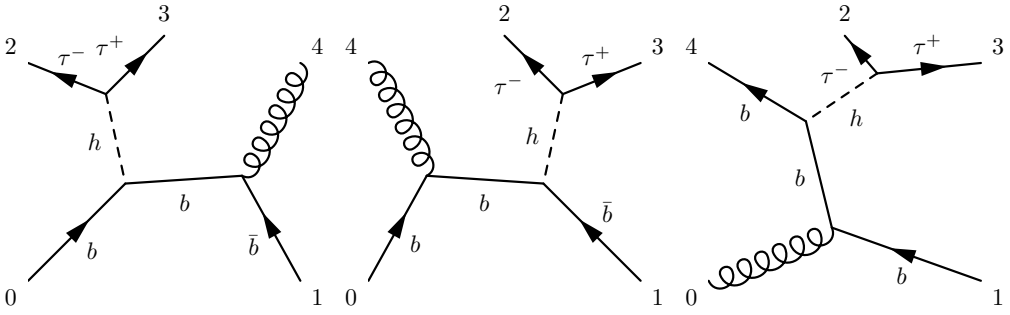

Graph 2

Graph 3

Graph 4

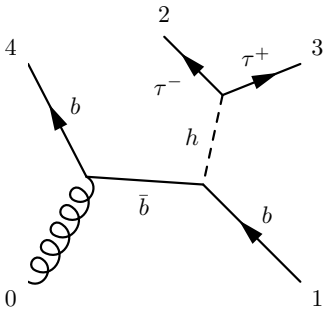

Graph 5

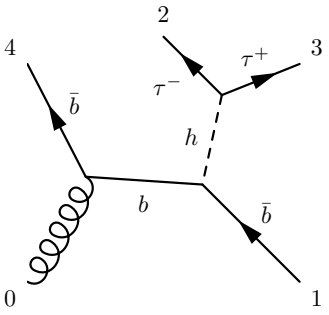

Graph 6

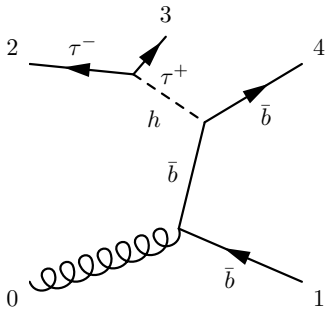

Graph 7

2→4 Processes (selection)

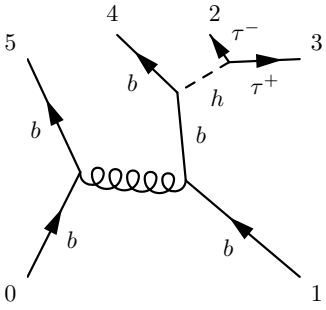

Graph 8

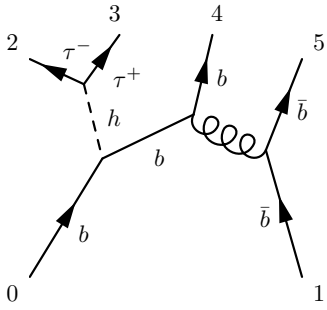

Graph 9

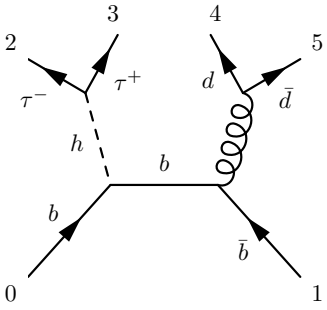

Graph 10

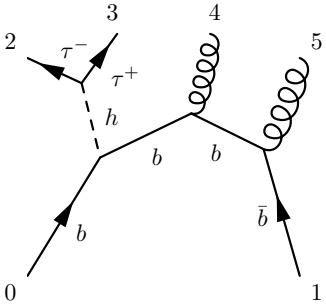

Graph 11

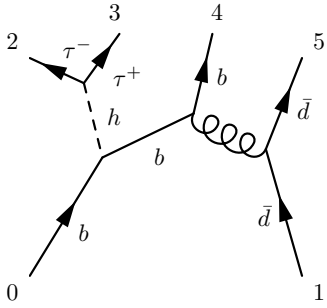

Graph 12

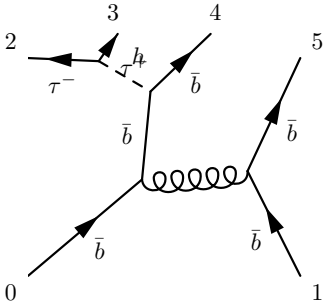

Graph 13

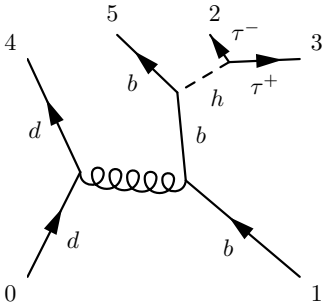

Graph 14

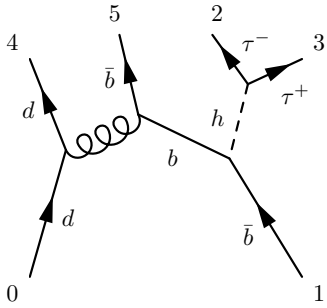

Graph 15

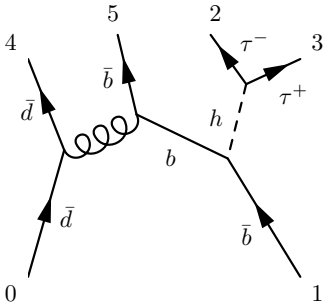

Graph 16

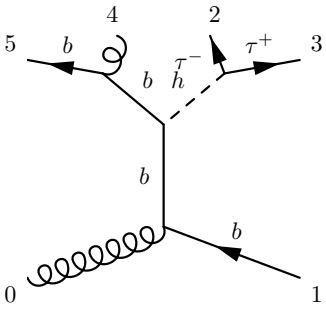

Graph 17

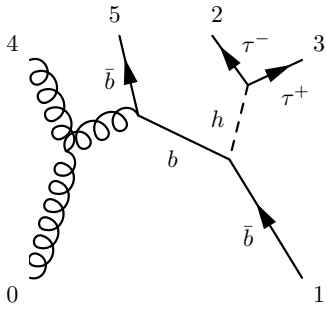

Graph 18

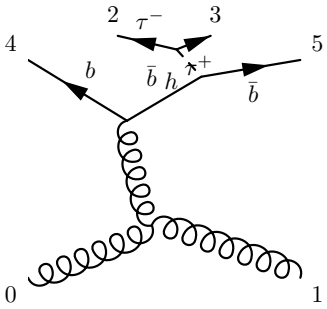

Graph 19

Appendix C

Mass Distributions

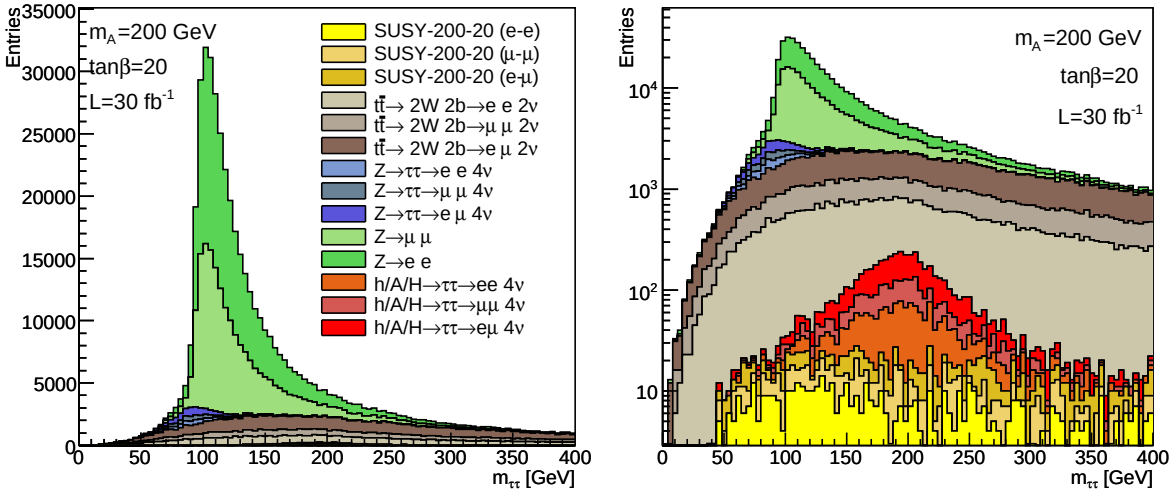

Figure C.1: Stacked background events and 200 GeV Higgs signal events after precuts, normalized to an integrated luminosity of 30 fb^{-1}, broken down to sub-channels.

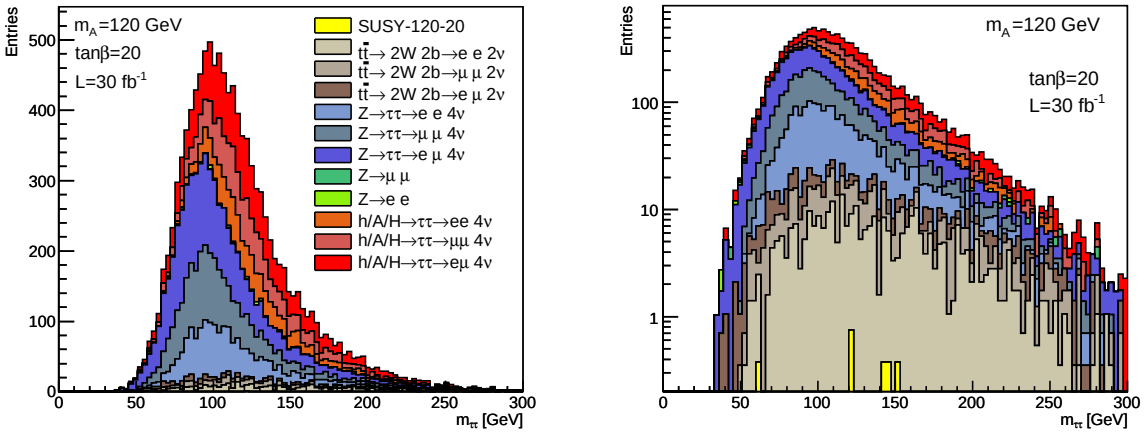

Figure C.2: Final $m_{\tau\tau}$ spectrum after all cuts (m_A=120 GeV, $\tan\beta$=20, L=30 fb^{-1}), broken down to sub-channels.

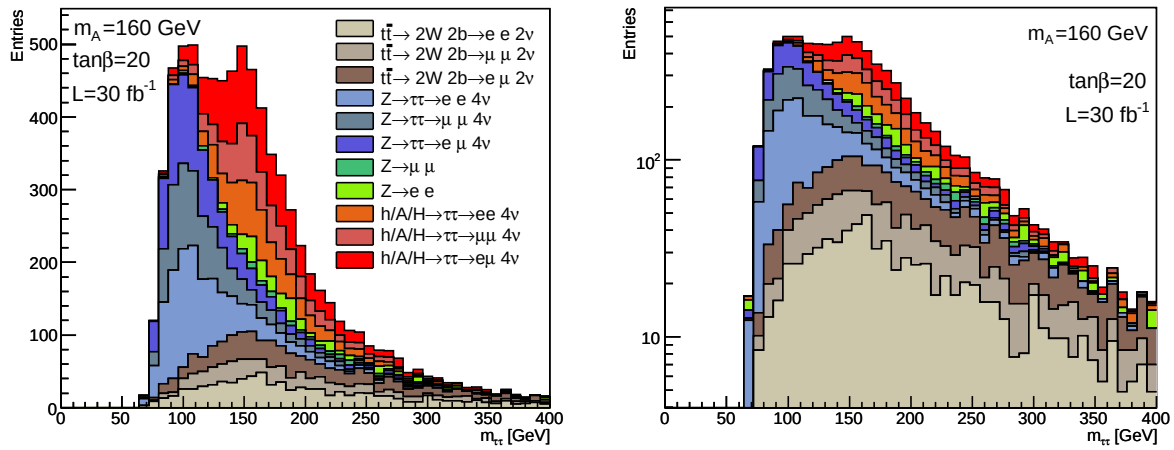

Figure C.3: Final $m_{\tau\tau}$ spectrum after all cuts (m_A=160 GeV, $\tan\beta$=20, L=30 fb^{-1}), broken down to sub-channels.

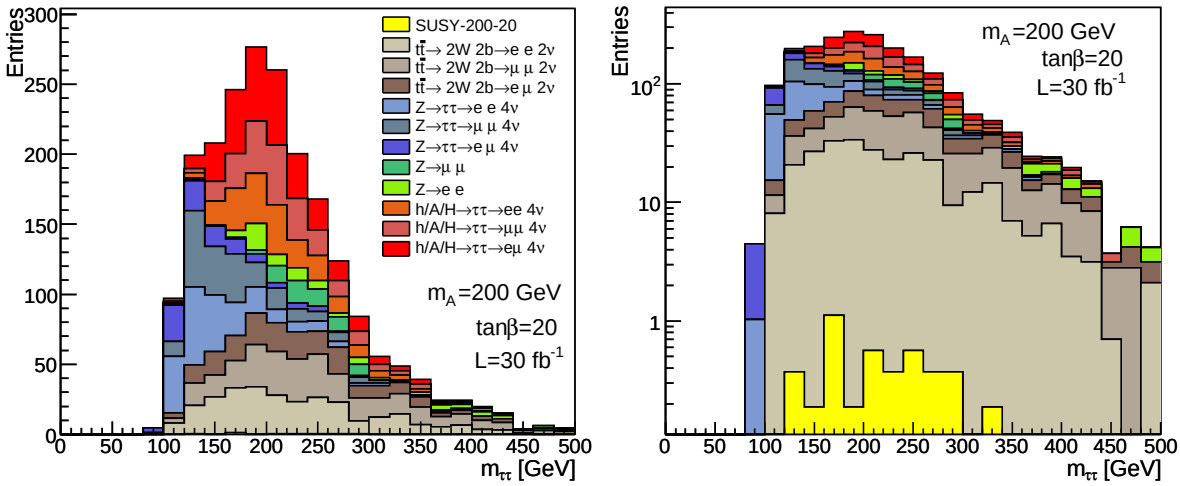

Figure C.4: Final $m_{\tau\tau}$ spectrum after all cuts (m_A=200 GeV, $\tan\beta$=20, L=30 fb^{-1}), broken down to sub-channels.

Bibliography

[1] *S.L. Glashow, Nucl. Phys.* **22** *(1961), S. Weinberg, Phys. Rev. Lett.* **19** *(1967), A. Salam, in Elementary Particle Theory, Stockholm, "Almquist and Wiksell" (1968).*

[2] W.-M. Yao *et al.*, J. Phys. **G 33** (2006).

[3] Peter W. Higgs, *Broken Symmetries and the Masses of Gauge Bosons*, Phys. Rev. Lett. **13** (1964).

[4] Peter W. Higgs, *Spontaneous symmetry breakdown without massless bosons*, Phys. Rev. **145** (1966).

[5] J. Goldstone, A. Salam and S. Weinberg, *Broken Symmetries*, Phys. Rev. **127** (1962).

[6] M. Veltman, G. 't Hooft, *Regularization and renormalization of gauge fields*, Nucl. Phys. **B 44** (1972).

[7] ALEPH, DELPHI, L3 & OPAL Collaboration, R. Barate et al., *Search for the Standard Model Higgs boson at LEP*, Phys. Lett. **B 565** (2003).

[8] M. Spira, P.M. Zerwas, *Electroweak Symmetry Breaking and Higgs Physics*, arXiv:hep-ph **9803257** (1997).

[9] Jochen Cammin, *Study of a Light Standard Model Higgs Boson in the ttH^0 Channel with ATLAS at LHC and Decay-Mode Independent Searches for Neutral Higgs Bosons wih OPAL at LEP*, Ph.D. thesis, Bonn University (2004), BONN-IR-2004-06.

[10] ATLAS Collaboration, *Detector and Physics Performance. Technical Design Report. Volume II.*, CERN-LHCC-99-15, 1999.

[11] ATLAS Collaboration, S. Asai et al., *Prospects for the Search of a Standard Model Higgs Boson in ATLAS using Vector Boson Fusion*, SN-ATLAS-2003-024, 2003.

[12] J.A. Casas, J.R. Espinosa, I. Hidalgo, *Implication for New Physics from Fine-Tuning Arguments*, JHEP **0411 057** (2004).

[13] Vera Rubin, *Rotation of the Andromeda Nebula from a Spectroscopic Survey of Emission Regions*, Astrophys. **159** (1970).

[14] WMAP collaboration, *First Year Wilkinson Microwave Anisotropy Prope (WMAP) Observations*, Astrophys. J. **148 175** (2003).

[15] Superkamiokande Collaboration, *Evidence for an oscillatory signature in atmospheric neutrino oscillation*, Phys. Rev. Lett. **93, 101801** (2004).

[16] John F. Gunion, Howard E. Haber, Gordon Kane, Sally Dawson, *The Higgs Hunters Guide*, Addison-Wesley, 1990.

[17] Robert V. Harlander, William B. Kilgore, *Higgs boson production in bottom quark fusion at next-to-next-to-leading order*, Phys. Rev. Lett. **D 68, 013001** (2003).

[18] M. Carena, S. Heinemeyer, C.E.M. Wagner, G. Weiglein, *Suggestions for Benchmark Scenarios for MSSM Higgs Boson Searches at Hadron Collider* (2002).

[19] ALEPH, DELPHI, L3 and OPAL Collaborations, The LEP Working Group for Higgs Boson Searches, *Search for Neutral MSSM Higgs Bosons at LEP* (2006).

[20] K. Müller, *Online lecture script*, http://www.physic.unizh.ch/∼kmueller/text/vorlesung/susy/node34.html.

[21] H.N. Brown et. al, *Precise measurements of the positive muon anomalous magnetic moment*, Phys. Rev. Lett. **D 86, 2227** (2001).

[22] The Tevatron Electroweak Working Group for the CDF and DØ Collaboration, *Combination of CDF and DØ Results on the Mass of the Top Quark* (2007).

[23] CMS, *CMS Physics Technical Design Report: Volume I, Detector Performance and Software*, CERN-LHCC-2006-001, 2006.

[24] *The Large Hadron Colloider beauty experiment website*, http://lhcb.web.cern.ch/lhcb.

[25] CERN, *ALICE Technical Proposal*, CDS cer-000214817, 1995.

[26] *Höchstenergetische Teilchenbeschleuniger*, http://www.physik.uni-muenchen.de/∼Ottmar.Biebel/TeVLHC-seminar/SLoew-Beschleuiniger.pdf.

[27] ATLAS Collaboration, *Technical Proposal for a General Purpose pp Experiment at the Large Hadron Collider at CERN*, CERN/LHC (1994).

[28] ATLAS Collaboration, *Detector and Physics Performance. Technical Design Report. Volume I.*, CERN/LHC, 1999.

[29] Christoph Ruwiedel, *Studie zur Messbarkeit der Struktur der Kopplung eines Higgs-Bosons an schwache Eichbosonen in der Vektorbosonfusion mit dem ATLAS-Detector am LHC*, Diploma thesis, Bonn University (2006).

[30] *ATLAS Transition Radiation Tracker website*, http://pcwetans.web.cern.ch/pcwetans/atlas-trt/.

[31] J. Butterworth, *Modelling Underlying Events and Minimum Bias Physics*, http://www.wlap.org/file-archive//atlas/20040622-umwlap002-06-butterworth.pdf.

[32] *Article in Wikipedia The Free Encyclopedia*, http://en.wikipedia.org/wiki/Grid_computing.

[33] *Worldwide LHC Computing Grid website*, http://lcg.web.cern.ch/LCG/index.html.

[34] T. Sjöstrand, *Monte Carlos for LHC*, http://thep.lu.se/ torbjorn/talks/cern04cms.pdf.

[35] *GEANT4 website*, http://geant4.web.cern.ch/geant4/.

[36] *ATLFast website*, http://www.hep.ucl.ac.uk/atlas/atlfast/.

[37] E. Richter-Was, D. Froidevaux, L. Poggioli, *ATLFast 2.0 a fast simulation package for ATLAS* **ATL-PHYS-98-131** (1998).

[38] S. Heinemeyer, *Feynhiggs website*, http://www.feynhiggs.de.

[39] T. Gleisberg, S. Höche, F. Krauss, A. Schaelicke, S. Schumann, J.-C. Winter, *SHERPA 1.α, a proof of concept version*, JHEP **0402 056** (2004).

[40] S. Catani, F. Krauss, R. Kuhn, B.R. Webber, *QCD matrix elements + Parton Showers*, JHEP **0111 063** (2001).

[41] F. Krauss, *Matrix elements and Parton Showers in Hadronic Interactions*, JHEP **0208 015** (2002).

[42] *Sherpa mini documentation (version 1.0.9)*, http://hepforge.cedar.ac.uk/hf/archive/sherpa/howto-1.0.9.pdf.

[43] J.M. Campell, R.K. Ellis, *Radiative corrections to $Zb\bar{b}$ production*, Phys. Rev. **D 62, 114012** (2000).

[44] D. Pallin, *Top Physics at the LHC*, http://atlas.web.cern.ch/Atlas/GROUPS/PHYSICS/Conferences/2006/Top-06_Pallin.ppt.

[45] S. Frixione, B.R. Webber, *Matching NLO QCD computations and parton shower simulations*, JHEP **0206** (2002).

[46] S. Frixione, P. Nason, B.R. Webber, *Matching NLO QCD computations and parton showers in heavy flavour production*, JHEP **0308** (2003).

[47] *Jimmy website*, http://projects.hepforge.org/jimmy/.

[48] N. Kidonakis, R. Voigt, *Next-to-next-to-leading order soft gluon corrections in top quark hadroproduction*, Phys. Rev. **D 68, 114014** (2003).

[49] Nicolas Möser, *Untersuchung des Entdeckungspotentials schwerer neutraler Higgsbosonen im Zerfallskanal $A^0/H^0 \to \tilde{\chi}_2^0\tilde{\chi}_2^0 \to \tilde{\chi}_2^0\tilde{\chi}_2^0 + 4\,l$ mit dem ATLAS-Detektor*, diploma Thesis, Bonn University (2006).

[50] *Nicolas Möser (Bonn university), private communication.*

[51] G. Corcella, I.G. Knowles, G. Marchesini, S. Moretti, K. Odagiri, P. Richardson, M.H. Seymour, B.R. Webber, *Herwig 6.5*, JHEP **0101** (2001).

[52] S. Moretti, K. Odagiri, P. Richardson, M.H. Seymour, B.R. Webber, *Implementation of supersymmetric processes in the Herwig event generator*, JHEP **0204** (2002).

[53] W. Beenakker, R. Höpker, M. Spira, *Prospino. A program for the production of supersymmetric particles in next-to-leading order QCD*, arXiv:hep-ph **9611232** (1996).

[54] *Madgraph website*, http://madgraph.hep.uiuc.edu/.

[55] *Pythia website*, http://projects.hepforge.org/pythia6/.

[56] *ATLAS Trigger and Acquisition wiki*, http://twiki.cern.ch/twiki/bin/view/Atlas/TriggerDAQ/.

[57] *Markus Warsinsky (Dresden University), private communication. M. Warsinskys Ph.D. thesis in preparation.*

[58] Iris Rottländer, *Studie zum Entdeckungspotenzial fuer ein Higgs-Boson aus Vektorbosonfusion mit leptonischem Zerfall fuer das ATLAS-Experiment am LHC*, Diploma thesis, Bonn University (2005).

[59] *Georgios Dedes (MPI Munich), private communication. G. Dedes' Ph.D. thesis in preparation.*

[60] *The ROOT website*, http://root.cern.ch.

[61] M. J. Oreglia, *A Study of the Reactions* $\Psi' \to \gamma\gamma\Psi$, Ph.D. thesis (1980), SLAC-236.

[62] J. E. Gaiser, *Radiative Decays of the* Ψ' *to All-Photon Final States*, Ph.D. thesis (1982), SLAC-255.

[63] T. Skwarnicki, *A Study of the Radiative Cascade Transitions between* Υ' *and* Υ *Resonances*, Ph.D. thesis (1986), DESY F31-86-02.

[64] *Michael Kobel (Dresden University), private communication.*

[65] F. James, *MINUIT Minimization package, CERN Program Library Long Writeup D506*, http://seal.web.cern.ch/seal/work-packages/mathlibs/minuit.

[66] Martin Schmitz, *Studie zur Bestimmung des Untergrundes aus Daten und der Higgs-Boson-Masse in Vektorbosonfusion mit* $H \to \tau\tau \to \mu\mu{+}4\nu$ *mit dem ATLAS-Detektor am LHC*, Diploma thesis, Bonn University (2006).

[67] H. Kalka, G.Soff, *Supersymmetrie*, Teubner Studienbuecher, 1997.

Danksagung

An dieser Stelle möchte ich mich bei den Menschen bedanken, die zum Gelingen meiner Diplomarbeit beigetragen haben. Ich möchte dabei als erstes die gesamte ATLAS Gruppe der TU Dresden erwähnen. Ganz besonders hilfreich war mein Zimmergenosse Markus Warsinsky, der mir stets mit vielen Ratschlägen weiterhelfen konnte. Meinen Betreueren Dr. Wolfgang Mader sowie Prof. Michael Kobel danke ich, dass sie mir nicht nur die Möglichkeit gaben, an einem aktuellen und interessanten Thema zu forschen, sondern auch meine Resultate beim internationalen Higgs Meeting am CERN vorzutragen, was mich sehr motiviert hat. Markus und Thomas Göpfert danke ich für das aufmerksame Korrekturlesen meiner Arbeit. Ich möchte weiterhin Dr. Rainer Schwierz danken, da er jederzeit bei computertechnischen Problemen zur Stelle war und außerdem die Hardware für den Institutskaffee bereitgestellt hat. Auch mein Papa hat mit seiner unermesslichen Unterstützung sehr zum Gelingen dieser Arbeit beigetragen.
Aufgrund der angenehmen und heiteren Atmosphäre in der Gruppe ist mir das letzte Jahr trotz aller Anstrengungen eine Freude gewesen und ich bin gespannt auf die weitere Zeit.

Erklärung

Hiermit versichere ich, dass ich die vorliegende Arbeit selbständig und ohne Benutzung anderer als der angegebenen Hilfsmittel angefertigt habe. Die aus fremden Quellen direkt oder indirekt übernommenen Resultate sind als solche kenntlich gemacht.

Dresden, den 25.06.2007

Jana Schaarschmidt